QUANTUM DESCRIPTION OF THE IMPULSIVE PHOTODISSOCIATION DYNAMICS OF I_3^- IN SOLUTION

GUY ASHKENAZI, URI BANIN, ALLON BARTANA, RONNIE KOSLOFF, AND SANFORD RUHMAN

Department of Physical Chemistry and the Fritz Haber Center for Molecular Dynamics, The Hebrew University, Jerusalem, 91904 Israel

CONTENTS

I. Introduction
  A. Experimental Background
  B. Theoretical Background
  C. Objective
  D. Outline for the Paper
II. Methods
  A. Statics
    1. Describing the State of the System
    2. Visualizing the State of the System
    3. Initial States
  B. Dynamics
    1. The Hamiltonian Operator
    2. The Dissipative Super-Operators
    3. The Evolution Operator
  C. Interpretation
    1. The Impulsive Excitation Picture
    2. Power Absorption of a Laser Pulse
    3. Absorption Spectrum
    4. Raman Spectrum
  D. Method Summery
III. Application
  A. Electronic Potential Energy Surfaces
  B. Photodissociation of I_3^-: The "Pump" Pulse
    1. Statics

Advances in Chemical Physics, Volume 100, Edited by I. Prigogine and Stuart A. Rice.
ISBN 0-471-17458-0

2. Dynamics
3. Interpretation
C. Dynamics of the photo-induced "hole" in I_3^-
1. Statics
2. Dynamics
3. Interpretation
D. Dynamics of Nascent I_2^-: The "Probe" Pulse
1. Statics
2. Dynamics
3. Interpretation
E. Vibrational Excitation of Relaxed I_2^-: The "Push" Pulse
1. Statics
2. Dynamics
3. Interpretation
F. Application Summary
IV. Summary
A. Critical Evaluation
B. Conclusions
APPENDIX A. Numerical Methods
1. Approximating Functions of Operators
2. Newton's Interpolation Method
3. Leja's Interpolation Points
4. Application to Operators
APPENDIX B. System Parameters
References

I. INTRODUCTION

The study of the dynamics and relaxation of simple chemical and photochemical reactions in solution is essential for the understanding of solution phase chemistry in its entirety. This study is part of an extensive experimental and theoretical effort aimed at gaining insight into the mechanism of photochemical reactions in solution. The strategy followed is to reduce the complexity of the mechanism by following the photodissociation dynamics in real time, so that the elementary steps can be studied sequentially. The photodissociation dynamics of I_3^- in different solvents has been chosen as a test case for this study. The significance of this system rises from the ability to observe coherent motion in the condensed phase on a sub-picosecond time scale, utilizing ultrafast pump-probe spectroscopy. This temporal resolution enables the separation in time of major events, which are basic to the understanding of condensed phase chemical dynamics, such as the intramolecular motion leading to bond cleavage, and energy flow between solute and solvent. In particular, direct access to the temporal evolution of photoproducts is made possible by these techniques allowing reconstruction of the time-dependent electronic and nuclear density operator. In turn,

this extremely detailed description of dynamics provides a stringent testing ground of various theoretical descriptions of dissipative phenomena of highly excited molecules in solution.

A. Experimental Background

The photoinduced dynamics of I_3^- are inferred from a combination of CW and pump pulse spectroscopic measurements. The parent triiodide ion is linear and symmetric in solution, and stable in many polar solvents. The absorption spectra of I_3^- in solution consists of two bands, peaked at ~290 and ~350 nm, whose spectral assignment has been the subject of debate. The most common explanation is that excitation leads to dissociative states correlating with $I_2^-(^2\Sigma_u^+)$ in the ground state, and I ($^2P_{1/2,3/2}$) in either of its lowest spin-orbit states. The photoproduct's diiodide electronic absorption spectrum is composed of two bands—one in the near UV, partly overlapping the I_3^- absorption spectra, and the other in the near IR, centered at ~740 nm. The separate spectral bands for reactant and product enable a direct interpretation of the pump-probe spectroscopy. The absorption spectrum of I_3^- and I_2^- are shown in Fig. 1.

In the experimental system, solvated I_3^- is subjected to an intense, short UV pump pulse, which dissociates it into I_2^- + I^*. A weak probe pulse in the visible region, in resonance with the nascent I_2^- product absorption, interrogates the photoproduct. A probe pulse in the UV region in resonance with the I_3^- absorption interrogates the photoinduced dynamics on the ground electronic surface of I_3^- (Fig. 2). At the application of the pump pulse, a sud-

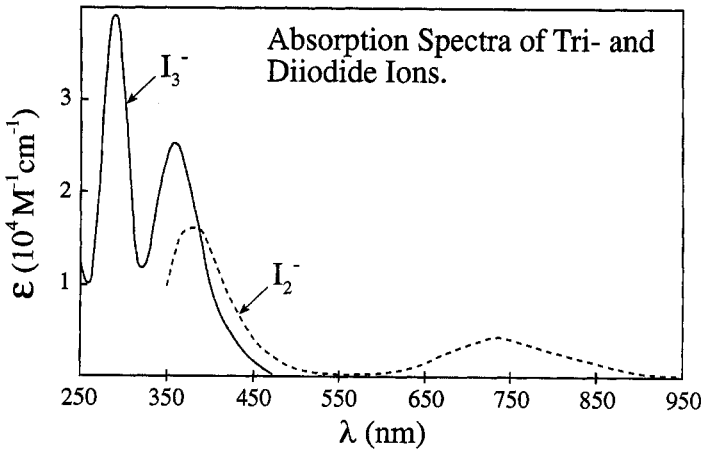

Figure 1. Absorption spectrum of I_3^- and I_2^-, showing the two absorption bands of I_3^- and of I_2^-.

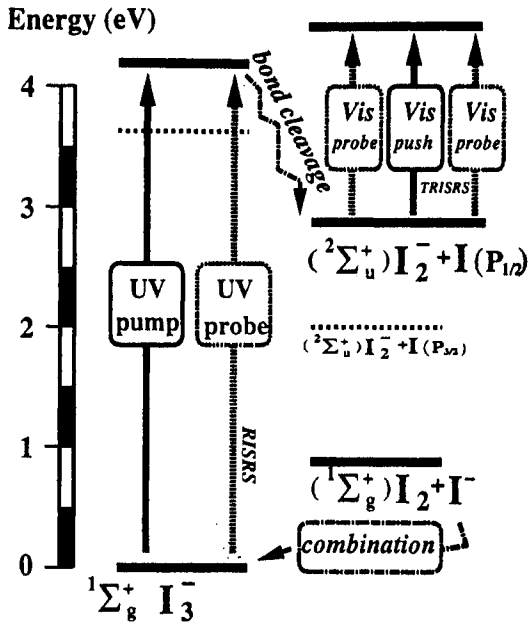

Figure 2. The energy bands associated with the I_3^- system. The UV pump initializes two separate processes. The first is photodissociation to I_2^-, which is probed in the visible region. The second is the RISRS process, which is probed in the UV region. In the TRISRS experiment, the I_2^- photoproduct can be invigorated by a push pulse and probed again in the visible region. The dashed levels show other possible routes to pump probe experiments.

den rise in absorption of the visible probe is observed, followed by a rapid reduction in absorption that lasts for nearly 300 fsec. During the following stages a slight increase of absorption is observed, which is accompanied by weak damped oscillations in the optical density [1]. The parameters of these oscillations strongly depend on the solvent (Fig. 3). The first instantaneous appearance of absorption is associated with the excited state of I_3^-. The stage of rapid reduction in the optical density is assigned to the process of bond fission, and emergence of the nascent fragments. The spectral modulations are attributed to the product state, in which a coherent population oscillates in and out of resonance with the probe, meaning that the I_2^- vibration is synchronized with the bond cleavage. Different probe wavelengths will correspond to different phases in the vibration [Fig. 12(*c*)]. Experimentally this is evident through a π phase shift of the spectral modulations, when probing with a blue and red shifted pulses (Fig. 4) [1].

Probing in the UV range reveals a similar phenomena, assigned to resonant impulsive stimulated raman scattering (RISRS) of the ground state population. This process can be visualized as a coherent "hole" created in

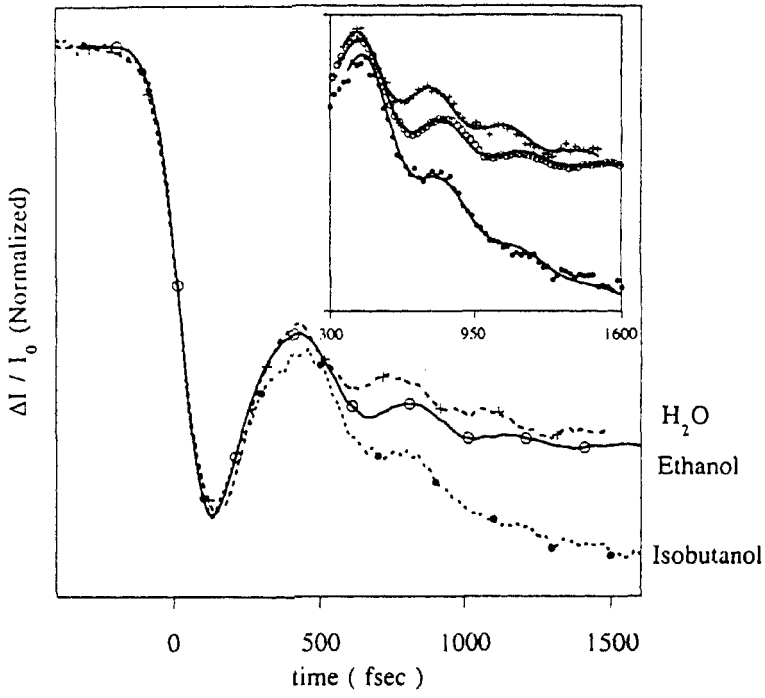

Figure 3. Transient transmission at short delays for three molecular solvents.

the reactant by lost product. Since the "hole" is not stationary it oscillates with the ground surface frequencies (Fig. 5). The spectral modulations of the "hole" shed light on the excitation stage [2]. This vibration can be correlated to the Raman spectrum of I_3^- (Fig. 6) [3].

The energetics of the photodissociation of I_3^- are such that 1.4 eV of excess energy has to be dissipated by the solvent. In an isolated system, kinematic considerations for a linear homonuclear triatomic molecule suggest that $\frac{1}{3}$ of the excess energy appears as vibration. The observed frequency of the modulations suggests a much lower vibrational excitation in the product, so part of this energy must be dissipated into the solvent during the dissociation stage. The rest of the excess energy will be dissipated by the product until thermal equilibrium is reached.

In order to study the evolving vibrational product distribution, at different delay times after the pump pulse, a second intense "push" pulse is applied to the system. The push pulse is in resonance with the nascent I_2^- product absorption, and so initiates a transient RISRS (or TRISRS) process, which sets a coherent motion in the I_2^- ground state population [4]. This motion is observed by modulations in the absorption of a third, weak probe pulse. The

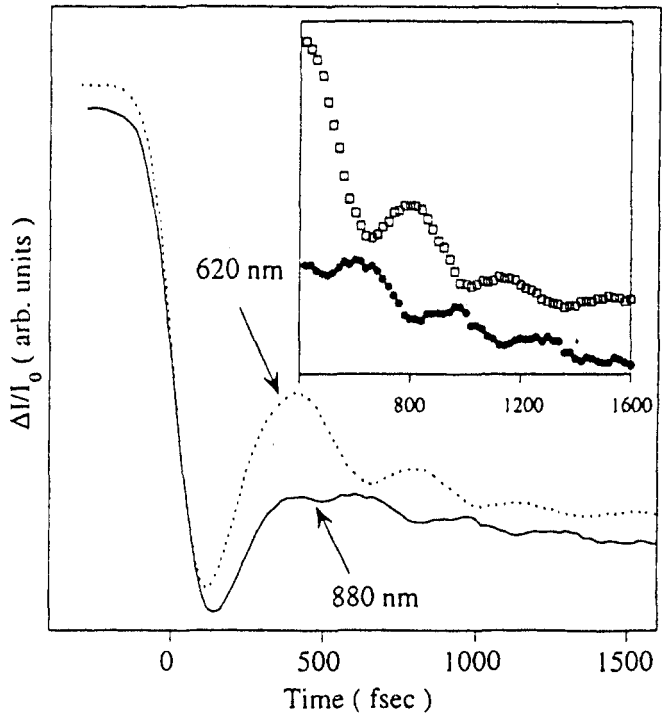

Figure 4. Transient transmission measurements at two probe wavelengths shifted to the blue (620 nm) and to the red (880 nm) of the maximum absorption wavelength for the near IR band of I_2^-. The solvent is water. There is a π radians phase shift of the oscillations between the two probe wavelengths.

parameters of the modulations (frequency, decay time) depend on the delay period between the pump and push pulses (Fig. 7), and so contain information about the vibrational dynamics of the transient species at the push instant. A schematic illustration of the possible pump-probe experiments is depicted in Fig. 2.

The experimental investigation of the I_3^- system is an ongoing story. Dissociation of I_3^- to I_2^- has recently been induced on the lower absorption band of 350 nm showing similar qualitative behavior [5]. To study the influence of initial symmetry, the photodissociation of I_2Br^- to I_2^- + Br [6] has been investigated and shows strong spectral modulations. The analysis presented here can also be applied to other photodissociation processes in solution, such as the dynamics of HgI_2, which has been studied both in the gas phase [7, 8] and in solution [9, 10]. Even at this stage, the degree of detail in the experiments requires an expansion of our theoretical descriptions and visual-

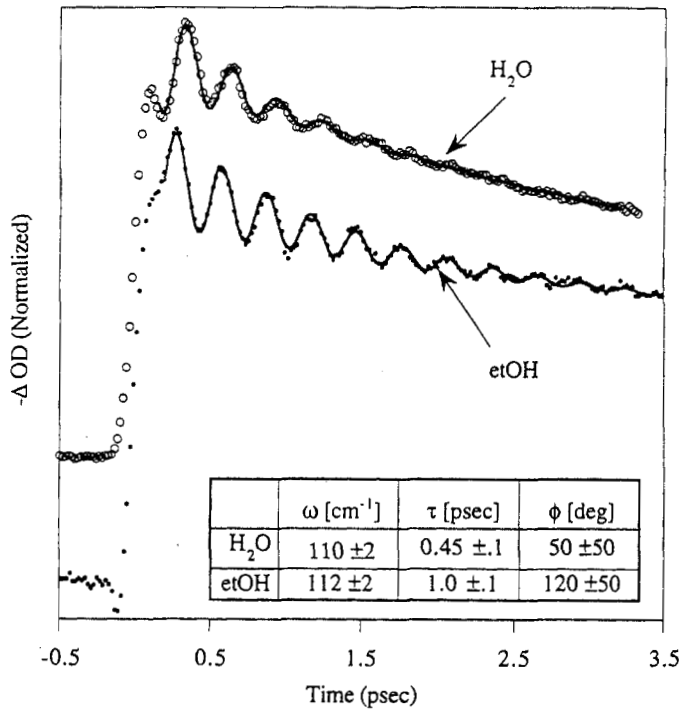

Figure 5. The resonant impulsive stimulated Raman scattering (RISRS) on I_3^- using a UV pump and probe pulse. The spectral modulation corresponds to the symmetric stretch motion of the ground surface.

ization of the underlying chemical physics. This report concentrates on recent developments in this direction.

B. Theoretical Background

The dynamical process describing photodissociation in solution involves many degrees of freedom of the ion-molecule and the surrounding solvent. A full quantum mechanical simulation of the process is therefore prohibitively expensive. For this reason there are two types of approaches to a theoretical investigation of the process:

- Including all relevant degrees of freedom in an approximate fashion.
- Treating the problem exactly within a reduced dimensional model.

To date the theoretical analysis of such systems has proceeded along both these paths. The first approach is usually formulated via the classical mechanics molecular dynamics (MD) setup [11]. If nonadiabatic processes

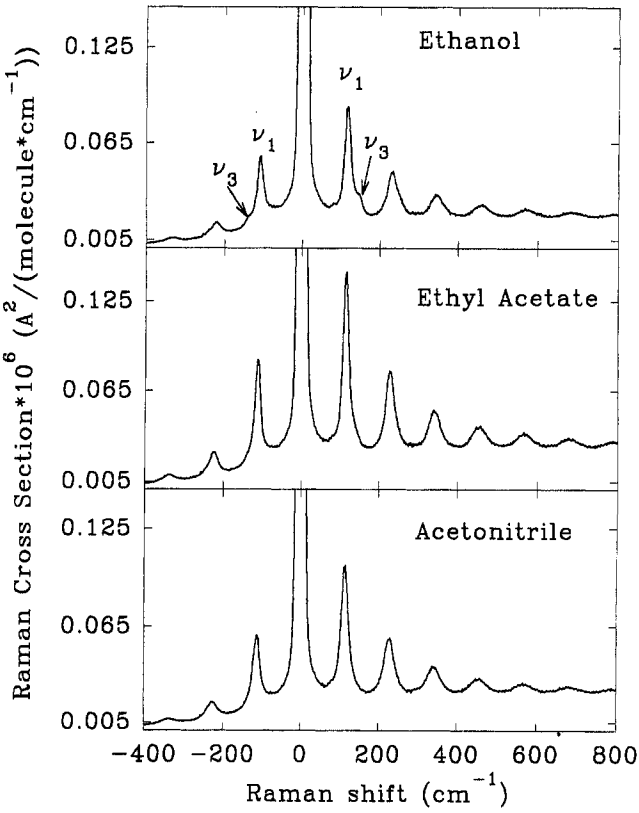

Figure 6. Resonant Raman spectra of I_3^- in three different solvents at 299 nm. ν_1 is the symmetric stretch frequency; ν_3 is the anti-symmetric stretch frequency, visible only in ethanol.

are involved or nuclear quantum phenomena are important, different formulations of quantum-classical simulations have been developed [12, 13, 14, 15, 16, 17].

In this study, the second approach is followed. Even though the participating iodine atoms are heavy and their behavior is expected to be classical, the ultrashort nature of the matter–radiation interaction induces coherent superpositions of quantum states, which should be dealt with in a quantum mechanical framework. An effort was made to include the entire process in this framework. Especially important is the inclusion of the solvent as a quantum species (even if this is only achieved phenomenologically), as it has a profound effect both as a stabilizer and as a destroyer of this quantum coherence.

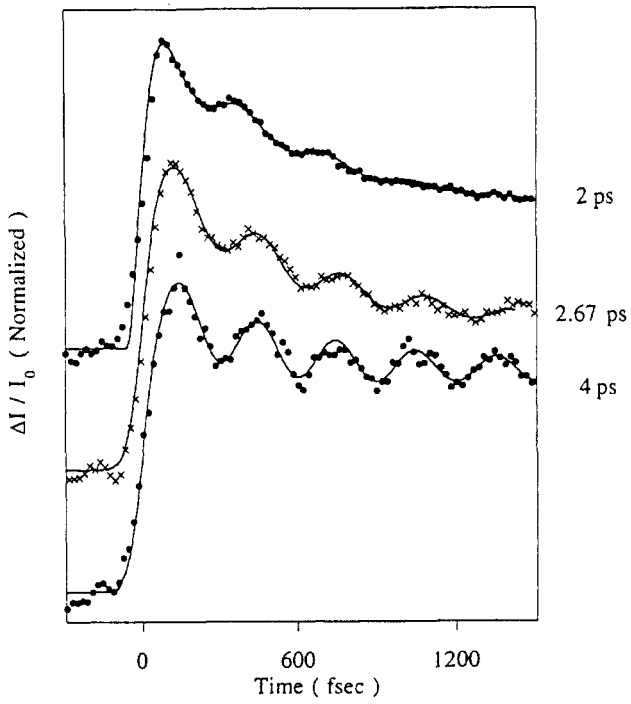

Figure 7. TRISRS data recorded at push delays of 2, 2.7 and 4 ps.

The current work summarizes and expands previous efforts along this direction. The purpose is to supply a complete picture of the theoretical considerations that have been developed in analyzing the I_3^- photodissociation process. The previous theoretical efforts included quantum wave-packet simulations of the photodissociation dynamics [1, 18], analysis of the dynamical "hole" in connection to the RISRS experiments [2, 19], and analysis of the TRISRS experiment utilizing a master equation simulation of the relaxation dynamics [4]. These results are now connected with solvent-induced relaxation dynamics with the purpose of supplying a complete picture.

C. Objective

The main purpose of this work is twofold:

- To develop a complete and general method for a fully quantum mechanical simulation of photodissociation processes in solution.
- To apply this method to a concrete experimental example, to unravel the underlying chemical physics of the processes in the reaction

$$I_3^- \xrightarrow{h\nu} I_2^- + I$$

in solution.

Some additional objectives are:

- Development of a simple uniformly convergent global propagation technique applicable to both Hermitian and non-Hermitian operators. This makes it possible to elegantly calculate all the different types of dynamics involved using a single algorithm.
- Visualization of the quantum state of the system in a way that makes the different components of the dynamics obvious and intuitive.
- Explaining the influence of different dissipation mechanisms on the observed modulations of a nonharmonic oscillator.

D. Outline of the Paper

The guiding principles of the quantum simulation and analysis are the following:

- The system can be represented by a state vector (in the pure case) or a density matrix (when dealing with a statistical ensemble).
- Forces acting on the system are formulated as operators, which induce a change in the state of the system as it evolves in infinitesimal time. These operators generate the dynamics of the system.
- Physical observables are formulated as operators, whose average values (with respect to the state of the system) are the observed measurements.

In Section II the theoretical framework for the quantum mechanical simulation of an impulsive photodissociation process in solution is developed. First, the system should be reduced to a numerically feasible quantum mechanical model, and its initial state must be defined (Section II.A). Second, the operator that generates the dynamics is constructed from the different forces acting within the system. By recursively applying the generator to the initial state, all the dynamical behavior can be reconstructed (Section II.B). Last, the experimentally measurable operators (observables) are constructed and their average value calculated (Section II.C).

In Section III the above framework is applied to an experimental system: the photochemical decomposition of tri-iodide.

$$I_3^- \xrightarrow{h\nu} I_2^- + I$$

The simulation is broken into four parts. In the first, the system is described

by a state vector and follows dissociation induced by the pump pulse (Section III.B). In the second and third, the system is described by a density matrix, demonstrating the influence of the solvent on the spectral modulations observed by two probe pulses: one in the UV (Section III.C), the other in the visible (Section III.D). In the last part, the effect of a delayed push pulse is studied (Section III.E).

Finally, in Section IV, the main results are summarized, and potential extensions and limitations are indicated.

II. METHODS

In this section the theoretical framework for a quantum mechanical simulation and analysis of an impulsive photodissociation process in solution is described.

A. Statics

The representation of a complex quantum mechanical system is discussed. The state of the system should be described in a way that can be processed by computers and visualized by humans. Once this is achieved, the initial state of the system can be cast in this way, as the starting point for the next section.

1. Describing the State of the System

To describe a quantum mechanical state, the Hilbert space of all possible states should be identified by defining the relevant degrees of freedom. Then a basis for this space is chosen. By expanding the state as a linear combination of the basis elements, it can be written as a vector (for a pure state) or a matrix (for a statistical ensemble). A discrete Fourier transform is used to change representations between conjugated basis sets.

a. Degrees of Freedom. The full description of a photodissociating molecule in solution contains the following degrees of freedom (DOF):

- Radiation field (photons) DOF
- Nuclear and electronic DOF for every solvent atom in interaction with the photodissociating species
- Molecular DOF:
  - Electronic
  - Nuclear—translation, rotations, vibrations.

Unlike classical mechanics, which is a local theory and therefore scales linearly with the number of DOF, quantum mechanics is a global theory and

scales exponentially with this number. It becomes prohibitively time-consuming to make a full quantum description of all DOF, and several approximations must be made to reduce the dimensionality of the problem.

The first approximation is to separate the radiation field from the system, and treat it as an external time-dependent variation. The radiation field is taken to be a classical electromagnetic wave, using the rotating wave approximation (RWA). This is a good approximation considering the intensities usually used in photodissociation experiments.

The most drastic reduction in dimensions is gained by separating the DOF of the solvent molecules from the DOF of the photodissociating molecular system, by changing the definition of the system from a closed one (solvent + solute) to an open system (solute only) surrounded by a bath (solvent only). This is done formally by taking a partial trace over the solvent DOF. If no correlations exist between the solvent and solute, the reduced system would remain a pure state, but if such correlations exist, the partial trace will transform the reduced system into a mixed state, and measurements made on the reduced system alone will prove it to be a statistical ensemble. The approximation is not in the trace operation (which is exact, formally), but in the neglect of the correlations with the bath in the dynamics. The bath can be incorporated into the dynamics of the open system by the Liouville von Neumann equation, as a dissipative part formulated within the dynamical semigroup approach [20, 21]. This approximation is good when the "memory" of the bath for correlations with the reduced system is shorter than the timescale of interest. The partition between the system and bath modes is arbitrary. The quality of the approximation improves if more degrees of freedom are included in the primary system. In particular, in solution the "cage" degrees of freedom should be included [22]. In practice, the number of degrees of freedom in the primary system is dictated by the computer resources available.

In the molecular system, the Born–Oppenheimer approximation is used to separate electronic from nuclear DOF, again on the basis of different timescales of the dynamics. The much faster electronic movement creates an effective potential for each configuration of the nuclei, and can be treated as a potential surface in which the nuclei move. Photodissociation experiments involve more than one electronic state simultaneously. In this study a simplifying assumption is used in which only two electronic states are coupled by the pulse at one time, so the electronic DOF can be reduced to the formalism of a two-level system.[1] This approximation is good as long as the electronic potential surfaces do not cross.

[1]Using pseudo-spin notation, $|-\rangle$ and $|+\rangle$ are the lower and upper states of the system, $\hat{\mathbf{P}}_- = |-\rangle\langle-|$ and $\hat{\mathbf{P}}_+ = |+\rangle\langle+|$ are the projection operators on those states, $\hat{\mathbf{S}}_x$, $\hat{\mathbf{S}}_y$, $\hat{\mathbf{S}}_z$ are the angular momentum operators, and $\hat{\mathbf{S}}_-$, $\hat{\mathbf{S}}_+$ are the lowering and raising operators, respectively.

Finally, only the molecular nuclear DOF remain. Here, each system should be studied to obtain the relevant DOF by comparing the timescales of the different motions (for example, rotations are usually much slower than vibrations, and can be neglected from the calculations).

b. Grid and Eigenstate Representations. Two different representations for the nuclear DOF are used throughout this work. The first representation is based on the Fourier method [23]. The state is taken to be a wave function in coordinate space ($\mathbf{r}$), its values sampled on an evenly spaced grid. The spatial extent of the grid is chosen so that the wave function decays exponentially to zero outside its boundaries (finite support). Its density ($\Delta\mathbf{r}$) is chosen to be such that the Fourier transform of the wave function decays exponentially to zero for absolute momentum values $|\mathbf{p}|$ greater than the Nyquist frequency $\mathbf{p}_{max} = h/2\Delta\mathbf{r}$ (band limited). If these conditions are met, the grid representation is equivalent to expansion on a continuous basis of δ-functions in coordinate space $\{|\mathbf{r}\rangle\}$. This basis is a set of eigenstates of the coordinate operator $\hat{\mathbf{R}}$.

The second representation is a discrete basis expansion. The basis is taken as a set of eigenstates of the molecular Hamiltonian operator for the bound ground state, denoted by $|v\rangle$. Since v has the meaning of the energy level of a periodic motion (vibration or rotation), its conjugated variable (via Fourier transform) is the phase of the motion ϕ_v. This pair is known in analytical classical mechanics as *action angle* variables.

A unitary transformation matrix $\mathbf{T}: \mathbf{r} \rightarrow v$ is constructed by finding the grid representation of the eigenstate wavefunctions, using the relaxation method (Eq. 2.42):

$$\mathbf{T}(v, \mathbf{r}) = v(r) = \langle v|\mathbf{r}\rangle \tag{2.1}$$

The transformations $\mathbf{T}$ and $\mathbf{T}^\dagger$ are used to convert states and operators between the two representations.

c. State Vector. The state of the system is represented simultaneously on two electronic surfaces: the initial ground surface and the electromagnetically coupled excited surface. When the system is a pure state Ψ, it can be represented as a pseudo-spin vector

$$\Psi = |\psi_g\rangle \otimes |-\rangle + |\psi_e\rangle \otimes |+\rangle = \begin{pmatrix} \psi_e \\ \psi_g \end{pmatrix} \tag{2.2}$$

where ψ_g, ψ_e are the nuclear wave functions on the ground and excited surfaces, respectively. These wave functions can be expanded as a linear com-

bination of the aforementioned basis sets, and represented as a vector of complex numbers, which are the coefficients of this combination. If there are n degrees of freedom in the system, this vector will be n-dimensional. When expanded in coordinate representation, the coefficients will be denoted by $\psi(\mathbf{r}) = \langle \mathbf{r}|\psi\rangle$, and in eigenstate space by $\psi(v) = \langle v|\psi\rangle$.

d. Density Matrix. When the system is a mixed state, it is no longer possible to represent it as a single state vector. The most general representation is by a density matrix $\hat{\rho}$

$$\hat{\rho} = \hat{\rho}_g \otimes \hat{\mathbf{P}}_- + \hat{\rho}_e \otimes \hat{\mathbf{P}}_+ + \hat{\rho}_c \otimes \hat{\mathbf{S}}_+ + \hat{\rho}_c^\dagger \otimes \hat{\mathbf{S}}_- = \begin{pmatrix} \hat{\rho}_e & \hat{\rho}_c \\ \hat{\rho}_c^\dagger & \hat{\rho}_g \end{pmatrix} \tag{2.3}$$

where $\hat{\rho}_g$, $\hat{\rho}_e$ are the nuclear populations on the ground and excited surfaces, respectively, and $\hat{\rho}_c$ is the nuclear coherence between these surfaces. These nuclear terms can be expanded as a linear combination of operators of the form $|b\rangle\langle b'|$, where $\{|b\rangle\}$ is a basis set. When expanded in coordinate representation, the coefficients form a matrix $\rho(\mathbf{r}, \mathbf{r}') = \langle \mathbf{r}|\hat{\rho}|\mathbf{r}'\rangle$, and in eigenstate space $\rho(v, v') = \langle v|\hat{\rho}|v'\rangle$. If there are n degrees of freedom in the system, those matrixes will be n^2-dimensional.

e. Conjugated Basis Sets. Given a representation of a state vector $|\psi\rangle$ or a density matrix $\hat{\rho}$ in a basis set, it is easy to transform it to its representation in the conjugated basis and back by using a discrete Fourier transform. For the $(\mathbf{r}, \mathbf{p})$ pair

$$\psi(\mathbf{p}) = \frac{1}{\sqrt{2\pi}} \sum_{\mathbf{r}} \psi(\mathbf{r})\, e^{-\frac{i}{\hbar}\mathbf{p}\cdot\mathbf{r}}\, \Delta\mathbf{r} \tag{2.4}$$

$$\psi(\mathbf{r}) = \frac{1}{\sqrt{2\pi}} \sum_{\mathbf{p}} \psi(\mathbf{p})\, e^{\frac{i}{\hbar}\mathbf{p}\cdot\mathbf{r}}\, \Delta\mathbf{p} \tag{2.5}$$

$$\rho(\mathbf{p}, \mathbf{p}') = \frac{1}{2\pi} \sum_{\mathbf{r}, \mathbf{r}'} e^{-\frac{i}{\hbar}\mathbf{p}\cdot\mathbf{r}}\, \rho(\mathbf{r}, \mathbf{r}')\, e^{\frac{i}{\hbar}\mathbf{p}'\cdot\mathbf{r}'}\, \Delta\mathbf{r}\Delta\mathbf{r}' \tag{2.6}$$

$$\rho(\mathbf{r}, \mathbf{r}') = \frac{1}{2\pi} \sum_{\mathbf{p}, \mathbf{p}'} e^{\frac{i}{\hbar}\mathbf{p}\cdot\mathbf{r}}\, \rho(\mathbf{p}, \mathbf{p}')\, e^{-\frac{i}{\hbar}\mathbf{p}'\cdot\mathbf{r}'}\, \Delta\mathbf{p}\Delta\mathbf{p}' \tag{2.7}$$

and similarly for the (v, ϕ_v) pair. These transformations can be calculated very efficiently using parallelized fast Fourier transform (FFT) algorithms.

2. *Visualizing the State of the System*

To gain insight on the processes under study, it is important to be able to visualize the quantum mechanical state of the system. Two ways are presented to extract graphical information from the nuclear parts of the system $(\psi_g, \psi_e, \rho_g, \rho_e)$.

A Single Basis Picture. Each basis is a set of eigenstates $\{|b\rangle\}$ of an operator $\hat{\mathbf{O}}$. Once a basis set is selected, and the state $|\psi\rangle$ is expanded in this basis, the probability of finding the result associated with $|b\rangle$ in a measurement of $\hat{\mathbf{O}}$ is $|\psi(b)|$.[2] For a density matrix $\hat{\rho}$, this probability is the diagonal element $\rho(b,b)$. Plotting these probabilities gives a picture of the distribution with respect to a single basis: coordinate distribution for the $\{|\mathbf{r}\rangle\}$ representation, momentum distribution for $\{|\mathbf{p}\rangle\}$, energy distribution for $\{|v\rangle\}$, and phase distribution for $\{|\phi_v\rangle\}$.

Phase Space Picture. A broader picture can be constructed by crossing the information gained from two conjugated representations, revealing the correlations between the conjugated properties. This is done by constructing a phase-space picture of the density matrix,[2] using the Wigner distribution function [24]

$$W(r,p) = \frac{1}{2\pi} \int e^{ipy} \rho\left(r - \frac{1}{2}\, y, r + \frac{1}{2}\, y\right)\, dy \tag{2.8}$$

$$W(v,\phi_v) = \frac{1}{2\pi} \int e^{i\phi_v y} \rho\left(v - \frac{1}{2}\, y, v + \frac{1}{2}\, y\right)\, dy \tag{2.9}$$

The naive interpretation of $W(r,p)[W(v,\phi_v)]$ is the probability of finding the system simultaneously at position r and momentum p [energy v and phase ϕ_v]. Care must be taken when using this interpretation, as there is no meaning for an area smaller than h in phase space, because of Heisenberg's uncertainty principle. Therefore the meaning of probability is associated with integration on an area, not with a specific value (which can be negative!). In particular,

$$\int_r W(r,p)\, dr = \rho(p,p) \tag{2.10}$$

[2]In the case of a state vector $|\psi\rangle$, it can easily be transformed into its associated pure state density matrix $|\psi\rangle\langle\psi|$.

$$\int_p W(r,p)\,dp = \rho(r,r) \tag{2.11}$$

$$\int_v W(v,\phi_v)\,dv = \rho(\phi_v,\phi_v) \tag{2.12}$$

$$\int_{\phi_v} W(v,\phi_v)\,d\phi_v = \rho(v,v) \tag{2.13}$$

i.e., the projections of the Wigner distribution function on a basis give back the single basis picture.

The two phase space pictures $W(r,p)$ and $W(v,\phi_v)$ are complimentary, and reveal different aspects of the dynamics, so both are used side by side in this work. Fig. 8 shows the relation between the two coordinate sets.

3. *Initial States*

Before the application of the laser pulse, the system is in thermal equilibrium with the bath, which is a mixed state $\hat{\rho}$. Because of the large energy gap between electronic surfaces, at room temperature it resides entirely on the ground electronic surface:

$$\hat{\rho}_e = 0 \tag{2.14}$$

$$\hat{\rho}_c = 0 \tag{2.15}$$

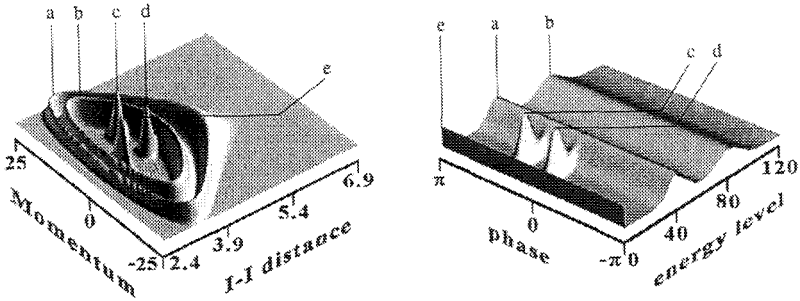

Figure 8. The Wigner distribution function $W_g(r,p)$ and $W_g(v,\phi_v)$ of an artificially mixed state of I_2^- (this distribution is only for illustration, and bears no physical significance). Depicted are two totally dephased states (a, b centered at v = 80, 40), two coherent states (c, d centered at v = 20 and $\phi_v = \pi/3$, 0) and the ground state (e) which is compact in (r,p) but phase independent in (v,ϕ_v). The ridges of the two dephased states in (r,p) mark the energy iso-lines, which in (v,ϕ_v) are straight lines through the respective ridges at v = 40, 80. The angle between the peaks of the two coherent states and the ground state in (r,p) is the distance between their peaks in (v,ϕ_v). Distances are in Å, and the momentum units are Å/ps.

which also means that no correlation exists between the ground and excited electronic surfaces. The statistical mechanical postulate that at equilibrium the phase of all quantum states is random, means that $\rho_g(v, v')$ is diagonal.[3] In an open system, the diagonal elements obey the Boltzmann distribution:

$$\rho_g(v, v) = \frac{e^{-E_v/k_bT}}{\sum_v e^{-E_v/k_bT}} \tag{2.16}$$

where E_v is the energy of the eigenstate $|v\rangle$.

B. Dynamics

The dynamics of a quantum system is governed by one of the following equations: The Schrödinger equation, Eq. (2.17), for a state vector, and the Liouville von Neumann equation, Eq. (2.18), for a density matrix.

$$i\hbar \frac{\partial}{\partial t} |\psi\rangle = \hat{\mathbf{H}}|\psi\rangle \tag{2.17}$$

$$i\hbar \frac{\partial}{\partial t} \hat{\rho} = \hat{\mathcal{L}}(\hat{\rho}) \tag{2.18}$$

where $\hat{\mathbf{H}}$ is called the Hamiltonian operator, and $\hat{\mathcal{L}}$ is the Liouvillian super-operator. In the case of a closed system, the dynamics are purely Hamiltonian, and $\hat{\mathcal{L}}$ is derived directly from $\hat{\mathbf{H}}$

$$\hat{\mathcal{L}} = \hat{\mathcal{L}}_H(\hat{\rho}) = [\hat{\mathbf{H}}, \hat{\rho}] \tag{2.19}$$

In an open system, a dissipative term is added to the Liouvillian which describes the interactions with the bath

$$\hat{\mathcal{L}} = \hat{\mathcal{L}}_H + i\hbar\hat{\mathcal{L}}_D(\hat{\rho}) \tag{2.20}$$

This section deals with the dynamics originating from the above equations. The structure of the Hamiltonian and the dissipative super-operators of the Liouvillian will be presented, followed by a numerical algorithm for propagating a state in time.

[3]This can be seen by calculating the Wigner distribution function of a diagonal matrix $\rho(v, v)$. This gives $W(v_0, \phi_v) = const$, i.e., for a given eigenstate $|v_0\rangle$, all phases are equally probable.

1. *The Hamiltonian Operator*

The evolution of a state can be divided into periods that are influenced by the radiation field, and of field-free evolution. In the field-free periods, there is no coupling between the electronic components of the state, therefore each nuclear component can be propagated independently. In this case, two separate Hamiltonians are used for the propagation of the ground and excited surface components. These are simply a sum of the kinetic and potential energy operators

$$\hat{\mathbf{H}}_{g/e} = \hat{\mathbf{T}} + \hat{\mathbf{V}}_{g/e} = \frac{\hat{\mathbf{P}}^2}{2m} + V_{g/e}(\mathbf{r}) \tag{2.21}$$

where $V_g(\mathbf{r})$ and $V_e(\mathbf{r})$ are the ground and excited state potential surfaces, respectively.

In the presence of the electromagnetic field, the two surfaces are coupled with the interaction of the field with the dipole moment operator

$$\begin{aligned}\hat{\mathbf{H}} &= \hat{\mathbf{H}}_g \otimes \hat{\mathbf{P}}_- + \hat{\mathbf{H}}_e \otimes \hat{\mathbf{P}}_+ + \epsilon(t)\hat{\mu} \otimes \hat{\mathbf{S}}_+ + \epsilon(t)^*\hat{\mu} \otimes \hat{\mathbf{S}}_- \\ &= \begin{pmatrix} \hat{\mathbf{H}}_e & \epsilon(t)\hat{\mu} \\ \epsilon(t)^*\hat{\mu} & \hat{\mathbf{H}}_g \end{pmatrix}\end{aligned} \tag{2.22}$$

where $\hat{\mathbf{H}}_{e/g}$ are the surface Hamiltonians, $\epsilon(t)$ is the time-dependent field, and $\hat{\mu}$ is the electronic transition dipole. Using the rotating-wave approximation, the field can be written as:

$$\epsilon(t) = \bar{\epsilon}(t)e^{-i\omega_L t} \tag{2.23}$$

where ω_L is the carrier frequency of the laser, and $\bar{\epsilon}(t)$ is the envelope of the pulse. To avoid the fast oscillating carrier frequency, a rotating-frame approach is used. A rotation operator is defined to transform the state

$$\hat{\mathbf{R}}(\omega_L t) = e^{i\omega_L t\hat{\mathbf{S}}_z} \tag{2.24}$$

$$|\tilde{\psi}\rangle = \hat{\mathbf{R}}(\omega_L t)|\psi\rangle \tag{2.25}$$

$$\hat{\tilde{\rho}} = \hat{\mathbf{R}}(\omega_L t)\hat{\rho}\hat{\mathbf{R}}^{\dagger}(\omega_L t) \tag{2.26}$$

In this representation, the equation of motion for a state vector is[4]

$$
\begin{aligned}
i\hbar \frac{\partial}{\partial t} |\tilde{\psi}\rangle &= i\hbar \frac{\partial}{\partial t} (\hat{\mathbf{R}}(\omega_L t)|\psi\rangle) \\
&= i\hbar \frac{\partial \hat{\mathbf{R}}(\omega_L t)}{\partial t} |\psi\rangle + i\hbar \hat{\mathbf{R}}(\omega_L t) \frac{\partial}{\partial t} |\psi\rangle \\
&= -\hbar\omega_L \hat{\mathbf{S}}_z \hat{\mathbf{R}}(\omega_L t)|\psi\rangle + \hat{\mathbf{R}}(\omega_L t)\hat{\mathbf{H}}|\psi\rangle \\
&= -\hbar\omega_L \hat{\mathbf{S}}_z \hat{\mathbf{R}}(\omega_L t)|\psi\rangle \\
&\quad + (\hat{\mathbf{H}} - \bar{\epsilon}(t)e^{-i\omega_L t}\hat{\mu}\hat{\mathbf{S}}_+ - \bar{\epsilon}(t)e^{i\omega_L t}\hat{\mu}\hat{\mathbf{S}}_- + 2\bar{\epsilon}(t)\hat{\mu}\hat{\mathbf{S}}_x)\hat{\mathbf{R}}(\omega_L t)|\psi\rangle \\
&= ((\hat{\mathbf{H}}_g + \hbar\omega_L/2) \otimes \hat{\mathbf{P}}_- + (\hat{\mathbf{H}}_e - \hbar\omega_L/2) \otimes \hat{\mathbf{P}}_+ + 2\bar{\epsilon}(t)\hat{\mu} \otimes \hat{\mathbf{S}}_x)|\tilde{\psi}\rangle \\
&= \tilde{\mathbf{H}}|\tilde{\psi}\rangle
\end{aligned}
\tag{2.27}
$$

Thus, working in the rotating frame, we can substitute the Hamiltonian of the system $\hat{\mathbf{H}}$ with an effective Hamiltonian

$$
\tilde{\mathbf{H}} = \begin{pmatrix} \hat{\mathbf{H}}_e - \hbar\omega_L/2 & \bar{\epsilon}(t)\hat{\mu} \\ \bar{\epsilon}(t)\hat{\mu} & \hat{\mathbf{H}}_g + \hbar\omega_L/2 \end{pmatrix} \tag{2.28}
$$

In the effective Hamiltonian the potential surfaces are closer by an amount equal to the photon energy $\hbar\omega_L$, and the time dependence is only in the slowly varying pulse envelope.

Calculating the Hamiltonian in Coordinate Representation. An efficient way for numerically calculating the operation of the Hamiltonian for a state in the coordinate representation is the Fourier method [23]. It is based on two facts: First, the Hamiltonian is composed of operators that are local in either the coordinate or momentum representations as in Eq. (2.21); second, there is an efficient way to transform a state between the two representations as in Eqs. (2.4–2.7). A local operator means that its representation in the appropriate basis reduces to a diagonal matrix. Specifically, applying the kinetic energy operator to a state in the coordinate representation requires:

[4]It is helpful to note that $[\hat{\mathbf{S}}_+, \hat{\mathbf{R}}(\theta)] = (1 - e^{i\theta})\hat{\mathbf{S}}_+\hat{\mathbf{R}}(\theta)$ and $[\hat{\mathbf{S}}_-, \hat{\mathbf{R}}(\theta)] = (1 - e^{-i\theta})\hat{\mathbf{S}}_-\hat{\mathbf{R}}(\theta)$, so that $[\hat{\mathbf{H}}, \hat{\mathbf{R}}(\theta)] = \bar{\epsilon}(t)\hat{\mu}(e^{-i\theta}\hat{\mathbf{S}}_+ + e^{i\theta}\hat{\mathbf{S}}_- - 2\hat{\mathbf{S}}_x)\hat{\mathbf{R}}(\theta)$.

1. Transforming the state into momentum representation as in Eq. (2.4).
2. Multiplying each momentum grid point p by $p^2/2m$.
3. Transforming the state back into coordinate representation as in Eq. (2.5).

Applying the potential energy operator to a state in the coordinate representation is simpler: just multiply each grid point by the value of the potential at that point.

Calculating the Hamiltonian in Eigenstate Representation. In eigenstate representation the Hamiltonian takes the form a matrix. Its operation on a state vector or a density matrix is simply done by matrix–vector or matrix–matrix multiplication (for which optimized parallel algorithms exist). The Hamiltonian matrix is constructed from the respective matrix elements

$$\mathbf{H}(v', v) = \langle v' | \hat{\mathbf{H}} | v \rangle \tag{2.29}$$

where the operation $\hat{\mathbf{H}}|v\rangle$ is calculated in coordinate representation using the Fourier algorithm.

2. *The Dissipative Super-Operators*

The relaxation dynamics under study involves the dynamical behavior of a quantum mechanical molecular system in a solvent. On a purely Hamiltonian level, the overall system can be described by the Hamiltonian

$$\hat{\mathbf{H}} = \hat{\mathbf{H}}_S + \hat{\mathbf{H}}_B + \hat{\mathbf{H}}_{SB} \tag{2.30}$$

Here $\hat{\mathbf{H}}_S$, $\hat{\mathbf{H}}_B$, and $\hat{\mathbf{H}}_{SB}$ stand, respectively, for system, bath and system–bath interaction. To obtain a traceable computation scheme the full dynamics is replaced with an appropriate reduced dynamics within the subspace of the quantum mechanical system. The interaction of the system with the bath can be represented in the form

$$\hat{\mathbf{H}}_{SB} = \sum_i \hat{\mathbf{V}}_i \hat{\mathbf{B}}_i \Gamma_i \tag{2.31}$$

where Γ_i is the interaction strength, and $\hat{\mathbf{V}}_i$, $\hat{\mathbf{B}}_i$ are operators of the system and of the bath, respectively. By reducing these interaction terms to the system coordinates alone, the influence of the bath can be described by a dissipative term $\mathcal{L}_D$. Using general arguments based on positivity and causality, the semi-group analysis derives for the dissipative term $\mathcal{L}_D$ in the form [20, 21, 25]

$$\mathcal{L}_D(\hat{\rho}) = \sum_i \gamma_i \left(\hat{\mathbf{V}}_i \hat{\rho} \hat{\mathbf{V}}_i^\dagger - \frac{1}{2} \{ \hat{\mathbf{V}}_i \hat{\mathbf{V}}_i^\dagger, \hat{\rho} \}_+ \right) \tag{2.32}$$

where the parameters γ_i are amplitudes describing the relaxation. This is a general formulation, and the parameters γ_i and the operators $\hat{\mathbf{V}}_i$ characterize the dissipation process.

In analyzing dissipative processes in solution, there are three specific, important cases of Eq. (2.32) that should be considered:

1. If $\mathbf{V}$ is unitary, Eq. (2.32) collapses to

$$\hat{\mathcal{L}}_D(\hat{\rho}) = \sum_i \gamma_i (\hat{\mathbf{V}}_i \hat{\rho} \hat{\mathbf{V}}_i^\dagger - \hat{\rho}) \tag{2.33}$$

   This form is appropriate for what might be referred to as Poisson processes: i.e., for processes in which the system suffers isolated changes due to sudden interactions with the environment—the isolated binary collision model is an obvious example. Under these conditions, the operator $\hat{\mathbf{V}}_i$ becomes the S matrix of a collision with particles of the environment. The process is characterized by a sum of independent uncorrelated scattering events acting on the molecular subsystem at a rate γ_i.
2. By setting $\hat{\mathbf{V}}_i$ to be Hermitian, Eq. (2.32) becomes

$$\hat{\mathcal{L}}_D(\hat{\rho}) = -\frac{1}{2} \sum_i \gamma_i [\hat{\mathbf{V}}_i, [\hat{\mathbf{V}}_i, \hat{\rho}]] \tag{2.34}$$

   The form is characteristic of a system strongly driven by a Gaussian random process. It can be derived directly for a quantum system coupled to a stochastic process [26], or driven by a δ-correlated random noise [27].
3. The third common case of Eq. (2.32) is of energy pooling. This case describes a relaxation through resonant energy transfer between the system and bath. It is best described by choosing as the operator $\hat{\mathbf{V}}_i$ in Eq. (2.32) as the raising or lowering operators of the systems manifold. Figure 9(*a*, *b*) demonstrates the energy relaxation of a harmonic oscillator starting from a coherent state. It should be noticed that the shape of the probability density stays compact throughout the process. The dephasing accompanying the energy relaxation can be interpreted as a geometric effect of increase of solid angle as the density moves toward the origin.

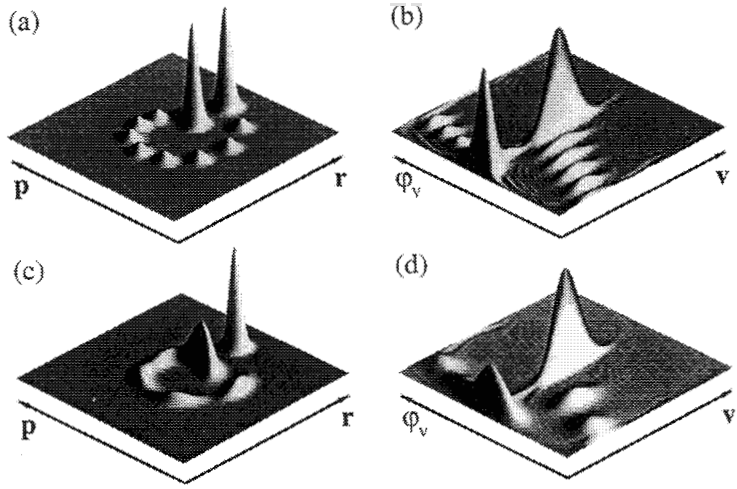

Figure 9. Relaxation dynamics of a harmonic oscillator. An initial coherent state positioned at the outer turning point is propagated for one period. A stroboscopic display is shown, in which the first and last states are enhanced by a factor of 10. The upper panels show an energy relaxation process in Eq. (2.32), where the operator $\hat{\mathbf{V}} = \hat{\mathbf{a}}$ describes relaxation to zero temperature. The relaxation parameter $\gamma = 0.3\omega$, the oscillator frequency. A time interval of $1/10\omega^{-1}$ between snapshots is used. The left panels show the Wigner distribution $W(r,p)$, while the right panels show the Wigner distribution $W(v,\phi_v)$. Notice in panel (b) that energy relaxation is accompanied by broadening in the phase distribution due to the approach of the distribution to the zero energy origin. The lower panels shows a combined dephasing, as in Eq. (2.35), and energy relaxation process, $\gamma_d = 0.015\omega^2$. A time interval of $1/5\omega^{-1}$ between shapshots is used.

A pure dephasing process is defined by an energy conserving dissipation process. Based on the Poisson and Gaussian dissipation, a pure dephasing process can be constructed. In a Gaussian process this amounts to choosing $\hat{\mathbf{V}}_i$ to be a function of the Hamiltonian operator $\hat{\mathbf{V}}_i = f(\hat{\mathbf{H}})$. Keeping only the linear term leads to

$$\hat{\mathcal{L}}_D(\hat{\rho}) = -\tfrac{1}{2}\,\gamma_d[\hat{\mathbf{H}},[\hat{\mathbf{H}},\hat{\rho}]] \tag{2.35}$$

Figure 9(c, d) demonstrates a Gaussian dephasing process of the harmonic oscillator. This dissipative process can be derived from δ-correlated random fluctuations in the oscillator's frequency.

A pure dephasing Poisson process can be constructed from the unitary operator $\hat{\mathbf{V}}_i = \exp(-\frac{i}{\hbar}\hat{\mathbf{H}}\tau)$, leading to

$$\hat{\mathcal{L}}_D(\hat{\rho}) = \gamma_d(e^{-\frac{i}{\hbar}\hat{\mathbf{H}}\tau}\hat{\rho}e^{\frac{i}{\hbar}\hat{\mathbf{H}}\tau} - \hat{\rho}) \tag{2.36}$$

where τ is a characteristic time parameter. The origin of this process can be elastic collisions of the system with solvent particles. Considering τ to be from a Gaussian distribution, $p(\tau) = 1/\sqrt{2\pi\sigma_\tau}\exp(-\tau^2/2\sigma_\tau^2)$, the dephasing generator becomes

$$\hat{\mathcal{L}}_D(\hat{\rho}) = \gamma_d(e^{-\frac{\sigma_\tau}{\hbar^2}[\hat{\mathbf{H}},\hat{\mathbf{H}},\ ]}\hat{\rho} - \hat{\rho}) \tag{2.37}$$

where the exponent is interpreted as a power expansion. The leading term of Eq. (2.37) is equivalent to Eq. (2.35); therefore only Gaussian dephasing processes will be considered in this study.

The three dissipative processes are the building blocks for constructing the dissipative superoperator for the photo-induced dynamics of I_3^-.

A phase space approach to dissipative dynamics in solution and its relation to classical mechanics has been the subject of a recent effort by Kohen and Tannor [28].

An alternative to the present approach is to construct the dissipative superoperator through a second-order perturbation expansion in the system–bath coupling constant. This expansion relates the dissipative constants γ_i to Fourier transforms of bath correlation functions [29, 30, 21, 31, 32]. This approach has been employed by Pugliano et al. [10] to calculate the relaxation coefficients in a master equation calculation for the vibrational relaxation of IHgI. The correlation functions are then calculated by a MD simulation of the solvent. For the I_3^- system, detailed knowledge of the bath correlation functions and the system–bath interactions is lacking. This justifies, at this stage, the phenomenological approach; in the future, the results can be related to detailed information on the solvent.

3. *The Evolution Operator*

From the differential equations in Eq. (2.17) and (2.18) an integral evolution operator and super-operator are constructed

$$|\psi\rangle(t') = \hat{\mathbf{U}}(t,t')|\psi\rangle(t) \tag{2.38}$$

$$\hat{\rho}(t') = \hat{\mathcal{U}}(t,t')\hat{\rho}(t) \tag{2.39}$$

In the case of a time-independent Hamiltonian, the integration is simple

$$\hat{\mathbf{U}}(t,t+\Delta t) = e^{-\frac{i}{\hbar}\hat{\mathbf{H}}\Delta t} \tag{2.40}$$

$$\hat{\mathcal{U}}(t,t+\Delta t) = e^{-\frac{i}{\hbar}\hat{\mathcal{L}}\Delta t} \tag{2.41}$$

and is exact for any Δt. A small variation on this equation is used to find the eigenstates of the ground state Hamiltonian $\hat{\mathbf{H}}_g|\phi_n\rangle = E_n|\phi_n\rangle$. Since $\{|\phi_n\rangle\}$ is a basis set, an arbitrary state can be written as $|\psi\rangle(0) = \Sigma_n a_n|\phi_n\rangle$. Using an imaginary time step in Eq. (2.41) results in

$$|\psi\rangle(t) = \hat{\mathbf{U}}(0, -i\Delta t)|\psi\rangle(0) = e^{-\frac{1}{\hbar}\hat{\mathbf{H}}\Delta t} = \sum_n a_n|\phi_n\rangle$$

$$= \sum_n a_n e^{-\frac{1}{\hbar}E_n\Delta t}|\phi_n\rangle \tag{2.42}$$

The decay of contributions from eigenstates with higher energy is exponentially faster than for ones with a lower energy, so Eq. (2.42) will quickly converge to

$$|\psi\rangle(t) \propto |\phi_0\rangle \tag{2.43}$$

which is the lowest eigenstate. Taking $|\psi'\rangle = |\psi\rangle - \langle\phi_0|\psi\rangle|\phi_0\rangle$ as the initial state will result in the next eigenstate $|\phi_1\rangle$, and so on.

When the evolution is induced by the radiation field, the Hamiltonian becomes time-dependent and Eq. (2.41) has to be amended by time ordering. The first-order Magnus expansion was employed [33] to approximate the evolution operator

$$\hat{\mathbf{U}}(t, t+\Delta t) = \exp\left[-\frac{i}{\hbar}\left(\int_t^{t+\Delta t} \frac{\hat{\mathbf{H}}(t')\,dt'}{\Delta t}\right)\cdot \Delta t\right] \tag{2.44}$$

$$\hat{\mathcal{U}}(t, t+\Delta t) = \exp\left[-\frac{i}{\hbar}\left(\int_t^{t+\Delta t} \frac{\hat{\mathcal{L}}_H(t')\,dt'}{\Delta t} + \hat{\mathcal{L}}_D\right)\Delta t\right] \tag{2.45}$$

This amounts to averaging the Hamiltonian over each time step, so Δt should be small in comparison with the rate of change in the pulse amplitude.

All the equations for the evolution operator and super-operator have the same functional form

$$f(\hat{\mathbf{O}}) = e^{-\frac{i}{\hbar}\hat{\mathbf{O}}\Delta t} \tag{2.46}$$

The basic idea underlying the propagation algorithm is that approximating a function of an operator is equivalent to approximating a scalar function in the domain of eigenvalues of this operator [34]. The scalar function is

approximated by the Newton interpolation polynomial:

$$f(z) \approx \mathcal{P}_{N-1}(z) \equiv \sum_{n=0}^{N-1} a_n \prod_{j=0}^{n-1} (z - x_j) \tag{2.47}$$

where the x_j's are interpolation points in which the value of $f(x_j)$ is sampled, and the a_n's are the expansion coefficients calculated to give $f(x_j) \equiv \mathcal{P}(x_j)$.

If the approximation is good for all the scalars that are equal to eigenvalues of an operator, then it is a good approximation for the function of this operator. For this procedure to work, a uniformly convergent method has to be applied to sum the power series into the different final results. The Chebychev polynomial expansion [35] has uniform convergence properties and therefore has been utilized in both time-dependent and time-independent calculations, but its interpolation domain lies on the real axis, so it has a very limited support for non-Hermitian operators. Since the dissipative terms in the Liouville von Neumann equation are anti-Hermitian, a different method had to be developed, in which the interpolation points reside in the complex plane. This method is the Newton interpolation with Leja interpolation points [18], which is detailed in the Appendix.

Once the interpolation points are chosen and the coefficients calculated, the function of the operator can be calculated by recursively applying the operator to an initial state, and summing the resulting polynomial. For example, if $\hat{\mathcal{L}}$ is the time-independent Liouvillian of the system, and

$$f(z) = e^{-\frac{i}{\hbar} z \Delta t} \approx \mathcal{P}_{N-1}(z) \tag{2.48}$$

for all z residing in the complex eigenvalue range of $\hat{\mathcal{L}}$, then

$$\hat{\rho}(t + \Delta t) = \hat{\mathcal{U}}(t, t + \Delta t)\hat{\rho}(t) \approx \mathcal{P}(\hat{\mathcal{L}})\hat{\rho}(t) \tag{2.49}$$

C. Interpretation

The primary interrogation tool of the photodissociation dynamics is light–matter interaction. A combination of CW and pump-probe spectroscopic experiments are then to be used. Theoretically, physical measurements applied to the system can be calculated through the use of observables, which are operators associated with the measurement process. The ability to separate the dynamics from the observation is based on the use of weak electromagnetic interactions, for which the perturbation of the system is limited. This section describes the construction of the relevant observables for a pump-probe photodissociation experiment.

1. The Impulsive Excitation Picture

When the pulse is short on the timescale of nuclear motion, and long compared to the timescale defined by the electronic excitation, the construction of observables associated with this pulse can be simplified using the impulsive two-level coordinate-dependent approximation.

a. The Coordinate-Dependent Two-Level Approximation. The starting point is a rearrangement of the effective Hamiltonian [Eq. (2.28)] defining the difference potential

$$2\hat{\mathbf{\Delta}}(\mathbf{r}) = \hat{\mathbf{V}}_e(\mathbf{r}) - \hat{\mathbf{V}}_g(\mathbf{r}) - \hbar\omega_L \tag{2.50}$$

This leads to the modified Hamiltonian

$$\tilde{\mathbf{H}} = \begin{pmatrix} \hat{\mathbf{\Delta}} & \hat{\mathbf{W}} \\ \hat{\mathbf{W}} & -\hat{\mathbf{\Delta}} \end{pmatrix} + \begin{pmatrix} \hat{\mathbf{\Delta}} & 0 \\ 0 & \hat{\mathbf{\Delta}} \end{pmatrix} + \begin{pmatrix} \hat{\mathbf{H}}_g & 0 \\ 0 & \hat{\mathbf{H}}_g \end{pmatrix} \tag{2.51}$$

where the time-dependent transition operator $\hat{\mathbf{W}} = -\bar{\epsilon}\hat{\mu}$ is also defined. This partition of the effective Hamiltonian is the basis for the definition

$$\tilde{\mathbf{H}} = \hat{\mathbf{H}}_3 + \hat{\mathbf{H}}_2 + \hat{\mathbf{H}}_1 \tag{2.52}$$

using spin notation

$$\hat{\mathbf{H}}_1 = \hat{\mathbf{H}}_g \otimes \hat{\mathbf{I}} \qquad \hat{\mathbf{H}}_2 = \hat{\Delta}(\mathbf{r}) \otimes \hat{\mathbf{I}} \qquad \hat{\mathbf{H}}_3 = 2\hat{\mathbf{W}}(\mathbf{r}, \mathbf{t}) \otimes \tilde{\mathbf{S}}_x + 2\hat{\Delta}(\mathbf{r}) \otimes \hat{\mathbf{S}}_z \tag{2.52a}$$

The original Hamiltonian has been partitioned into a direct product of spatially dependent operators and spin operators.

The partitioning of the Hamiltonian is the basis for approximating the evolution operator that propagates the wave function for a pulse duration t_f, as a product of terms

$$\hat{\mathbf{U}}(t_f) = e^{-\frac{i}{\hbar}\tilde{\mathbf{H}}t_f} \approx e^{-\frac{i}{\hbar}\hat{\mathbf{H}}_3 t_f} e^{-\frac{i}{\hbar}\hat{\mathbf{H}}_2 t_f} e^{-\frac{i}{\hbar}\hat{\mathbf{H}}_1 t_f} \tag{2.53}$$

The approximation is based on the Trotter formula [36]. Its use is well known in the split operator propagation method for the time-dependent Schrödinger equation introduced by Fiet and Fleck [37, 38]. The approximate evolution operator in Eq. (2.53) is used to propagate an initial wave function that is exclusively on the ground surface, for a pulse duration t_f

$$\Psi(\mathbf{r},0) = \begin{pmatrix} 0 \\ \psi_g(\mathbf{r},0) \end{pmatrix} \tag{2.54}$$

A simple case is of an initially stationary wave function at $t = 0$, i.e., $\hat{\mathbf{H}}_\mathbf{g}\psi_g(\mathbf{r},0) = E_g\psi_g(\mathbf{r},0)$. The operation of the propagator $e^{-\hat{\mathbf{H}}_1 t}$ on $\Psi(0)$ will lead to a global phase shift

$$\Psi_1 = e^{-\frac{i}{\hbar}\hat{\mathbf{H}}_1 t_f}\Psi(0) = e^{-\frac{i}{\hbar}E_g t_f}\Psi(0) \tag{2.55}$$

The next step is to propagate with $e^{-\frac{i}{\hbar}\hat{\mathbf{H}}_2 t_f}$

$$\Psi_2 = e^{-\frac{i}{\hbar}\hat{\mathbf{H}}_2 t_f}\Psi_1 = e^{-\frac{i}{\hbar}E_g t_f}\begin{pmatrix} 0 \\ e^{-\frac{i}{\hbar}\hat{\Delta} t_f}\psi_g(\mathbf{r},0) \end{pmatrix} \tag{2.56}$$

The operator $\exp(-\frac{i}{\hbar}\hat{\mathbf{\Delta}}(\mathbf{r})t_f)$ causes a momentum change in ψ_g, since $\hat{\mathbf{\Delta}}(\mathbf{r})$ is a function of $\mathbf{r}$.

The final step is to operate with $\exp(-\frac{i}{\hbar}\hat{\mathbf{H}}_3 t_f)$ on Ψ_2. Since $\hat{\mathbf{H}}_3$ is not diagonal in the g/e representation, $\hat{\mathbf{H}}_3$ is diagonalized for each position $\mathbf{r}$. At this point it is assumed that the field envelope $\bar{\epsilon}$ is constant. This amounts to a square pulse shape. For a nonsquare pulse, $\hat{\mathbf{W}}(r,t)$ is approximated as [39]:

$$\hat{\mathbf{W}} \approx \hat{\mu}\,\frac{1}{t_f}\int_0^{t_f}\bar{\epsilon}(t')\,dt' \tag{2.56a}$$

Closed form expressions can be obtained also for $\epsilon(t) = \bar{\epsilon}\,\mathrm{sech}(t)/\tau$ [40]. The eigenvalue equation of the Hamiltonian $\mathbf{H}_3$ becomes $(\lambda+\Delta)(\lambda-\Delta)-W^2 = 0$, leading to

$$\lambda_{1,2} = \pm\sqrt{W^2+\Delta^2} \tag{2.57}$$

The diagonalization matrixes can be described as a rotation matrix for each position $\mathbf{r}$ [41]

$$\hat{\mathbf{S}}(\mathbf{r}) = e^{-i\theta(\mathbf{r})\tilde{\mathbf{S}}_\mathbf{y}} = \begin{pmatrix} \cos\theta/2 & -\sin\theta/2 \\ \sin\theta/2 & \cos\theta/2 \end{pmatrix} \tag{2.58}$$

where: $\tan\theta(\mathbf{r}) = \frac{|\hat{\mathbf{W}}|}{\hat{\Delta}}$. With this form the propagator for each spatial point $\mathbf{r}$

becomes

$$e^{-\frac{i}{\hbar}\hat{\mathbf{H}}_3 t_f} = \mathbf{S}^{-1}(\mathbf{r}) \begin{pmatrix} e^{-\frac{i}{\hbar}\lambda_1 t_f} & 0 \\ 0 & e^{-\frac{i}{\hbar}\lambda_2 t_f} \end{pmatrix} \mathbf{S}(\mathbf{r}) \tag{2.59}$$

For convenience the spatial dependent Rabi frequency is defined as

$$\Omega(\mathbf{r}) = \frac{1}{\hbar}\sqrt{W^2 + \Delta(\mathbf{r})^2} \tag{2.60}$$

and also the angles

$$\sin\theta = \frac{|W|}{\sqrt{W^2 + \Delta^2}}, \qquad \cos\theta = \frac{\Delta}{\sqrt{W^2 + \Delta^2}} \tag{2.61}$$

Combining the successive contributions of the propagator in Eq. (2.53) onto the initial wave function leads to the wave function at $t = t_f$ after the pulse. The ground surface wave function becomes

$$\psi_g(\mathbf{r}, t_f) = e^{-\frac{i}{\hbar}E_g t_f} e^{-\frac{i}{\hbar}\Delta t_f}[\cos(\Omega t_f) + i\cos\theta \sin(\Omega t_f)]\psi_g(\mathbf{r}, 0) \tag{2.62}$$

and the excited surface wave function becomes

$$\psi_e(\mathbf{r}, t_f) = e^{-i\phi} e^{-\frac{i}{\hbar}\Delta t_f}[\sin\theta \sin(\Omega t_f)]\psi_g(\mathbf{r}, 0) \tag{2.63}$$

where

$$\phi = \left(\omega + \frac{E_g}{\hbar}\right) t_f + \frac{\pi}{2} \tag{2.63a}$$

Equations (2.63) and (2.62) constitute extremely useful interpretive tools for analyzing impulsive pump-probe experiments.

b. The Ground Surface Dynamical "Hole" and the Excited Surface Density. We now consider the amplitude of the wave function in coordinate space. The amplitude transferred to the excited surface, $A^2(\mathbf{r}) = \sin^2\theta \sin^2(\hat{\mathbf{\Omega}} t_f)$, is missing in the ground surface creating a dynamical "hole." Once created, the "hole," which is not stationary, evolves, due to ground surface dynamics. The RISRS experiment monitors by a probe pulse this photo-induced dynamics.

In momentum space the picture is more involved. Due to cycling of amplitude between the ground and excited surfaces the wave functions gain a coor-

dinate dependent phase that induces a momentum kick

$$\Phi_g = -\frac{1}{\hbar} E_g t_f - \frac{1}{\hbar} \hat{\mathbf{\Delta}} t_f + \arctan[\cos\ \theta(\mathbf{r}) \tan(\Omega(\mathbf{r}) t_f)] \tag{2.64}$$

and

$$\Phi_e = -\phi t_f - \frac{1}{\hbar} \hat{\mathbf{\Delta}} t_f \tag{2.65}$$

On the excited surface, the wave function gains momentum linearly in time due to the coordinate-dependent phase $\Phi_e(\mathbf{r})$. Since for most photodissociation situations $\partial\hat{\mathbf{\Delta}}/\partial r$ is negative, the momentum kick $\delta\hat{\mathbf{P}} \approx \hbar\partial\Phi/\partial r$ is positive.

A more involved situation exists on the ground surface. For short times the change in momentum is zero, since the positive momentum change of the term that is linear in $\hat{\mathbf{\Delta}}$ in Eq. (2.64) is exactly compensated by the next term. This is in accordance with the Frank–Condon picture, in which the momentum of the ground surface is not affected by transfer of population to the excited surface. Far from resonance, the coordinate-dependent Rabi frequency Ω becomes very large, leading to rapid cycling. This rapidly changes the direction of the momentum shift from negative to positive, leading to the average asymptotic momentum shift of

$$\delta P = -\frac{W^2 t_f}{2\Delta^2} \frac{\partial\Delta}{\partial r} \tag{2.66}$$

This expression has also been obtained by Cina and Smith [42], using the classical Frank approximation. Detuned from resonance, this momentum shift provides the excitation interaction for impulsive stimulated Raman scattering (ISRS) [43]. On resonance ($\mathbf{r} = \mathbf{r}_h$), the cycling is slower and can lead first to a significant negative momentum shift. A semiclassical estimation of the momentum kick becomes

$$\delta\mathbf{P} \approx \hbar \left.\frac{\partial\Phi}{\partial r}\right|_{r_h} = \left[\frac{\tan(W t_f)}{W} - t_f\right] \left.\frac{\partial\Delta(r)}{\partial r}\right|_{r_h} \tag{2.67}$$

This negative momentum kick causes the "hole" to move in the positive direction of bond extension. For more intense pulses where $\Omega(\mathbf{r}_h) \cdot t_f$ exceeds π, the momentum kick changes sign and becomes positive. An interesting effect is obtained for a 2π pulse, where the "hole" in coordinate space fills

up, and a significant positive momentum change is acquired by the ground surface wave function.

A more rigorous definition of the dynamical "hole" is obtained by an orthogonal decomposition of the ground surface density $\hat{\rho}(t_f)$ into a static part and a dynamical part

$$\hat{\rho}(t_f) = \hat{\rho}_d + c^2\hat{\rho}_s \tag{2.68}$$

where $\hat{\rho}_s = Z^{-1}\exp(-\beta\hat{\mathbf{H}}_g)$ is the equilibrium stationary density operator, and the scalar product between operators is defined as $(\hat{\mathbf{A}}\cdot\hat{\mathbf{B}}) = tr\{\hat{\mathbf{A}}^{\dagger}\hat{\mathbf{B}}\}$. This definition casts the full dynamics of the density operator, including the dissipative relaxation, and leads to full thermal equilibrium. For the RISRS experiment this is usually the initial density operator $\hat{\rho}_0$. The decomposition can be done by requiring that the dynamical part $\hat{\rho}_d$ be orthogonal to the stationary density $\hat{\rho}_s$. This leads to the overlap functional

$$c^2 = tr\{\hat{\rho}(t_f)\cdot\hat{\rho}_s\}/tr\{\hat{\rho}_s^2\} \tag{2.69}$$

Since the decomposition of Eq. (2.68) is linear, all the dynamical observations depend only on $\hat{\rho}_d$ the "hole" density. It is important to notice that the dynamical "hole" is not a pure state, even when pure wave function dynamics can be applied [2].

A quantitative measure of the created coherence is an important tool in the analysis. The integrated square density of the dynamical "hole" creates a natural definition of this measure

$$C^2 \equiv tr\{\hat{\rho}_d^2\} \tag{2.70}$$

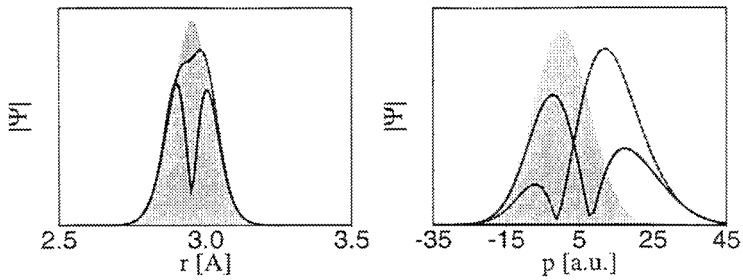

Figure 10. The ground surface wave packet immediately after a short 15-fs pulse, showing the creation of the "hole." The left panel shows the absolute value of the wave function in position space for π (solid) and 2π (dashed) pulses. The right panel shows the same wave function in momentum space. The gray background shows the wave function prior to the application of the pulse.

The coherence measure can be interpreted as the self-dynamical expectation of the dynamical "hole" $\hat{\rho}_d$.

2. *Power Absorption of a Laser Pulse*

The main observable in a pump-probe experiment is the power absorbed from the pulse. With the time-dependent Hamiltonian, Eq. (2.22), the power, or change in energy becomes [44]

$$\mathcal{P} = \frac{dE}{dt} = -2\mathrm{Re}\left(\langle\psi_e|\hat{\mu}|\psi_g\rangle \frac{d\epsilon}{dt}\right) = -2\mathrm{Re}\left(\langle\hat{\mu}\otimes\hat{\mathbf{S}}_+\rangle \frac{d\epsilon}{dt}\right) \tag{2.71}$$

where the last line is appropriate for a density operator description.

Under the conditions of the RWA, the power is linearly proportional to the change in population [44, 45]

$$\mathcal{P} = -\hbar\omega_0 \frac{dN_g}{dt} \tag{2.72}$$

The integrated power per pulse, which is the total energy absorbed, can be related to the change in population

$$\Delta E = \int_0^t \mathcal{P}\, dt' = -\hbar\omega\Delta N_g \tag{2.73}$$

a. Transient Absorption of a Weak Pulse. The power absorbed by a probe pulse can be calculated using the linear relation between the integrated power and the change in population Eq. (2.73), using the impulsive two-level coordinate dependent approximation (Section II.C.1). In most cases a weak probe

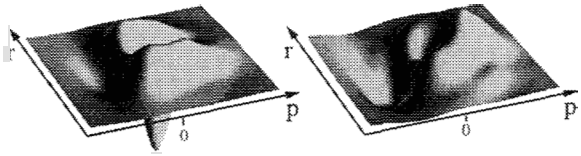

Figure 11. The dynamical "hole" $\hat{\rho}_d$ in I_3^--shown as a Wigner distribution in phase space. The left panel shows the dynamical "hole" created by a π pulse. The point of resonance is in middle of the absorption band. Qualitatively the shape of the "hole" does not change up to intensities of π. Notice that the hole is centered at $p = 0$. The right panel shows the dynamical "hole" for 2π pulse. Notice the rotation in phase space in the "hole's" shape from position to momentum.

pulse is used ($W \ll \Delta(r)$), so the population transfer at a position $\mathbf{r}$ after a time of τ_{pr} becomes

$$P(\mathbf{r}) = [\sin\ \theta \cdot \sin(\Omega(\mathbf{r})\tau_{\mathrm{pr}})]^2 \approx \left(\frac{W \sin(\Delta(\mathbf{r})\tau_{\mathrm{pr}}/\hbar)}{\Delta(\mathbf{r})}\right)^2 \tag{2.74}$$

This expression can be rearranged and written as a sinc window function $\hat{\mathbf{W}}(r, r) = P(\mathbf{r})$, which is a diagonal operator in coordinate space:

$$\hat{\mathbf{W}}(r, r) = (\hbar W \tau_{\mathrm{pr}})^2 \left(\frac{\sin(\Delta(r)\tau_{\mathrm{pr}}/\hbar)}{\Delta(r)\tau_{\mathrm{pr}}/\hbar}\right)^2 \tag{2.75}$$

To obtain the absorption signal at time t, the local population at each r should be multiplied by the transfer probability and integrated over all r, to give the total population transfer $\Delta N_g(t)$. This amounts to using the window function as the observable which measures the total power absorption of the pulse:

$$\begin{aligned}\Delta E(t) &= -\hbar\omega_{\mathrm{pr}} \Delta N_g(t) = -\hbar\omega_{\mathrm{pr}} \langle \hat{\mathbf{W}} \rangle(t) \\ &= -\hbar\omega_{\mathrm{pr}} \langle \psi(t) | \hat{\mathbf{W}} | \psi(t) \rangle = -\hbar\omega_{\mathrm{pr}} tr(\rho \cdot \hat{\mathbf{W}})\end{aligned} \tag{2.76}$$

For a short probe pulse within the impulsive limit, the observation window is influenced by electronic dephasing. A modified window operator can be calculated by simulating the absorption process starting from $\hat{\rho}_g = \hat{\mathbf{I}}$ using the full dynamics, including dissipation. Projecting out the excited surface density operator $\hat{\rho}_e$ and propagating backward in time to the instant of the peak of the pulse defines the modified window operator $\hat{\mathbf{W}}$.

b. Other Transient Spectroscopies. A different type of probe is obtained, if, after the pulse propagates through the medium, it is dispersed and its spectrum is compared to the spectrum of a reference pulse [46, 47]. In general, this problem is quite difficult, since it requires the solution of both Maxwell's and Schrödinger's equations simultaneously. The difficulty is lessened if the absorption process takes place in a thin sample and the pulse is only slightly depleted. In addition, due to fast electronic dephasing in solution, it is assumed that the dipole created by the pump pulse has decayed by the time the probe pulse has arrived. In order to relate the observation to a molecular property, the absorbed power represented by Eq. (2.73) is integrated. The total amount of energy absorbed from the field becomes

$$\Delta E_f = \int_{-\infty}^{\infty} \mathcal{P}\ dt = 2\mathrm{Re}\left(\int_{-\infty}^{\infty} \langle \hat{\mu} \otimes \hat{\mathbf{S}}_+ \rangle \cdot \frac{\partial \epsilon}{\partial t}\ dt\right) \tag{2.77}$$

Defining the Fourier transforms of the instantaneous dipole expectation

$$\langle \hat{\mu} \otimes \hat{\mathbf{S}}_+ \rangle(\omega) = \int_{-\infty}^{\infty} \langle \hat{\mu} \otimes \hat{\mathbf{S}}_+ \rangle(t) e^{i\omega t}\, dt \tag{2.78}$$

and using the Fourier transform of the field $\epsilon(\omega)$, the energy absorption can be written as [48]

$$\Delta E_f = -2\mathrm{Re}\left(\int_{-\infty}^{\infty} i\omega \langle \hat{\mu} \otimes \hat{\mathbf{S}}_+ \rangle(\omega) \cdot \epsilon^*(\omega)\, d\omega \right) \tag{2.79}$$

This suggests the decomposition of energy to frequency components

$$\Delta E_f = \int_{-\infty}^{\infty} \Delta E_f(\omega)\, d\omega \tag{2.79a}$$

Normalizing each frequency component to the energy density of the pulse leads to the expression

$$\sigma_a(\omega) = \frac{\Delta E_f(\omega)}{|\epsilon(\omega)|^2} = -2\omega \mathrm{Im}\left[\frac{\langle \hat{\mu} \otimes \hat{\mathbf{S}}_+ \rangle(\omega)}{\epsilon(\omega)} \right] \tag{2.80}$$

This expression resembles the one presented by Pollard and Mathies [46], and Yan and Mukamel [49], but its derivation is not based on a perturbation expansion, and therefore it is correct for strong fields. The main ingredient of the calculation, the instantaneous dipole $\langle \hat{\mu} \otimes \hat{\mathbf{S}}_+ \rangle(t)$, is extracted directly from the numerical integration of the Liouville von Neumann equation.

Another option for probing the transient motion is to collect the dispersed emission after the probe has propagated through the medium. The emission is a consequence of the induced dipole or polarization created by the probe pulse, which continues to radiate even after the pulse is over. The emission is proportional to the acceleration of the dipole observable $\partial^2 \langle \hat{\mu} \otimes \hat{\mathbf{S}}_x \rangle / \partial t^2$ [48]. This leads to the expression for the dispersed emission

$$\sigma_e(\omega) \propto |\omega^2 (\langle \hat{\mu} \otimes \hat{\mathbf{S}}_x \rangle(\omega))|^2 \tag{2.81}$$

Since interest is in the transient features, the static dispersed emission is subtracted from the transient one.

The same molecular quantity, the instantaneous dipole, governs all light–matter interactions. This is also true if the instantaneous dipole maintains coherence up to the time of the probe pulse [50, 51, 52, 45, 53]. The analysis of this quantity makes it possible to interpret coherent pump-probe spectroscopies. The key point is that any full numerical simulation of a pump-probe sequence automatically imposes a phase-locked pulse sequence. As a result, the instantaneous dipole induced by the first pulse can interfere with the second pulse. This is the basis of the heterodyne experiment [54, 55]. In a recent paper, Domke [56] has shown how to derive the observables of four-wave mixing using a nonperturbative approach based on the calculation of the instantaneous dipole. Due to fast electronic dephasing of the molecular I_3^- in solution, this type of spectroscopy has not been applied.

3. *Absorption Spectrum*

The initial conditions for the absorption spectrum are that all amplitude is in an eigenstate of the ground electronic surface. The main assumption is that the field is weak and that only a very small fraction is transferred to the excited surface. Under these conditions the absorption spectrum can be derived directly from the transient power expression Eq. (2.71) [57]. With these assumptions, the evolution of the wave function on the ground surface is not altered by the field

$$|\psi_g(t)\rangle = e^{-\frac{i}{\hbar}E_g t}|\psi_g(0)\rangle \tag{2.82}$$

where E_g is the ground state energy. The excited surface wave function is obtained using the time-dependent first-order perturbation theory

$$|\psi_e(t)\rangle = \frac{i}{\hbar}\int_0 d\tau e^{-\frac{i}{\hbar}\hat{\mathbf{H}}_e(t-\tau)}\hat{\mu}\epsilon^*(\tau)e^{-\frac{i}{\hbar}E_g\tau}|\psi_g(0)\rangle \tag{2.83}$$

Using the RWA-CW field $\epsilon(t) = E_0 e^{-i\omega_L t}$, Eqs. (2.82) and (2.83) are inserted into the power expression Eq. (2.71)

$$\begin{aligned}\mathcal{P} &= -2\mathrm{Re}\left(\langle\psi_g(t)|\hat{\mu}|\psi_e(t)\rangle\frac{d\epsilon}{dt}\right)\\ &= -2\omega_L\mathrm{Re}\left(\frac{E_0^2}{\hbar}\int_0^t d\tau\langle\psi_g|\hat{\mu}e^{-\frac{i}{\hbar}(\hat{\mathbf{H}}_e-E_g)(t-\tau)}\hat{\mu}|\psi_g\rangle e^{-i\omega_L(t-\tau)}\right)\end{aligned} \tag{2.84}$$

By changing the integation variable from $t-\tau$ to t, extending the integration to $t \rightarrow \infty$, and using the time reversal symmetry the well-known formula obtained by Heller [58] from the time-independent Golden-Rule expression, Eq. (2.85) is obtained the expression

$$\sigma_A(\omega_L) \propto \int_{-\infty}^{\infty} \langle \theta(0)|\theta(t)\rangle e^{i(\omega_L+\omega_i)t}\, dt \tag{2.85}$$

where $|\theta(t)\rangle = \hat{\mu}|\psi_g(t)\rangle$ is the wave function propagated on the excited surface, ω_L is the laser frequency, and $\hbar\omega_i$ is the energy of $|\psi_g\rangle$. The absorption cross section is proportional to the Fourier transform of the autocorrelation function. The steeper the excited surface is, the faster this function decays to zero, and the wider will be its Fourier transform. This correlates the slope of the excited surface at the Frank–Condon region with the bandwidth of the electronic spectrum.

Equation 2.85 can also be written as

$$\sigma_A(\omega_L) \propto \langle \psi_i|\hat{\mathbf{A}}|\psi_i\rangle \tag{2.86}$$

$$\hat{\mathbf{A}} = \hat{\mu}\left\{\int_{-\infty}^{\infty} e^{\frac{i}{\hbar}[\hbar(\omega_L+\omega_i)-\hat{\mathbf{H}}_e]t}\, dt\right\}\hat{\mu} \tag{2.87}$$

The observable $\hat{\mathbf{A}}$ is a function of the Hamiltonian of the excited surface, and is interpolated using the Newtonian interpolation method described in Appendix A.

4. *Raman Spectrum*

In a similar way, the Raman cross section for an induced transition from an initial state $|\psi_i\rangle$ to a final state $|\psi_f\rangle$ is

$$\sigma_{if}(\omega_L) \propto |\langle R_i(\omega_L)|\psi_f\rangle|^2 \tag{2.88}$$

where ω_L is the laser frequency, and $|R_i(\omega_L)\rangle$ is called the Raman wave function.

$$|R_i(\omega_L)\rangle = \left[\int_0^{\infty} e^{\frac{i}{\hbar}(\hbar(\omega_L+\omega_i)-\hat{\mathbf{H}}_e)t} e^{-\Gamma(t)}\, dt\right]|\psi_i\rangle \tag{2.89}$$

where $\Gamma(t)$ is a phenomenological lifetime. If the energies of $|\psi_i\rangle$ and $|\psi_f\rangle$ are

$\hbar\omega_i$ and $\hbar\omega_f$, respectively, the frequency of the scattered light resulting from this transition is $\omega_s = \omega_L + \omega_i - \omega_f$. The operator that creates the Raman wave function from $|\psi_i\rangle$, is a function of the Hamiltonian of the excited surface, and is interpolated using the Newtonian interpolation method described in Appendix A.

D. Method Summary

The methods described follow orthodox quantum mechanics and include three parts: the state vector, the dynamical evolution, and the observables represented by operators. The computational methods supply a phase space picture of the state, based on a discrete representation. The state is followed in time by constructing the evolution operator approximated as a polynomial. The dynamics evolution includes the radiation field as a time-dependent influence, as well as the dissipative influence of the solvent. Finally the relevant spectroscopic observables are cast into the form of observables that can be directly calculated from the state of the system.

III. APPLICATION

To gain insight into the photodissociation event of I_3^-, the calculation follows the sequence of events in time, from the initial thermal state on the ground surface to the final product I_2^- + I. Due to the heavy mass of iodine, quantum calculations are computationally intensive; therefore the computational model has to be carefully constructed. The strategy followed is to first use wave-packet simulations. These calculations serve as a guide to Liouville dynamics, which include the dissipative solvent effects. Following the methods developed in the previous section, a model of the encounter is set, involving a limited number of degrees of freedom. Within this model a fully converged quantum mechanical calculation is carried out by the following sequence:

- An initial state is prepared.
- Evolution in time is simulated.
- Experimental measurements are predicted.

The simulation is broken into four parts. In the first, the act of excitation of I_3^- by the pump pulse leading to dissociation is studied. The same pump pulse photo-induced ground surface dynamics is studied in the second part. In the third part, the system studied is the hot and coherently vibrating nascent I_2^-, interrogated by a delayed ultrafast probe pulse. In the last part, the dissipation of the excess vibrational energy from the system is investigated by a delayed push pulse, acting on the spectroscopically decayed I_2^- population. Insight into the photodissociation process can be obtained by comparing the

calculated observables with the experiment. A single set of potential energy surfaces unifies all calculations.

All the parameters used in the simulations can be found in Appendix B.

A. Electronic Potential Energy Surfaces

Common to all types of simulations are the electronic potential energy surfaces and transition dipole functions, which interpolate smoothly from reactant I_3^- to product I_2^- and to the excited I_2^- used for interrogation.

The solvent free ground surface potential of I_3^- can be calculated to reasonable accuracy by *ab initio* methods [Fig. 12(*a*)]. The colinear structure of the molecule is reconstructed and the three vibrational frequencies calculated are within 1% of the experimental values [59]. In the calculation, the potential was fit to a harmonic potential in the symmetric (111 cm^{-1}) and antisymmetric (143 cm^{-1}) stretching modes. This description is appropriate for low vibrational excitation energies, as in a thermal distribution at room temperature. If recombination events are studied, where high excitation of the ground surface vibration is anticipated, the present description should be replaced with the full *ab initio* potential.

The experimental change in these vibrational frequencies for different solvents is also within 1%. Nevertheless the antisymmetric stretch vibration is accompanied by a charge redistribution of the molecular ion. In polar solvents this charge redistribution may lead to loss of symmetry, which is represented by a double well potential.

The excited electronic energy surfaces of I_3^- are very difficult to calculate. Preliminary calculations show a multitude of excited surfaces [60], which split further due to spin–orbit interactions. As an interim solution, the upper excited potential energy was fit to a LEPS functional form using the absorp-

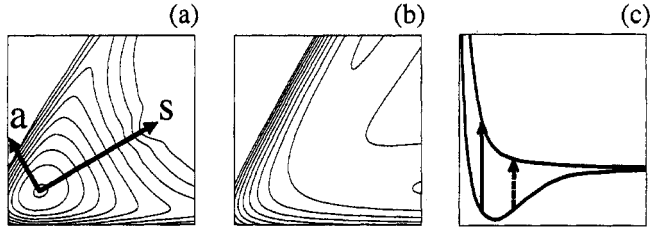

Figure 12. Approximate potential surfaces for the $I_3^- \rightarrow I_2^-$ reaction. (*a*) A contour map of the ground binding state of I_3^- (From Yamashita et al. [60]). The symmetric and antisymmetric stretching mode coordinates are shown. (*b*) The excited dissociative state of I_3^-, with two symmetrical exit channels leading to $I_2^- + I^*$ (the LEPS potential is shown). (*c*) The potential curves for the ground and excited states of I_2^-. The arrows represent the probe resonance, which is blue- (solid arrow) and red- (dashed) shifted from the center of absorption. (*a*) and (*b*) are drawn in Jacoby mass-scaled coordinates (Eq. 3.4).

tion spectra and the asymptotic I_2^- potentials, [1] [Fig. 12(*b*)]. The absorption spectrum of I_3^- shows only a small variation in different solvents, in accordance with *ab initio* calculations, which show a very small change in the charge distribution of I_3^- upon excitation.

The ground and excited surface potentials of I_2^- were taken from the gas phase experiments [61]. The potential energy surfaces have been calculated extensively and show good agreement with the experimental results [62]. The solvent can induce a charge distribution symmetry breaking of I_2^- that can modify these potentials significantly. Nevertheless, there is only a small observed solvent dependence of the absorption spectrum of I_2^-. A more elaborate treatment would include a solvation coordinate also [63, 64]. The ground and excited potential energy surfaces of I_2^- used in the present calculation are shown in Fig. 12(*c*).

B. Photodissociation of I_3^-: The "Pump" Pulse

The initial stage of the photolysis is now studied, when the electromagnetic perturbation initiates the photodissociation journey of the molecule. The impulsive nature of the excitation creates conditions at the very beginning of the trip, whose consequences are still evident much later down the road.

1. Statics

Degrees of Freedom. The model is based on the fact that I_3^- is a linear triatomic molecule. The calculation therefore concentrates on the symmetric and antisymmetric vibrational modes of the molecule, denoted r_s and r_a, respectively. As no bending mode overtones appear in the experimental resonance Raman spectrum, it is concluded that bending is not a major component at the early stages of the reaction coordinate, and the bending modes are excluded from the calculation. The rotation of the molecule is also neglected since a separation of timescales exists between the rotational and vibrational motion. These two global coordinates are transformed into atomic coordinates

$$\begin{aligned} r_{I_A-I_B} &= (r_s + 2r_a)/2 \\ r_{I_B-I_C} &= (r_s - 2r_a)/2 \end{aligned} \tag{3.1}$$

These are further transformed into mass-weighted Jacoby coordinates

$$x = r_{I_A-I_BI_C} = a \cdot r_{I_A-I_B} + b \cdot \cos\ \beta \cdot r_{I_B-I_C} \tag{3.2}$$

$$y = r_{I_B-I_C} = b \cdot \sin\ \beta \cdot r_{I_B-I_C} \tag{3.3}$$

$$a = \sqrt{2/3} \qquad b = \sqrt{2/3} \qquad \beta = \pi/3$$

This last set of coordinates is asymptotically equivalent to I_2^- vibration and relative translation of the photofragments. In these coordinates, the equations of motion for the three atoms reduce to a single equation for a pseudoparticle, with the mass of an iodine atom, moving in a two-dimensional world. In the Jacoby representation, the symmetric stretching mode is a line in the direction of 30° from the x axis, and the antisymmetric stretching mode is perpendicular to it (see Fig. 12).

Initial State. A density matrix in a two-dimensional world is a four-dimensional entity. The amount of CPU time and storage required for a four-dimensional simulation prohibit such calculations. To keep the calculation on a two-dimensional scale, the interaction with the solvent is neglected, so the dynamics do not mix pure states, and a state vector representation is adequate. This approximation is reasonable only for very short times, before the photofragments hit the walls of the solvent cage.

At room temperature, many of the excited vibrational states of the I_3^- ground electronic surface are populated. The initial density matrix in Eq. (2.16) is divided into its pure state components, which are the eigenstates of the ground surface, each multiplied by a Boltzmann weight according to its energy. The simulation starts with an initial set of these wave functions, represented on a two-dimensional grid and propagated independently. At the end of the simulation, each wave function is transformed back to a density matrix representation of a pure state, and the sum of these matrixes gives the final mixed state.

The ground electronic surface is considered to be harmonic in both vibrational modes, so the grid representation of the initial wave functions was calculated analytically. These wave functions will be denoted by their symmetric and antisymmetric excitations, respectively, i.e., $|v_{1,0}\rangle$ means a state with one quantum in the symmetric stretching mode and at ground state with respect to the antisymmetric motion. The initial states are shown in Fig. 13.

All vibrational levels up to an energy of 300 cm^{-1} were calculated. This means that at room temperature 61% of the population was accounted for in the simulation. It will be shown that this subset of the population is dominant in the experimental observations (see Tables I and II).

2. *Dynamics*

a. Electromagnetic Field. The laser pulse plays a major part in setting the dynamics in motion, by coupling the two surfaces, thus creating a population on the excited surface and leaving a population vacancy on the ground surface (to be studied in the next section). The excitation is tuned to the $I_3^- \rightarrow I_2^- + I^*$ electronic transition, slightly red-shifted from the center of absorption at 308 nm. It is taken to be circularly polarized, according to the rotating-wave approximation. In the resulting effective Hamiltonian of

Eq. (2.28) the excited state potential crosses the ground potential surface at the line of resonance, and the coupling between the shifted surfaces $\bar{\epsilon}(t)\hat{\mu}$ becomes a slowly varying Gaussian field of 60 fs FWHM (full width half maximum).

b. Propagation Results. The initial states (Fig. 13) were propagated using the time-dependent evolution operator in Eq. (2.45) with a time step of $\Delta t = 5$ fs for a total time of $t_f = 240$ fs. Under the experimental conditions, the intensity is large enough that a significant fraction of the population is transferred to the excited surface. Considering individual initial vibrational states, the fraction transferred depends primarily on the symmetric stretch excitation. This effect is summarized in Table I. The maximum quantum efficiency with a 308-nm pump is for $v = 1$ in the symmetric stretching mode. The pulse is not exactly in resonance with the maximum thermal absorption, which occurs at the peak of the $|v_{0,0}\rangle$ eigenstate [Fig. 13(*a*)], but coincides with the upper right lobe of the $|v_{1,0}\rangle$ state [Fig. 13(*b*)]. Further excitation of the symmetric stretching mode will move the main population away from the line of resonance [Fig. 13(*d*)]. The Boltzmann weights of more excited states further lowers their contribution in the final product (Table II), so the initial states used are sufficient to describe the experimental results.

The pump pulse used in the experiment was long in comparison to dynamics in the symmetric stretching mode on the excited surface. Significant coupling is present for a duration of ~180 fs [Fig. 14(*a–d*)]. This means that pho-

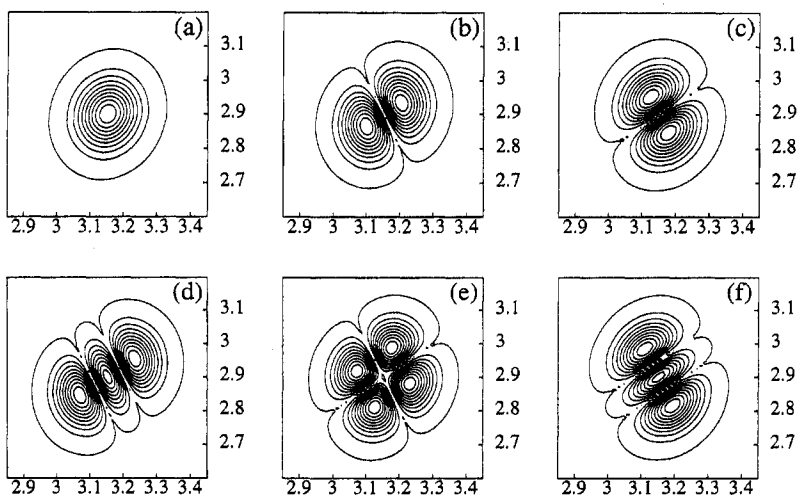

Figure 13. Contour maps of eigenstates of the ground electronic surface. (*a*)–(*f*) are $|v_{0,0}\rangle$, $|v_{1,0}\rangle$, $|v_{0,1}\rangle$, $|v_{2,0}\rangle$, $|v_{1,1}\rangle$, $|v_{0,2}\rangle$, respectively. The scaling is in angstroms.

TABLE I
The Influence of the Initial Vibrational Excitation on the Population Transferred to the Excited Surface[a]

A \ S	0	1	2	3
0	18.6%	41.6%	27.3%	5.0%
1	17.1%	40.4%		
2	15.8%			

S = excitation in the symmetric stretch mode.
A = excitation in the anti-symmetric stretch mode.

todissociation dynamics proceeds while amplitude is still fed to the excited surface. For this pulse duration, the impulsive approximation (Section II.C.1) has only qualitative meaning. Most of this motion is along the symmetric stretching mode as opposed to dynamics leading toward bond cleavage, i.e., motion along the antisymmetric stretch, which is small (see Figure 12a).

Once the pump pulse is over, the dynamics on the ground and excited surfaces decouple. Since the focus of the calculation is shifted to the products, free propagation of the wave function is carried out on the excited surface alone. The excited wave functions $|\psi_e^{s,a}\rangle(t_f)$ induced by the excitation pulse from the initial state $|\psi_g\rangle(0) = |v_{s,a}\rangle$, were used as the initial states. The propagation was carried out by the time-independent evolution operator in Eq. (2.41) generated by a time-independent Hamiltonian Eq. (2.21) with a time step of $\Delta t = 2000$ a.u. Intermediate 50-fs snapshots of the evolving wave functions were stored. Since both potentials are symmetric along the atomic coordinates [Eq. (3.2)], so are all the wave functions, throughout the propagation. This means that it is enough to follow the dynamics of just one of the product channels, leading to $I_A + (I_B I_C)^-$. To save memory and com-

TABLE II
The Boltzmann Distribution of the Initial Vibrational States[a]

A \ S	0	1	2	3
0	20.5%	12.0%	7.1%	4.1%
1	10.3%	6.0%	3.5%	2.1%
2	5.2%	3.0%	1.8%	1.0%
3	2.6%	1.5%	0.9%	0.5%

S = excitation in the symmetric stretch mode.
A = excitation in the anti-symmetric stretch mode.

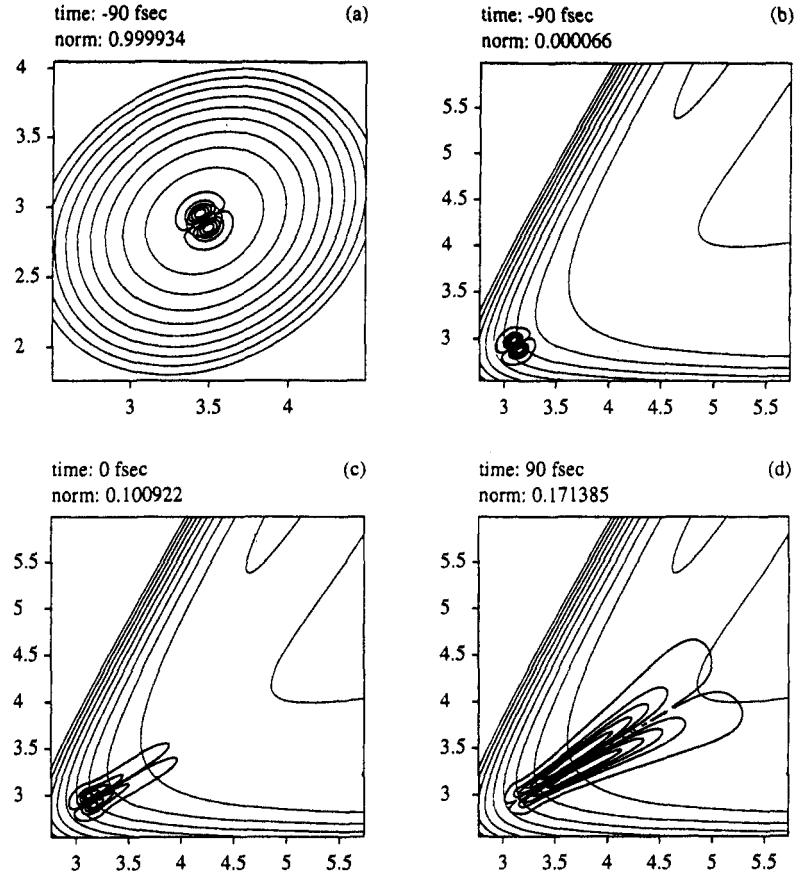

Figure 14. Propagation of the wave packet during a 60-fs pump pulse. The initial state shown is $|v_{0,1}\rangle$. (*a*) The wave function on the ground state at the very beginning of the pulse. (*b*) The excited surface wavefunction. (*c*) The wave function at the peak of the pulse. (*d*) The wave function after most of the pulse is over. The scaling is in angstroms.

putation time, and this exit channel is fully described by the grid. The other channel is blocked by an absorbing boundary condition[5] [65], which makes it possible to take the grid twice as far in the x direction as in the y direction. Figures 15 and 16 show several snapshots starting from two different initial wave functions.

[5]Absorbing boundary condition is a pseudopotential $\hat{\mathbf{V}}_{absorbing}$ added to the Hamiltonian. This potential is zero on most of the grid, and negative imaginary on the boundary. Any part of a wavefunction propagating under the influence of this anti-Hermitian potential will decay exponentially to zero before it can overflow the grid boundary.

At the early stage of the dynamics the motion is along the direction of the symmetric stretch, down the potential slope, across the saddle point, and "up hill" in the direction of the three-body dissociation. Only when the wave function crosses the saddle point, does motion in the direction of the antisymmetric stretching become significant. This motion, is an essential component of the reaction coordinate leading to bond cleavage.

The wave function that was initiated as an antisymmetric eigenstate on the ground surface is "better suited" for such motion, and enters the second stage earlier, falling rapidly into the exit channels without ascending deep into three-body dissociation [Fig. 16(*a*)]. On the other hand, the wave function that started as a symmetric eigenstate has most of its population centered along the symmetric stretching mode, so it continues ascending much further before bifurcating into the exit channels (Fig. 15(*a*)].

The wave function enters the exit channels with much excess energy, which translates into two asymptotic modes: vibration of the I_2^- fragment, and translation of the I atom away from the I_2^- molecule. Coherent vibrational motion of the antisymmetric wave function is seen clearly in Fig. 16(*b*), and less evidently in Fig. 15(*b*).

After longer propagation, the wave function is no longer compact because of the large distribution in translational energy, which smears the wave packet into a long "snake" Figs. 15(*c*) and 16(*c*). The total excess energy is relatively well defined by the photon energy dispersion in the pump (0.04 eV). This imposes an obvious correlation between vibrational and translational degrees of freedom in the evolving product. The long serpentine appearance of the wave packet initially in $|v_{1,0}\rangle$ indicates an extremely large dispersion of the wave packet, whose initial dynamics is primarily along the symmetric stretch. The shape of the wave packet at long delays also indicates that the portion entering earlier into the exit channel is characteristic of high translational and low vibrational energy content; whereas the more delayed portions are poor in translation and highly excited vibrationally. This dispersion is much less apparent in the case of I_3^- initially excited in the antisymmetric stretching mode. This initial displacement of density away from the ridge of perfect symmetry tends to direct the population into the exit channels in a much more compact and uniform fashion, limiting the degree of dispersion in vibration and translation. One should keep in mind that, in a solvent, the translational motion will be rapidly dissipated due to hitting with the solvent molecules.

3. *Interpretation*

It is evident that the shape of the wave packet at very long times still bears a memory of its early history, at times shorter than a few hundred femtoseconds, in which the dynamics are governed by the electromagnetic pulse

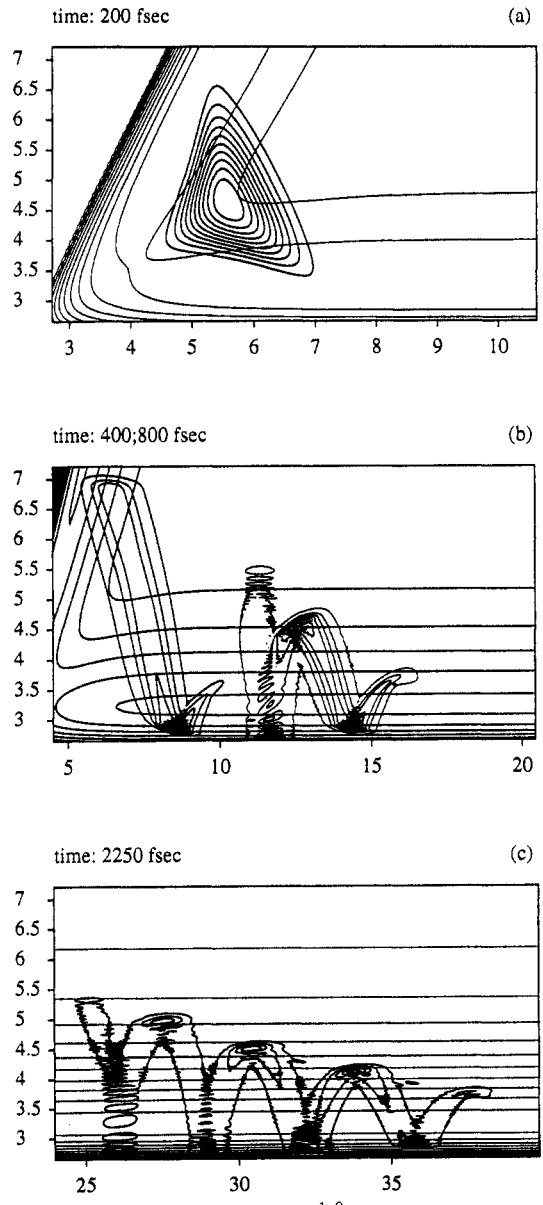

Figure 15. Propagation of the wave packet $|\psi_e^{1,0}\rangle(t)$ generated by the pump pulse, on the excited surface. The initial state $|\psi_g\rangle(0)$ is $|v_{1,0}\rangle$. The first wave function in (*b*) is "chopped" at the top of the frame by an absorbing potential. The scaling is in angstroms.

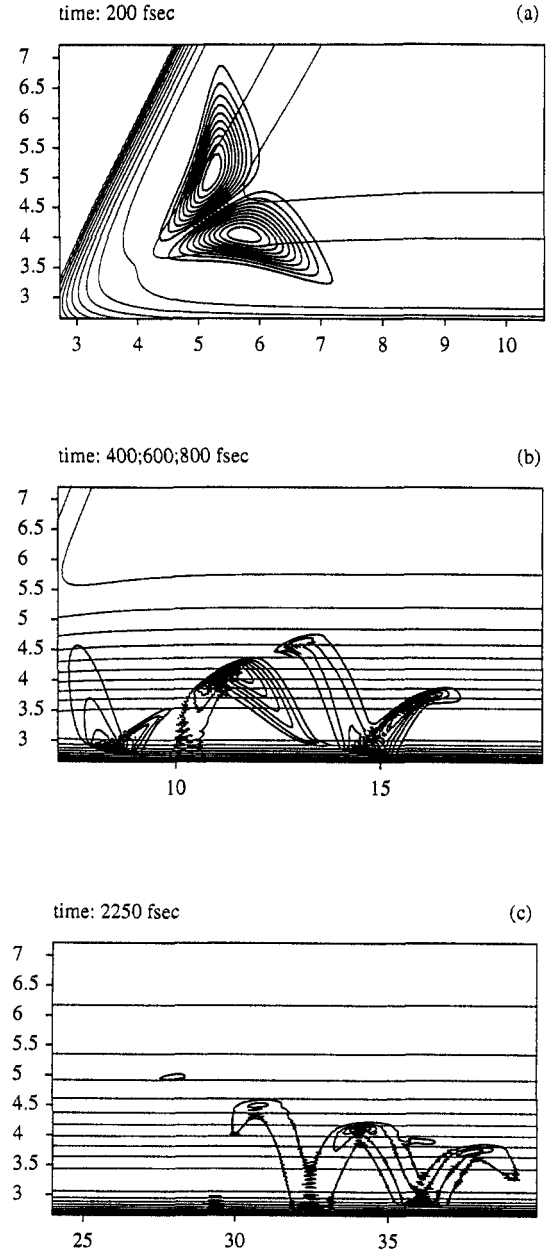

Figure 16. Propagation of the wave packet $|\psi_e^{0,1}\rangle(t)$ generated by the pump pulse, on the excited surface. The initial state $|\psi_g\rangle(0)$ is $|v_{0,1}\rangle$. The scaling is in angstroms.

and the Franck–Condon region of the excited potential. There are two other observables that correlate with the same part of the potential: the electronic absorption spectrum and the Raman spectrum.

a. Absorption Spectrum. The slopes of the excited potential surface in the Frank–Condon region have a major influence on the width of the electronic absorption spectrum. Calculation of the absorption spectrum, using Eq. (2.87), then gives the calculated measure for this slope. Fitting the calculated spectra with the experimental one has served to calibrate the parameters of the LEPS potential.

b. Raman Spectrum. A complementary probe of the first stages of the dissociation dynamics is recovered from the Raman spectra. Raman wave functions were calculated for all initial vibrational states using Eq. (2.89), integrating to a time of 75 fs. The excitation energy E_L is on resonance with the transition.

The Raman wave function shown in Fig. 17 is very similar to the wave packet created by the pump pulse [Fig. 14(*c*)]. Thus the Raman spectra and the RISRS experiment carry complimentary information on the initial stage of the photodissociation. Individual Raman spectra were extracted from the Raman wave functions using Eq. (2.88), and then Boltzmann averaged according to the initial vibrational energies. Figure 18 shows the resulting Raman spectrum at $T = 300$ K.

The main features in the spectrum correspond to harmonics of the symmetric stretching frequency, and so are attributed to the population of highly excited states of the symmetric stretching mode by the Raman process. In the time domain, this correlates to the long propagation along this mode.

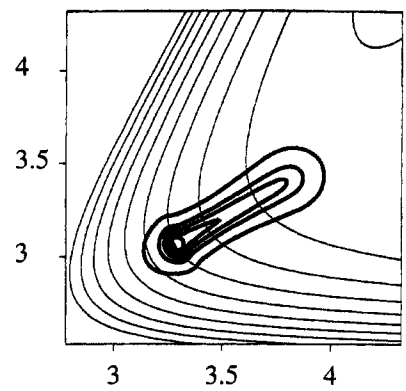

Figure 17. The Raman wavefunction excited from $|v_{1,0}\rangle$ on the LEPS potential. The scaling is in angstroms.

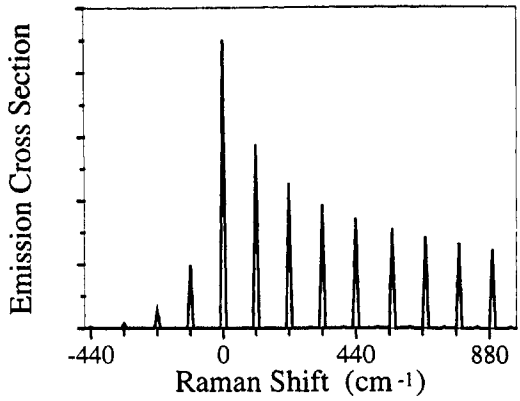

Figure 18. The simulated Raman spectrum at T = 300 K of I_3^- calculated with the LEPS potential.

The odd harmonics of the antisymmetric stretching frequency are symmetry forbidden, so only the second harmonic is expected in the spectrum, as the propagation along the antisymmetric mode is very small. On examining the spectrum, it can be seen that the second harmonic of the antisymmetric stretch has, indeed, only a very small signature.

The Raman spectrum is sensitive to the shape of the excited potential, as can be seen by comparing the above results with preliminary work on the *ab initio* potential. This potential induces spreading along the antisymmetric stretching mode as well (Fig. 19). The resulting spectrum (Fig. 20) differs in

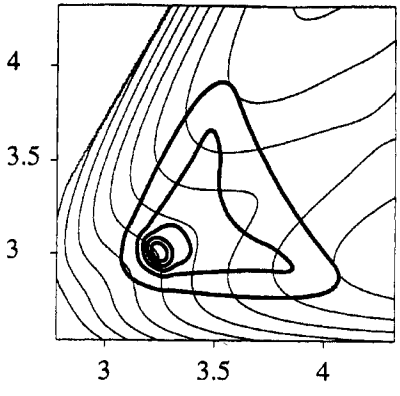

Figure 19. The Raman wave function excited from $|v_{1,0}\rangle$ on the *ab initio* potential. The scaling is in angstroms.

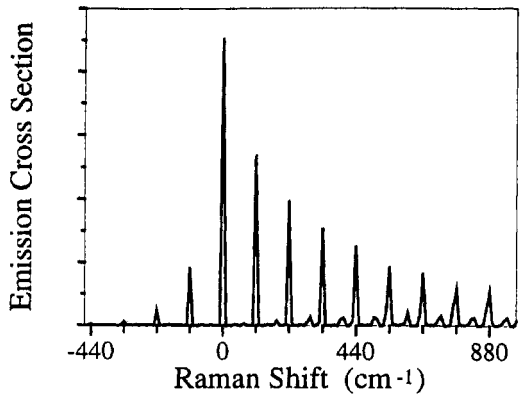

Figure 20. The simulated Raman spectrum at T = 300 K of I_3^- calculated with the *ab initio* potential.

two ways from the previous one. First, the decay of the signal corresponding to the higher harmonics of the symmetric stretch is more rapid. Second, the second harmonic of the antisymmetric stretch has a more pronounced signature, which increases for higher Raman shifts (corresponding to longer propagation times on the excited surface). This is consistent with the shape of the Raman wave function, in which the motion along the antisymmetric stretch mode is larger at later times.

C. Dynamics of the Photo-Induced "Hole" in I_3^-

The photoinduced density on the excited surface leading to photodissociation is missing on the ground surface. The missing density or the coherent "hole" is nonstationary and will therefore continue to ring long after the pump pulse has turned off. Observation of this ringing sheds light on the interaction of the reactant I_3^- with its solvent.

1. Statics

a. Degrees of Freedom. The initial position of the dynamical "hole" is determined by the ground–excited difference potential $2\hat{\mathbf{\Delta}} = \hat{\mathbf{V}}_e(\mathbf{r}) - \hat{\mathbf{V}}_g(\mathbf{r}) - \hbar\omega_L$ in Eq. (2.50). The gradient of the difference potential along the antisymmetric stretch is almost zero; therefore this mode can be excluded from the calculations. The simulation of the excitation stage in Section III.B.2 has verified this assumption. For this reason a one-dimensional representation in the symmetric stretching coordinate is an adequate description.

These consideration should be reevaluated for a shorter pump pulse and the sharper *ab initio* potential of Fig. 20 is used. In this case the difference potential $\hat{\mathbf{\Delta}}$ will include a contribution from the antisymmetric stretching mode. The induced "hole" in this direction will have inversion symmetry, in

accordance with the Raman spectrum; therefore the fundamental frequency will not be excited. A modulation with a period of the first overtone ≈ 100 fs will be a signature of this motion.

b. Initial State. The dynamical "hole" density is recreated by solving the Liouville dynamics for the symmetric stretching mode. The initial state was a thermal density on the ground surface at 300 K. The pump field amplitude used in the simulation corresponds to 1.1π pulse conditions on resonance for the 60-fs pulse. The total depletion of the ground surface population in these conditions is 8%. Electronic dephasing has a profound influence on the amount of coherence generated on the ground surface and, as a result, on the depth of the observed modulations. This dephasing process can be thought off as limiting the time during which the two surfaces are coupled by the radiation. In accordance with Section II, Eq. (2.35), a Gaussian dissipative model is used, leading to

$$\hat{\mathcal{L}}_D(\hat{\rho}) = -\tfrac{1}{2}\gamma_z[\hat{\mathbf{I}} \otimes \hat{\mathbf{S}}_\mathbf{z}, [\hat{\mathbf{I}} \otimes \hat{\mathbf{S}}_\mathbf{z}, \hat{\rho}]] \tag{3.4}$$

The electronic coherence lifetime γ_z^{-1} is estimated to be in the range of 10–100 fs. Finally a Gaussian vibrational dephasing process was also added

$$\hat{\mathcal{L}}_D(\hat{\rho}) = -\tfrac{1}{2}\gamma_g[\hat{\mathbf{H}}_\mathbf{g} \otimes \hat{\mathbf{I}}, [\hat{\mathbf{H}}_\mathbf{g} \otimes \hat{\mathbf{I}}, \hat{\rho}]] \tag{3.5}$$

The dephasing characteristic time was set at $\tau_{dg} = (\omega_g^2\gamma_g)^{-1} = 960$ fs. With this timescale the vibrational dephasing has only a small effect on the creation of the dynamical "hole." Fig. 21(*a*) displays the dynamical "hole" immediately after the pump pulse. Under these conditions the resulting dynamical "hole" is mainly a shift of density along the position coordinate, with relatively weak contribution of direct shift along the momentum direction.

2. *Dynamics*

The dynamics of the "hole" $\hat{\rho}_d$ are studied directly by propagating $\hat{\rho}_g$ obtained above after the excitation pulse has turned off. The evolution operator is generated by the ground surface Hamiltonian and the vibrational dephasing term in Eq. (3.5). Figure 21 shows phase space snapshots of the dynamical "hole" at different time delays after the pump pulse. Note that the phase space distribution consists of balanced positive and negative parts, since the integrated phase space volume of the "hole" is zero ($\hat{\rho}_d^e$ is traceless). The dynamics is influenced by the ground surface Hamiltonian and the vibrational dissipation. The ground surface Hamiltonian rotates the distribution in phase space—a full cycle corresponds to one vibrational period

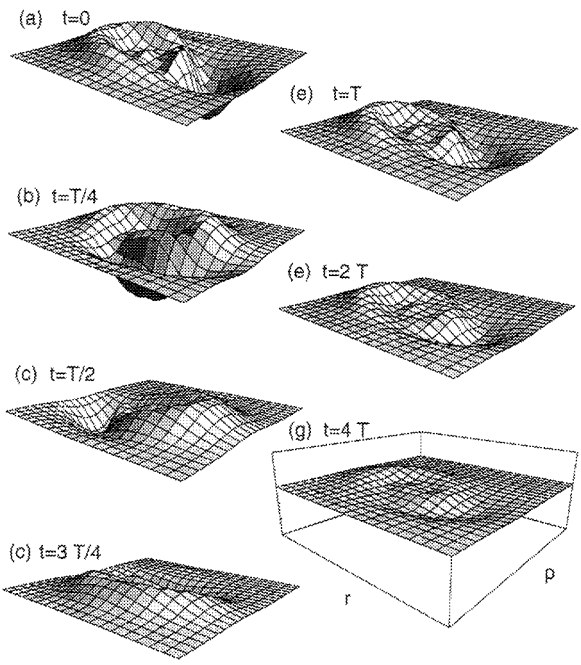

Figure 21. Snapshots of the Wigner distribution function $W_d(r,p)$ of the dynamical "hole." The initial density is a Boltzmann distribution at 300 K, pumped by a pulse of 60 fs FWHM and wavelength of 308 nm. T is the period of the vibration.

[Fig. 21(*a–e*)]. Since the "hole" in this case is created in an initial thermal distribution at the bottom of the I_3^- potential there is no anharmonic contribution to the dynamics. Therefore only the dissipative terms eliminate the "hole" by smoothing it out. In the present case, the major effect of dissipation is assumed to be vibrational dephasing, which manifests itself in smearing the lobe and anti-lobe of the dynamical "hole" while they undergo circular motion in phase space. Energy relaxation processes are assumed not to contribute in view of the longer timescale of vibrational relaxation found for the I_2^- in Section III.E.

In a pump-probe experiment, many experimental measurements are taken at different delays between the pulses. The idea is that the strong pump pulse prepares the molecules in a nonstationary state, and the weak probe pulse serves as a tool for measuring the evolved state at a certain point in time.

After the measurement takes place, these molecules are regarded as gone (they either dissociate to give a different molecule, or recombine and cool back to their initial state). The next pulse pair encounters the same initial conditions as the last, prepares the molecules at the same nonstationary state, and measures the evolved state at a different point in time. Only the power absorbed by the probe is calculated; thus, the state of the system on the excited surface after its interaction with the probe pulse has no experimental significance, and is therefore eliminated.

3. *Interpretation*

A full simulation of the probe signal in a pump-probe absorption experiment is shown in Fig. 22. The modulations are fit to an exponentially decaying $\sin(t)$ function. The decay time, 960 fs, agrees with the decay time of the coherence measure. It is important to stress that the ability to directly measure the rate of vibrational dephasing from the decay of oscillations in optical density is not at all trivial.

Figure 23 compares the results of the full simulation of the pump-probe experiment (Fig. 22) with the experimental results in ethanol. The expo-

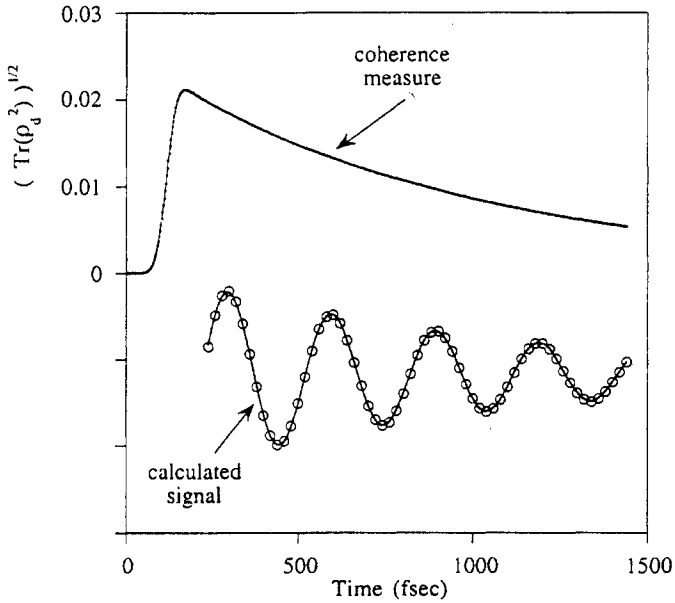

Figure 22. The coherence measure as a function of time (upper panel) for a full simulation of the pump-probe experiment. An electronic dephasing time of 5 fs and vibrational dephasing time of 960 fs have been used. The calculated signal is shown in the bottom panel. The solid line is a fit to an exponentially decaying sin function of ω_v = 112 cm^{-1} and decay time τ_{dg} = 960 fs.

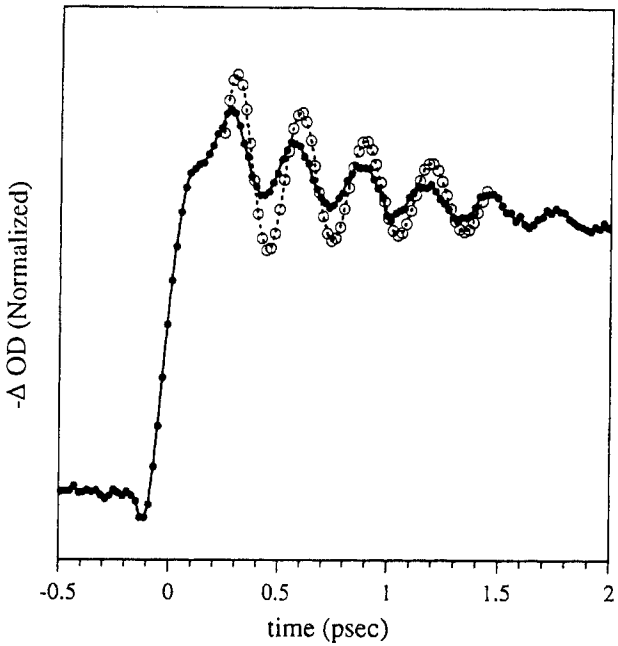

Figure 23. Comparison of the experimental results in ethanol (solid points) with the simulation of the pump-probe experiment (open circles). The baseline is identical for both signals. The slow background exponential decay, obtained from the fit to the experimental data, was added also to the simulated result. The frequency, phase, and decay time of the simulated signal agrees with the experimental data.

nentially decaying sine function affords a good fit to both the measured and calculated signals, allowing the extraction of various molecular and solvent-dependent parameters. The frequency of the experimental and simulated spectral modulation matches the ground state symmetric stretching frequency. The absolute phase of the spectral modulations reflects the position in phase space of the coherent "hole" and is identical, within experimental error, to the simulations. Finally the decay rate of the spectral modulation allows the extraction of a dephasing constant, assumed in the simulation to be due to purely vibrational dephasing. Identifying the decay rate with changes of the coherence measure in the molecular system has been verified in Fig. 22.

The major discrepancy between the calculated and experimental signal is the depth of modulation. This might be due to propagation effects of the radiation through a dense medium; these are not considered in the simulation.

The RISRS experiment is able to measure the ground surface vibrational frequency of the solvated system and the vibrational dephasing rate. With a shorter pump and probe higher harmonics can be observed.

D. Dynamics of Nascent I_2^-: The "Probe" Pulse

The role of the probe laser pulse in this section is that of a silent observer, quietly recording the details of the trip of hot I_2^- to equilibrium.

1. *Statics*

a. Degrees of Freedom. The system at hand is the nascent I_2^- molecule. The model for I_2^- is one-dimensional, including the single vibrational mode of the diatomic molecule $(I_BI_C)^-$. This mode can be represented in coordinate space by the y Jacoby coordinate in Eq. (3.4), or expanded in eigenstate space $\{|v_i\rangle\}$, where $\hat{\mathbf{H}}_g|v_i\rangle = E_i|v_i\rangle$. The relative translation of the photofragments (the x Jacoby coordinate), will be shortly discarded as it bears no effect on the experimental observables. As for I_3^-, the rotations are once again neglected due to the divergence of timescales.

Since the system has just one dimension, it can be represented as a density matrix, and the influence of the solvent can be added to the dynamics through the open system formalism developed at the previous section.

b. Initial State. The final states of Section III.B.2 serve as the starting point for the current calculations. Each final state $\psi_e^{s,a}(x,y)$ is first transformed to momentum representation along the x coordinate by an FFT as in Eq. (2.4), and then to the I_2^- vibrational eigenstate representation along the y coordinate, using a unitary basis transformation from $\{|y\rangle\}$ to $\{|v_i\rangle\}$ as in Eq. (2.1), resulting in $\psi_e^{s,a}(p,v)$. A density matrix was constructed from each of these wave functions

$$\rho_g^{s,a}(p,p',v,v') = |\psi_e^{s,a}(p,v)\rangle\langle\psi_e^{s,a}(p,v)| \tag{3.6}$$

A partial trace over the momentum degree of freedom (p) was taken, resulting in the desired one-dimensional representation in v space $\rho_g^{s,a}(v,v')$. The effect of this reduction on the measured observables was checked by comparing the transient absorption of $\psi_e^{s,a}(x,y)$ and $\rho_g^{s,a}(v,v')$, and the difference was found to be negligible. This can be attributed to the strong correlation between v and p, as seen in Fig. 16(c) and Fig. 15(c), meaning that each v collects contributions from a very narrow band of p's in the partial trace process, and has no coherence with p's outside this band.

The initial state for the I_2^- relaxation study was created by Boltzmann averaging over all initial wave functions:

$$\rho_g(v,v') = \sum_{s,a} e^{-E_v^{s,a}/k_BT}\rho_g^{s,a}(v,v') \tag{3.7}$$

where $E_v^{s,a}$ is the energy of the eigenstate $|v_{s,a}\rangle$ of the ground surface of I_3^-.

The time instant chosen for the reduction was set at t = 680 fs in which the dissociation process already separated the wave function into the asymptotic channels. In order to compensate for the dissipation at earlier times the initial density was propagated backwards in time under dissipation-free evolution to a time of t = 255 fs. This time is estimated as the time at which the molecular ion I_2^- has separated from the I atom and can be considered as a separate motion influenced by the solvent. The state $\rho_g(v, v')$ at t = 255 fs was then used as the initial state for the dissipation studies. Figure 24 shows the Wigner plots of the initial distribution. The left panel shows the Wigner function $W_g(r, p)$ and its projections on the coordinate and momentum coordinates. On examining the figure it is clear that a very broad initial distribution is created. The right panel shows the initial Wigner function $W_g(v, \phi_v)$, which reveals that the I_2^- photoproduct is created in a vibrationally hot state, with a mean energy of 0.55 eV. The projection on the vibrational state displays a very wide vibrational distribution peaked at 0.4 eV (v = 34). The dissipation of this energy by the solvent will be the main subject of the next section.

2. *Dynamics*

The probe pulse is not to be incorporated into the Hamiltonian, and only its experimental outcome, the total power absorbed, is calculated in Section III.D.3.

a. Potential and Interaction with the Solvent. The ground and excited potential curve of I_2^- has been described in Section III.A. The excited surface does not take part in the dynamics, as there is no coupling between the

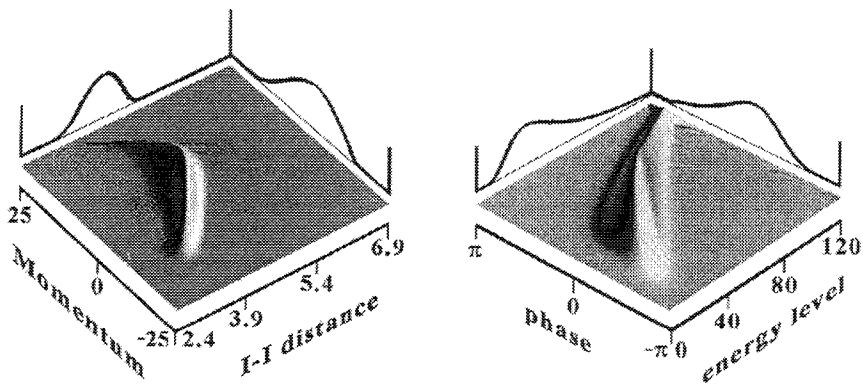

Figure 24. The Wigner distribution function $W_g(r, p)$ and $W_g(v, \phi_v)$ of the initial density at time t = 255 fs. The projections on the variables are also shown, displaying the initial position, momentum, vibrational energy, and phase distributions. Distances are in angstroms, and the momentum units are Å/ps.

surfaces (the electromagnetic field of the probe is excluded from the Hamiltonian), so only $\hat{\rho}_g$ will be considered in the dynamics.

During its nuclear motion the nascent I_2^- molecule is constantly influenced by the bath. This influence can be caused by direct impact on the nuclei due to collisions with the bath molecules, or by solvent dipoles interacting with the electrons of the molecule. The solvent's influence can be divided into a static part, described by a modification of the effective potential, and a dynamical part, which, viewed by the reduced molecular system, has a stochastic nature, so each I_2^- molecule "feels" random collisions and dipole fluctuations. To describe these processes, the phenomenological framework of Section II.B.2 is used. The dissipation process are divided in two categories:

- Relaxation: Processes that allow energy flow between the system and the bath. They will be referred to as T_1 processes.
- Dephasing: Elastic processes that conserve the energy of the system, but erase the coherence between the different populations in $\hat{\rho}_g$. These will be termed T_2 processes.

The dissipative part of the Liouvillian is likewise divided into two categories

$$\hat{\mathcal{L}}_D = \hat{\mathcal{L}}_{D_{nr}} + \hat{\mathcal{L}}_{D_{nd}} \tag{3.8}$$

where $\hat{\mathcal{L}}_{D_{nr}}$ is the nuclear energy relaxation term and $\hat{\mathcal{L}}_{D_{nd}}$ is the nuclear dephasing term.

In general the dissipative energy exchange process is described by

$$\hat{\mathcal{L}}_{D_{nr}}(\hat{\rho}_{\mathbf{g}}) = \sum_{ij} \gamma_{ij} \left[\hat{\mathbf{P}}_{ij} \hat{\rho}_{\mathbf{g}} \hat{\mathbf{P}}_{ij}^{\dagger} - \frac{1}{2} \{ \hat{\mathbf{P}}_{ij} \hat{\mathbf{P}}_{ij}^{\dagger}, \hat{\rho}_{\mathbf{g}} \}_+ \right] \tag{3.9}$$

where $\hat{\mathbf{P}}_{ij}$ is a projection from state $\langle v_i|$ to state $|v_j\rangle$, $\hat{\mathbf{P}}_{ij} = |v_j\rangle\langle v_i|$, and γ_{ij} is a rate constant. Detailed balance is imposed when the rate constants obey the relation $\gamma_{ij}/\gamma_{ji} = e^{-(E_j - E_i)/k_B T}$. In this study the source of the energy relaxation is the cage effect of solvent molecules pushing against the I_2^- ion. It is therefore reasonable to assume that the relaxation rate is proportional to the vibrational amplitude. A linear relation of the rate γ_{ij} with vibrational amplitude was therefore assumed. Since the oscillator is anharmonic, the rate was chosen to be proportional to the classical vibrational amplitude of the energy of level i. Specifically, only nearest-neighbor transitions were included in the calculation. Finally, the rate coefficients were all proportional to a global parameter Γ that empirically determines the relaxation rate τ_{nr}. For low excitation energies the relaxation model matches the energy relaxation rate of a

harmonic oscillator. The energy relaxation parameters were adjusted to the harmonic model used previously with τ_{nr} = 3ps [2].

Random elastic collisions of the solvent with the molecule, which are fast on the vibrational time scale, are described by a Gaussian random process. This process leads to a dephasing of the vibrational motion. By choosing $\hat{\mathbf{V}}_i = \hat{\mathbf{H}}_g$ in Eq. (2.34) the nuclear dephasing term is obtained

$$\hat{\mathcal{L}}_{D_{nd}}(\hat{\rho}_{\mathbf{g}}) = -\gamma_{nd}[\hat{\mathbf{H}}_g, [\hat{\mathbf{H}}_g, \hat{\rho}]] \tag{3.10}$$

$$\tau_{nd}(v) = 1/(\omega(v)^2\gamma_{nd}) \tag{3.11}$$

where $\tau_{nd}(v)$ is the dephasing time constant of the vibrational level v, and $\omega(v)$ is the vibrational frequency of that level. The value of $\tau_{nd}(0)$ was taken to be 960 fs. In the Heisenberg picture $\hat{\mathbf{H}}_g$ is a constant of motion ($\hat{\mathcal{L}}^{\dagger}_{D_{nd}}(\hat{\mathbf{H}}_g) = 0$), so this term represents a process where the system on the ground surface does not exchange energy with the bath. A similar dephasing term was used to describe the dissipative dynamics of the "hole" in the reactant I_3^-.

Since the nuclear relaxation term is easily constructed in terms of the ground surface eigenstates, the eigenstate representation was used for the Hamiltonian as well, which is diagonal in its own basis representation

$$\mathbf{H}_g(v', v) = \delta_{v',v}E_v \tag{3.12}$$

b. Propagation Results. To obtain insight concerning the different mechanisms of dissipation, different types of dynamics were studied and compared. As a benchmark, the dissipation-free Hamiltonian dynamics were simulated. The free dynamics were contrasted with dissipative evolution that includes energy relaxation processes [T_1, Eq. (3.9)]. Finally dephasing processes were also included [$T_1 + T_2$, Eq. (3.10)].

Figure 25 compares snapshots of the Wigner function $W_g(r,p)$ of the different dynamical processes. The free evolution is described in the left panel. The motion observed is a winding motion, since the outer energy shells have a lower vibrational frequency due to anharmonicity. As a result the free dynamics stretches the initial distribution around the zero energy point $(r - r_{eq})$, $p = 0$. The anharmonic effect is more readily understood by examining Fig. 26, which displays the Wigner function in action angle variables. The phase velocity of the higher quantum numbers (higher action) is slower than the lower ones, because of the anharmonicity of the I_2^- potential. As a result the dynamics can be visualized as a winding motion of the distribution around a cylinder whose axis represents the action. The observable consequence of the anharmonic motion is scrambling of the phase compactness. This leads to a reduction of the amplitude of the spectral modulations of the probe pulse.

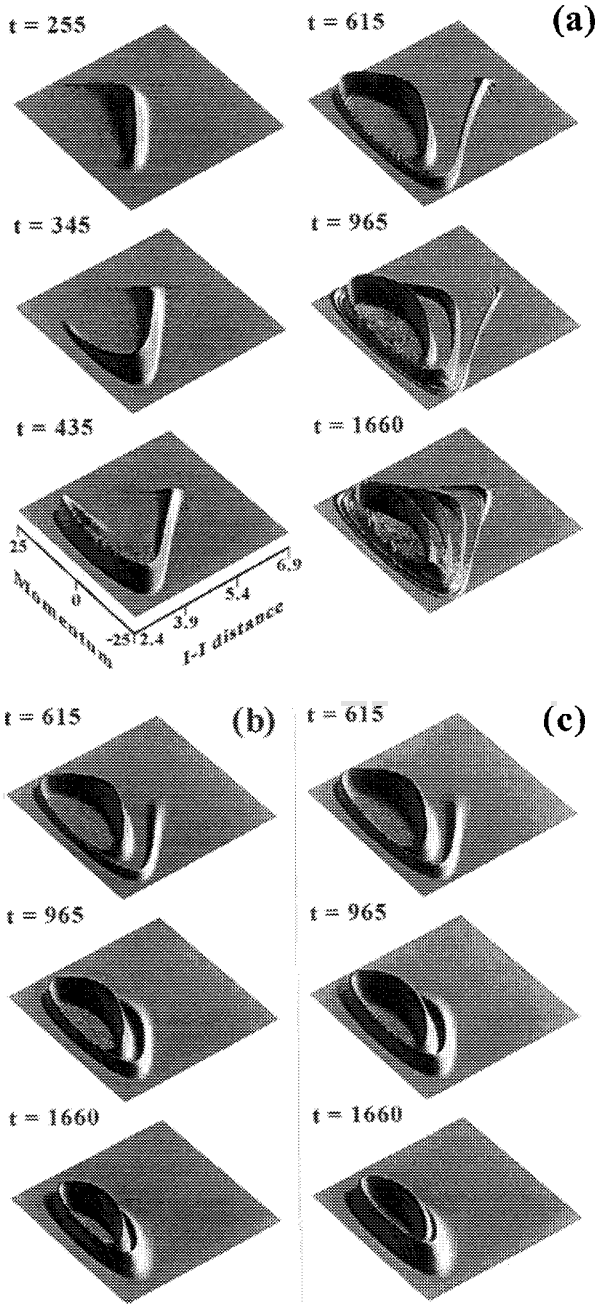

Figure 25. Snapshots of the Wigner distribution function $W_g(r,p)$: (*a*) Hamiltonian dynamics only; (*b*) Dynamics with energy relaxation (T_1); (*c*) Dynamics with energy relaxation and dephasing ($T_1 + T_2$). Times are in femtoseconds where the panels correspond to approximately 0, $\frac{1}{4}$, $\frac{1}{2}$, 1, 2, 4 vibrational periods. Distances are in angstroms, and the momentum units are Å/ps.

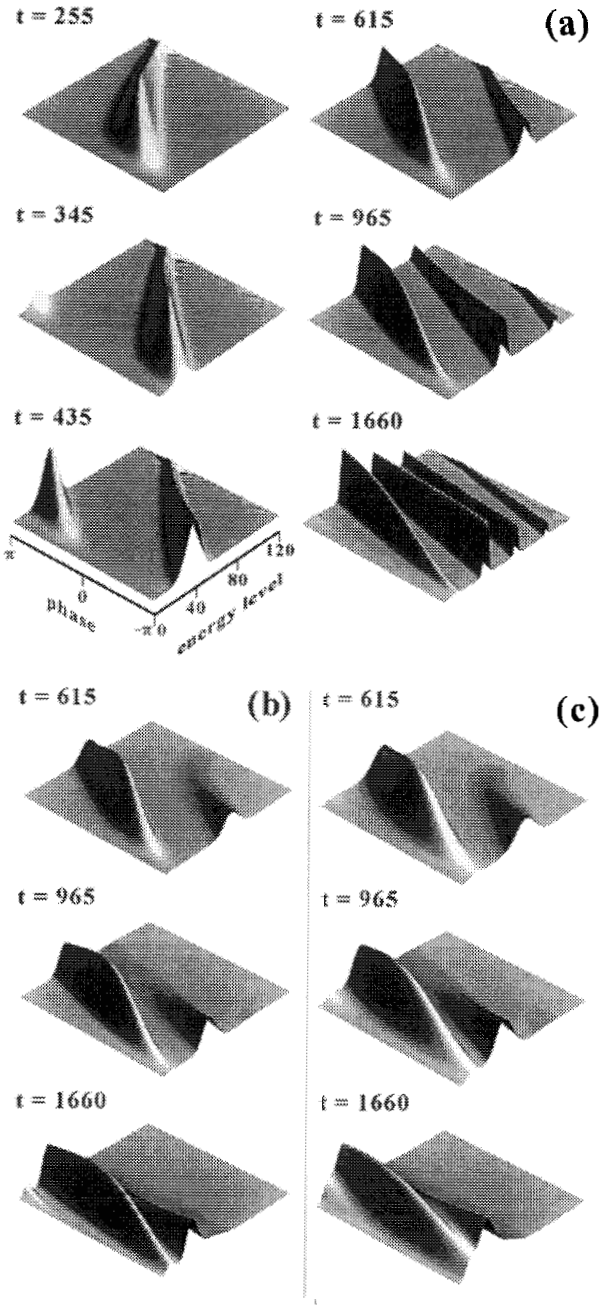

Figure 26. Snapshots of the Wigner distribution function in action angle coordinates, $W_g(v, \phi_v)$: (*a*) Hamiltonian dynamics only; (*b*) Dynamics with energy relaxation (T_1); (*c*) Dynamics with energy relaxation and dephasing ($T_1 + T_2$).

The energy relaxation process is described in Figs. 25(*b*) and 26(*b*). In the (r,p) phase space, energy relaxation is manifested by the distribution $W_g(r,p)$ approaching the origin. In the action angle representation, the relaxation moves the distribution $W_g(v,\phi_v)$ towards lower action values, thus decreasing the loss of phase due to anharmonicity. The effect of removing energy is enhancement of the modulation in phase, as can be seen by comparing panels (*a*) and (*b*) of Fig. 26 at t = 1660 fs.

Finally the right panel (*c*) in Figs. 25 and 26 shows the added influence of dephasing on the dynamics. As can be seen in Fig. 26 the features along the phase coordinate at a time of t = 1660 fs are smoother in panel (*c*), so that the observed modulation would be smaller.

3. *Interpretation*

The different types of dynamics have a profound effect on the transient observables, specifically on the measured transient spectrum of a weak probe pulse. Two different wavelengths were used, one blue-(at 620 nm) and one red-(at 880 nm) shifted from the center of the absorption band (at 740 nm), which induces a transition to a dissociative state of I_2^-. To obtain the absorption signal of the probe pulse, the impulsive limit in weak fields is employed [Eq. (2.76)], where τ_{pr} = 60 fs. A phase space image of the window functions associated with the two probe pulses is shown in Fig. 27.

The window function is momentum independent, but it is almost δ correlated in the r coordinate (actually, it is sinc correlated), with a sharp peak at the resonance point (3.1 Å for 620 nm and 3.4 Å for 880 nm). These points are equal to the classical inner (620 nm) and outer (880 nm) turning points of v = 2. This correlation is reflected in the phase coordinate at low v values, where the window is centered around $\pm\pi$ for 620 nm and around 0 for 880 nm, which are the phases of the inner and outer turning points, respectively. For $v > 2$ the lines at r = 3.1 Å and at r = 3.4 Å cross the iso-energy lines at two points each (compare Fig. 27 and Fig. 8), corresponding to inward and outward motion at the resonance point, which explains the bifurcation of the phase dependency for larger energy values. Because of the oscillatory shape of the eigenstates, the window in the v representation is a wide oscillatory function, with a large peak at v = 3, but on the average the window is more sensitive to the lower vibrational states.

a. Transient Spectrum of Individual States. The effect of the initial vibrational state on the resulting spectral modulations was studied first. The transient absorption for the different $\rho_g^{s,a}(v,v')$ was calculated with a dissipation-free Hamiltonian. Examining Fig. 28 it is clear that the modulations of the probe signal increase upon excitation of the antisymmetric stretching mode. The phase of the signal is also shifted to earlier times because the wave packet enters the exit channel earlier.

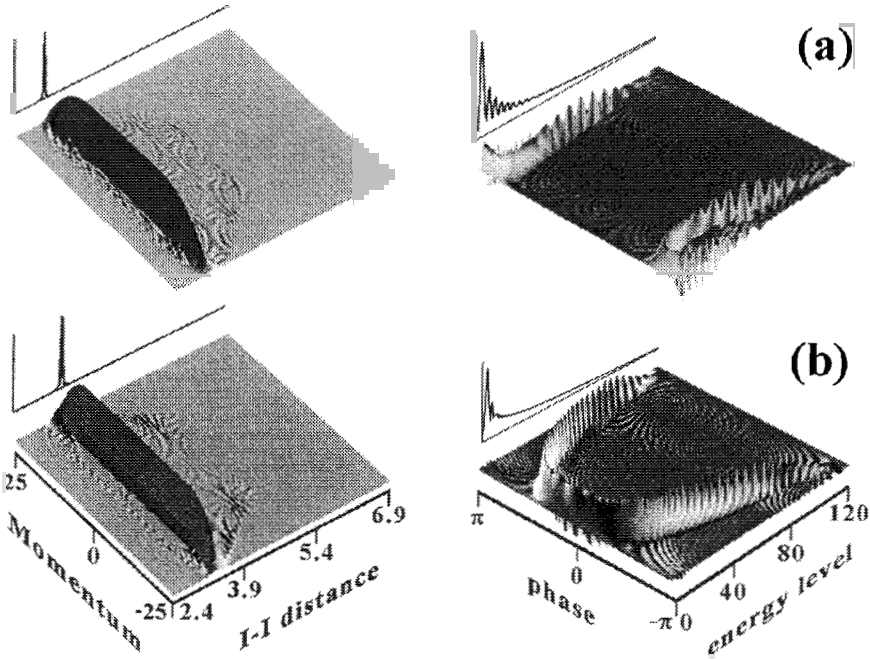

Figure 27. The Wigner distribution function $W_g(r,p)$ and $W_g(v,\phi_v)$ of the window function in Eq. (2.75) of a 60-fs pulse with central frequency of (*a*) 620 nm and (*b*) 880 nm. The projection on the position and vibrational energy coordinates is also shown.

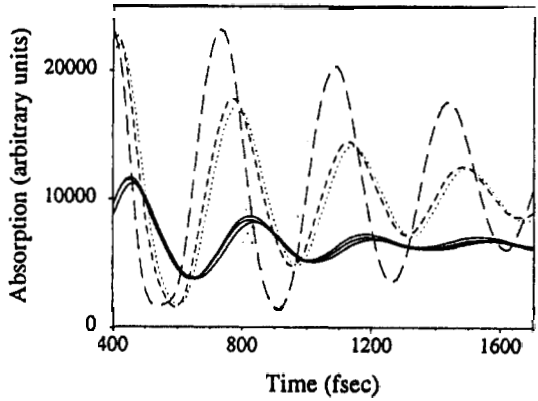

Figure 28. The transient absorption of the I_2^- products originating from different initial wave packets. The evolution was carried out with a dissipation-free Hamiltonian, and the spectrum calculated for a probe pulse of 60-fs duration and a wavelength of 620 nm. All signals are normalized with respect to the excited state population ($tr(\hat{\rho}_g^{s,a})$). The solid lines represent the pure symmetric stretch excitations $|v_{0,0}\rangle$, $|v_{1,0}\rangle$ and $|v_{2,0}\rangle$, which all bunch together. The antisymmetric stretch excitations are represented as broken lines: $|v_{0,1}\rangle$ (dotted), $|v_{1,1}\rangle$ (dashed line) and $|v_{0,2}\rangle$ (long dashed line).

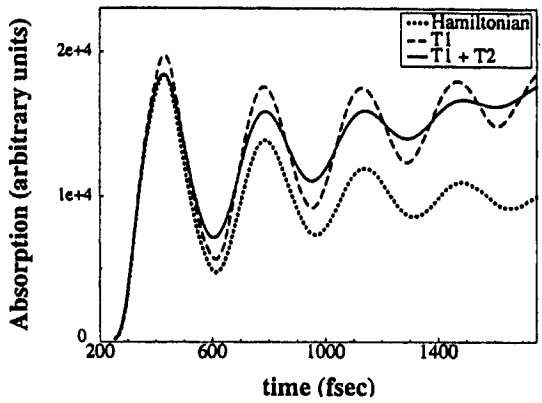

Figure 29. Transient absorption of a 60-fs probe pulse at 620 nm as a function of the time delay between the photodissociation pump and the probe. (*a*) Free Hamiltonian dynamics; (*b*) dynamics including energy relaxation processes (T_1); (*c*) dynamics including vibrational dephasing processes ($T_1 + T_2$).

b. Transient Spectrum Under Dissipation Conditions. To see the effect of the different dissipation mechanisms on the observed spectrum, the total population $\rho_g(v, v')$ was probed during propagation under the influence of the bath operators. Observing Fig. 29, the spectral modulations in the signal of the free evolution dynamics decay, due to the anharmonic nature of the potential, causing the winding motion in Fig. 26(*a*). The suprising observation is that addition of energy relaxation causes the modulations to become more persistent. The reason is that the high vibrational part of the distribution, which is prone to anharmonic motion, is pushed to the lower more harmonic part of the potential and refocused [Figure 26(*b*)]. This transfer is obtained without wiping out the vibrational coherence. The baseline of the modulation also increases, due to the flow of amplitude from the high vibrations into the observation window. As expected when dephasing is added, the spectral modulations decay [Fig. 26(*c*)]. This observation makes it possible to assign the decay of spectral oscillation primarily to dephasing processes.

c. Transient Spectrum at Different Probe Wavelengths. The last calculation (transient spectrum including T_1 and T_2 processes) was repeated for the red-shifted probe, expecting an anti-phased modulation as in the experiment (see Fig. 4). The resulting signal is shown, along with that resulting from the blue-shifted probe, in Fig. 30.

There are two deviations from the experimental scan. The first is the appearance of a double frequency second harmonic part for the red-shifted probe, which disappears after the second modulation (a dephasing process timescale). The second is the phase difference, which only approaches π at the end of the scan (a relaxation process time scale). Examining the window

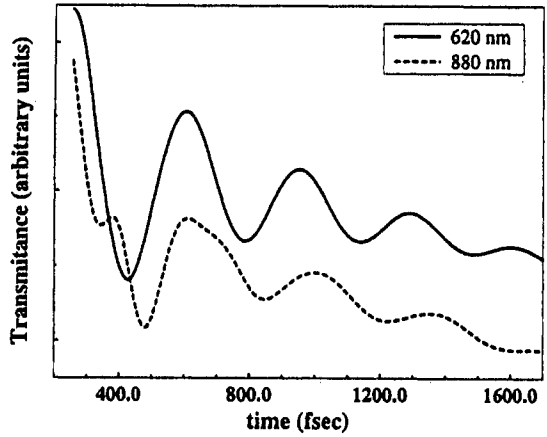

Figure 30. Transient absorption of a 60-fs probe pulse as a function of the time delay between the photodissociating pump and the probe. (*a*) Probe wavelength at 620 nm. (*b*) Probe wavelength at 880 nm.

functions of the probe pulses (Fig. 27), the source of the double frequency is obviously the large bifurcation of the phase dependency at 880 nm. As long as the phase distribution of the population is narrower than this bifurcation [this is true at short times—Fig. 26(*a*)], the distribution crosses the window twice at each cycle of its winding motion. This behavior vanishes as the distribution broadens, due to anharmonicity and dephasing processes [Fig. 26(*c*)]. The absence of this feature from the experimental scan might indicate the existence of earlier dephasing mechanisms not accounted for in the calculation, such as electronic dephasing during the pump pulse, or collisions with the cage prior to bond cleavage. It is also possible that this behavior is obscured by the sharp fall in absorption at the beginning of the scan, attributed to a transition to a higher electronic surface, which is not included in the model. The discrepancy of the phase difference between the different wavelengths is also explained by the shape of the window functions, in which a π phase difference is only present for very low values of v. Only when the distribution cools enough so that a significant portion of the population occupies the lower energy region would an anti-phased behavior appear. This suggests that the initial experimental distribution is cooler than the one obtained from the calculations of the pump pulse.

E. Vibrational Excitation of Relaxed I_2^-: The "Push" Pulse

Typically the dephasing rate is faster, or even much faster, than the energy relaxation rate. The observable consequence is that the spectral modulations have decayed long before the vibrational distribution reaches equilibrium. In order to regain the observable, the spectral modulations are reinvigorated

by adding a push pulse that transfers amplitude to the dissociative excited surface while leaving a dynamical "hole" in the ground surface. Once created, the dynamical "hole" will oscillate, creating new spectral modulations. This phenomena is analogous to the RISRS experiment in the parent I_3^- molecule. The transient frequency of these oscillations can be associated with the energy distribution of the system, and the decay of the modulations can be associated with the dephasing rate. Since both the energy distribution and the phase coherence manifest themselves in the frequency and decay rate of the spectral modulations of the same observable, this experiment makes it possible to measure T_1 and T_2 simultaneously.

1. *Statics*

As in the previous section, the system under study is the I_2^- molecule, so the same degrees of freedom apply here as well. The difference is that the ground and excited electronic states are coupled by the push pulse, so the full dual-surface representation of the density matrix is needed to represent the system.

The initial state for the dynamics is $\hat{\rho}_g(t)$ of the previous section, where t is taken to be 2, 4, 6, 8, and 10 ps before the application of the pulse, $\hat{\rho}_e = \hat{\rho}_c = 0$.

Figure 31(*a*) demonstrates the state of the system after the dephasing process has smoothed out the initial phase dependence (as seen from the flat projection on ϕ_v), and with that eliminated the spectral modulations. At the same time, the relaxation process is still far from completion, as seen from the projection on v which peaks at $v = 10$ and has almost no population at $v = 0$.

The energy distribution of the population is slowly decaying toward a Boltzmann distribution due to T_1 processes, but even after as much as 10 ps thermal equilibrium is still not reached. Figure 32 shows the diagonal elements of the density $\langle v|\hat{\rho}|v\rangle$, which are the relative populations at each energy level, for all initial states.

2. *Dynamics*

a. Interaction with the Solvent and Electromagnetic Field. In view of the two electronic surfaces involved the dissipation mechanisms are divided into electronic and nuclear dissipative processes: $\hat{\mathcal{L}}_D = \hat{\mathcal{L}}_{D_{el}} + \hat{\mathcal{L}}_{D_{nd}}$, where $\hat{\mathcal{L}}_{D_{el}}$ is the electronic dephasing term and $\hat{\mathcal{L}}_{D_{nd}}$ is the nuclear dephasing. Nuclear relaxation processes are neglected for the duration of the pulse, to simplify the calculations. This is justified by the larger time scale of these processes ($\approx$ 3 ps) in comparison with the pulse's duration.

The main electronic dissipative process is dephasing. The mechanism involved originates from fast fluctuations of the dipoles in the solvent, which induce fluctuations in the energy gap between the ground and excited sur-

face. This results in fluctuations of the transition frequencies between the surfaces [compare Eq. (2.60)], and the wave packet looses the coherence ($\hat{\rho}_c$) between its lower and upper parts ($\hat{\rho}_g$ and $\hat{\rho}_e$). By choosing $\hat{\mathbf{V}}_i = \hat{\mathbf{I}} \otimes \hat{\mathbf{S}}_z$ in Eq. (2.34) the electronic dephasing term is obtained

$$\hat{\mathcal{L}}_{D_{el}}(\hat{\rho}) = -\gamma_{el}[\hat{\mathbf{I}} \otimes \hat{\mathbf{S}}_z, [\hat{\mathbf{I}} \otimes \hat{\mathbf{S}}_z, \hat{\rho}]] \tag{3.13}$$

The relaxation coefficient can be related to the electronic dephasing time $\gamma_{el} = 1/\tau_{el}$. The electronic dephasing time τ_{el} was taken to be 30 fs. On the timescale of the experiment nonradiative decay process are negligible, therefore no other electronic dissipative terms are included in the calculation. For simplicity, the nuclear dephasing term is set as a pure dephasing term of the ground surface [Eq. (3.10)]

$$\hat{\mathcal{L}}_{D_{nd}}(\hat{\rho}) = -\gamma_{nd}[\hat{\mathbf{H}}_g \otimes \hat{\mathbf{I}}, [\hat{\mathbf{H}}_g \otimes \hat{\mathbf{I}}, \hat{\rho}]] \tag{3.14}$$

The Hamiltonian is constructed in the eigenstate representation. The operator $\hat{\mathbf{H}}_g$ is the same diagonal matrix as in the previous section, but since $\{|v_i\rangle\}$ are not eigenstates of the upper surface Hamiltonian, $\hat{\mathbf{H}}_e$ is not diagonal and its matrix elements are calculated using Eq. (2.29).

The push pulse has the same characteristics as the pump pulse in Section III.B, except for the carrier frequency, which is attuned to the $I_2^- \rightarrow I^- + I$ electronic transition, slightly blue-shifted from the center of absorption at 616 nm. When the electronic surfaces are coupled by the pulse, population is fed to the upper repulsive potential, and quickly propagated very far from the Frank–Condon region. This "runaway" population is the dissociated I + I^-, which is not probed by the experiment. It will be discarded at the end of the pulse, when the focus of attention is back on the ground I_2^- state. To avoid the need to represent these long propagations, an absorbing boundary condition was imposed on the excited surface.[6] The boundary was set in the eigenstate representation for large values of v, since the highest vibrational states of the ground surface correspond to large propagation distance when projected on the excited surface.

Once the pulse is over and the electronic surfaces decouple, the system can be again treated as in Section III.D, considering only $\hat{\rho}_g$ and setting $\hat{\mathcal{L}}_D = \hat{\mathcal{L}}_{D_{nr}} + \hat{\mathcal{L}}_{D_{nd}}$.

[6]The absorbing boundary condition for a density matrix is a super-operator of the form $\hat{\mathcal{L}}_A(\hat{\rho}) = \{\hat{\rho}, \hat{\mathbf{V}}_{absorbing}\}_+$ added to the Hamiltonian. The value of $\hat{\mathbf{V}}_{absorbing}$ is zero on most of the grid and negative imaginary on the boundary. Any part of the density propagating under the influence of this anti-Hermitian potential will decay exponentially to zero before it can overflow the grid boundary.

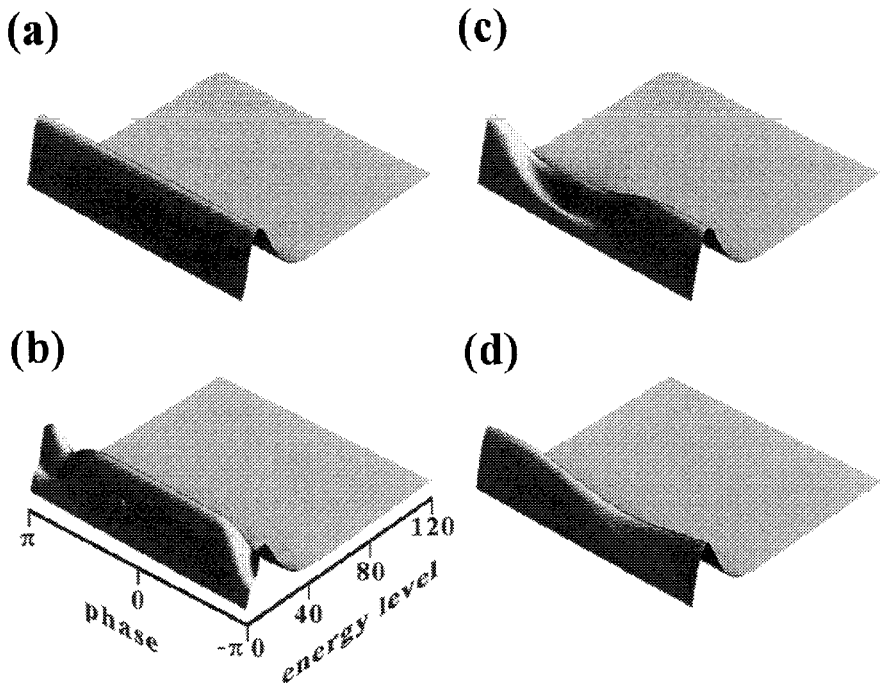

Figure 31. (*a*) The Wigner distribution function $W_g(v, \phi_v)$ after 4 ps. Notice that although the vibrational energy has not reached equilibrium the distribution is phase independent. (*b*) The same distribution function after the application of a push pulse of 60 fs at 616 nm, which photodissociated 20% of the I_2^- population. (*c, d*) The dynamics of the hole after 100,200 fs.

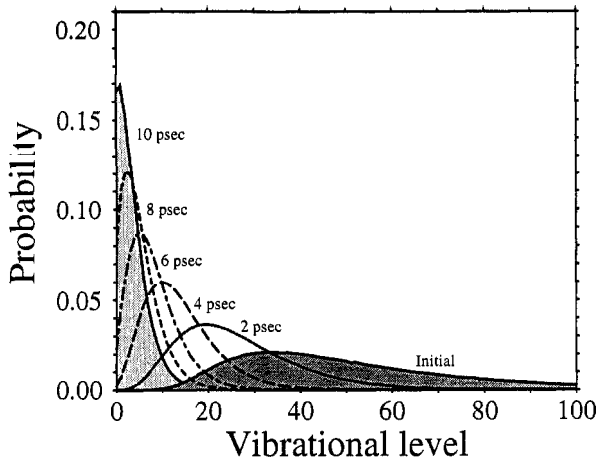

Figure 32. The energy distribution as a function of time delay from the pump pulse

b. Propagation Results. The application of the push pulse in Fig. 31(*b*) has "drilled a hole" in a specific area in the phase coordinate (around $\pm\pi$), which will travel across ϕ_v [Fig. 31(*c*)] until smoothed out by the dephasing [Fig. 31(*d*)]. The winding motion along the phase coordinate renews the spectral modulations. As seen earlier (Fig. 26), the velocity of this motion depends on v, because of the anharmonicity of the vibrational manifold. Thus, the frequency of observed spectral modulations will change with the initial energy distribution at the onset of the push pulse. This phenomena was observed in experiment [4], and recreated in simulation by applying the push pulse at different time delays from the pump, and observing the resulting transient spectrum. The (r,p) picture of the same process is shown in Fig. 33. Notice that the push pulse has drilled two holes in the distribution [Fig. 33(*b*)], at the crossing of the energy iso-line and the resonance line at 3.1 Å (cf. Fig. 27). The hole travels clockwise along the iso-energy line [Fig. 33(*c*)], until smoothed out by the dephasing [Fig. 33(*d*)].

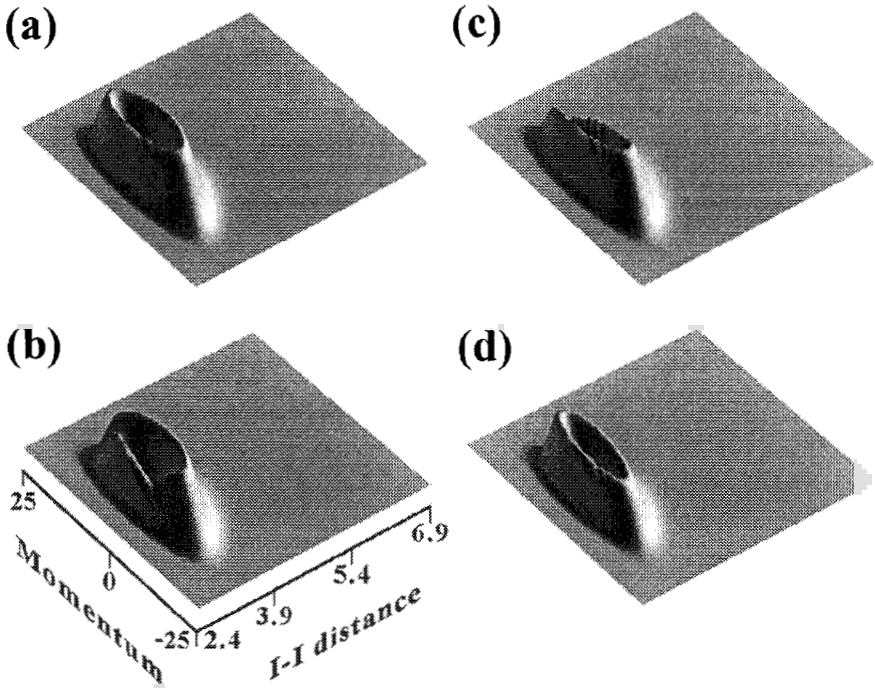

Figure 33. (*a*) The Wigner distribution function $W_g(r,p)$ after 4 ps. (*b*) The same distribution function after the application of a push pulse of 60 fs at 616 nm, which photo dissociated 20% of the I_2^- population. (*c, d*) The dynamics of the hole after 100,200 fs. Distances are in angstroms, and the momentum units are Å/ps.

3 *Interpretation*

The transient spectra for different pump-push delays are shown in Fig. 34. As in the experiment, there is an initial decrease in the absorption during the application of the pulse (due to loss of I_2^- population via photodissociation), followed by a decaying spectral modulation. The percent of photodissociated population falling within the pushing window function increases with time as the population cools and enters the center of the absorbing part of the push window function at lower vibrational levels (cf. Fig. 27 and Fig. 32). The same cooling process is also responsible for the observed increment in the frequencies of the spectral modulations. The modulations were fitted with a decaying harmonic behavior (Fig. 35), and the fit results are compared with the experiment in Table III.

The observed decay times of the modulations are very short (fast decay) for the hot populations measured at short delays, and saturate at a much longer value at longer delays. This trend is seen both in experiment and in simulation. The decay time of the modulations (τ_t) is smaller at high energies because there are contributions to the loss of coherence from the anharmonicity effect (cf. Fig. 29) as well as from the dephasing processes. The slight decrease in τ_t at longer delays can be attributed to the fact that the rate of the dephasing process varies as the square of the oscillator frequency in Eq. (3.11), which is larger at lower vibrational energies. It is satisfying to note that this trend will eventually lead to the chosen parameter $\tau_{nd}(0) \approx 1$ ps,

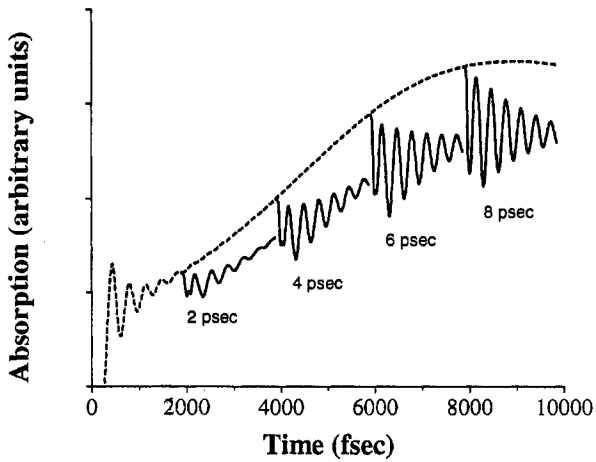

Figure 34. The transient absorption as a function of time showing the perturbation of the push pulse at different times on the dynamics. The dashed line shows the unperturbed dynamics. The pump pulse is at 308 nm, the push and probe at 616 nm.

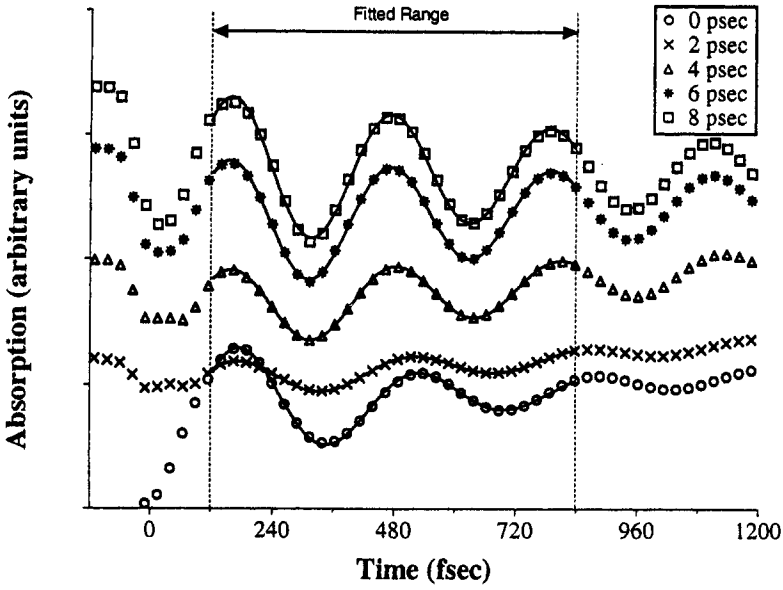

Figure 35. The transient absorption as a function of time delay after the push pulse for different push delays. The middle section was fitted to the function $C + A \cdot e^{-t/\tau_t} \sin(\omega_t t + \phi) + B \cdot t$.

meaning that the asymptotic damping rate of the modulations can be associated with a pure dephasing mechanism.

The values for the frequencies are harder to interpret, as their associated energies do not follow an exponential decay law (as should be expected from a T_1 process), in both experiment and theory. This can be explained by exam-

TABLE III
Fitted Parameters for the TRISRS Spectral Modulations

	Experimental [4]		Calculated	
Push Delay (ps)	ω_t (cm^{-1})	τ_t (ps)	ω_t (cm^{-1})	τ_t (ps)
No push			97 ± .2	0.4 ± .01
2.0	102 ± 4	0.4 ± .2	99 ± .2	0.7 ± .02
2.67	105 ± 3	0.9 ± .2		
4.0	112 ± 2	1.2 ± .3	106 ± .1	1.1 ± .02
6.0	112 ± 2	1.7 ± .4	108 ± .2	1.3 ± .05
8.0			109 ± .3	1.2 ± .07
10.0			110 ± .4	1.1 ± .08
13.4	113 ± 2	1.2 ± .2		

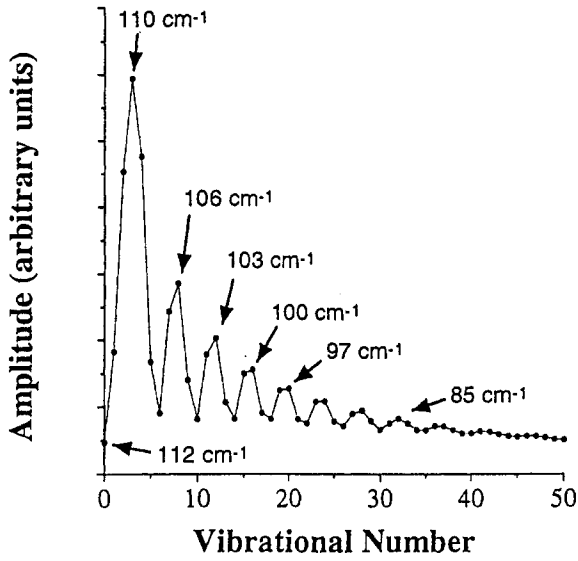

Figure 36. Sensitivity of the probe pulse to the vibrational quantum number, obtained from the diagonal elements of the window function in the v, v' representation. Some typical vibrational frequencies of different vibrational levels are also shown.

ining the sensitivity of the probe pulse to different vibrational levels. As was seen in Fig. 27, the sensitivity is not a smooth function of the vibrational level, but rather oscillatory, with large peaks at low vibrational levels. The behavior at the lower end of the spectrum is magnified in Fig. 36.

By comparing Fig. 31, Fig. 36, and Table III, it is clear that the observed modulation frequency is associated not with the mean energy of the distribution, but rather with its lower energy tail, because of the preference of the window function for lower energies. While the average energy obeys an exponential decay law, its lower energy tail quickly reaches the highest peak in the window at $v = 3$, and stays there throughout the relaxation process, thus masking the continuing decay of the rest of the distribution.

F. Application Summary

The key point in understanding the results of this section is that photoinduced events in the past propagate and influence the outcome of observables at later times. These events have a finite memory span due to electronic and nuclear dissipative processes induced by the solvent. The decay of the spectral modulations is due to a combination of dephasing and loss of compactness due to unharmonic dynamics. The energy relaxation processes are able to enhance the spectral modulations by transferring the population to

lower more harmonic regions of the potential without losing the vibrational coherence. When the dephasing rate is larger than the energy relaxation rate, spectral modulations are invigorated by a push pulse, shedding light on the full scope of vibrational relaxation in solution.

IV. SUMMARY

A. Critical Evaluation

1. Theoretical Framework

The calculation methods developed and applied to the photodissociation dynamics of I_3^- are based on the strict rules of quantum mechanics. In Wigner's terminology "orthodox" quantum mechanics is followed, starting from state vectors to describe the system and operators to describe measurable observables. The evolution of the system is described by differential generators either $\hat{\mathbf{H}}$ for a closed system or $\hat{\mathcal{L}}$ for an open quantum system. All the methods applied are numerically exact, meaning that within the model, the measurable observables converge exponentially with respect to the numerical parameters. Moreover, the interaction with the radiation field is included explicitly and not perturbatively. Employment of these methods assures that the finite precision of the computation can be ruled out as a source of discrepancy with the experiment. The main difficulty in following such a program lies in the exponential scaling of quantum calculations with the number of degrees of freedom. This fact severely limits the scope of the calculation to a small number of modes. Under these conditions, one may wonder, can converged quantum calculation become relevant to an extremely complex scenario such as the photoreaction of I_3^- in solution?

2. Relevance to Experiment

The relevance of the simulation is closely tied to the experimental conditions under study. The photodissociation of I_3^- is characterized by a series of timescale separations. This situation enables the use of the impulsive limit in which the pulse duration is long compared to the electronic transition time, but short compared to the vibrational and rotational periods (see Table IV). Under these circumstances a carefully constructed reduced dimensional quantum description is able to capture the essential dynamics.

The main asset of the computational methods developed in this study are their flexibility in addressing different types of experimental probes. These can be time-dependent, such as the spectral modulations of the product; or time-independent, such as the absorption and Raman spectrum. Each probe gives information on different aspects of the dynamics: The absorption spectrum is associated with the Frank–Condon area of the excited surface; the Raman spectrum covers further ground down the dissociative slope, and can

TABLE IV
Timescales Involved in the I_3^- Photodissociation

Physical Entity		Timescale
Electronic transition	$1/\omega_0$	1 fs
Electronic dephasing	$1/\gamma_z$	5–60 fs
Pulse fluctuations	$1/\gamma_\phi$	100 fs
Pulse duration	t_f	30–60 fs
Pump Probe Delay time	t_{pr}	100–8000 fs
Bond cleavage	τ_{bond}	250 fs
Vibrational period	$1/\omega_v$	300 fs
Vibrational dephasing	$1/\omega_v^2\gamma_v$	400–1000 fs
Vibrational relaxation	T_1	3–10 ps
Reorientation	T_R	10–100 ps

distinguish between motions along the different coordinates; the transient spectrum has an accumulated memory of the entire potential all the way to dissociation, and may serve as a probe for those parts not covered by absorption and Raman spectra. Crossing the information gained from all probes is made possible because they are bundled together as the outcome of a unified framework.

The current simulations are able to point to the experimental levers that are the most relevant to understand the dynamics. The effects of the initial vibrational excitation in the reactants were found to be important. The extremely large effect that the excitation in the antisymmetric stretching mode has on every aspect of the photochemical outcome, be it vibrational excitation in the products, the emergence time of isolated fragments, or the depth of modulation in the transient spectrum, underscores this clearly. The antisymmetric excited population propagates in the antisymmetric direction from the very beginning of the dynamics. This leads to faster bond cleavage and lower vibrational excitation in the products, and helps to keep a compact wave packet for longer times, which enhances the observed spectral modulations. Of special interest here is the strong effect of symmetry breaking on the chemical evolution of the system. This is a particular example of a more general phenomena. The intimate nature of the mutual interaction between the system and the solvent in the present case underlines the prominent role that asymmetric solvation must play in determining the outcome of the reaction.

The calculated Raman spectrum associates the appearance of overtones of the antisymmetric stretch with early motion along the antisymmetric direction, which was shown to have a major part in the creation of spectral modulations. Such overtones, as well as the appearance of the fundamental antisymmetric frequency, were measured experimentally by Anne Meyers and

coworkers [3] in resonance Raman spectra of I_3^- in several organic solvents, and proved to be solvent dependent. This indicates that the solvent has a significant influence on the early stages of the dynamics, and can encourage motion in the antisymmetric direction, by inducing nonsymmetric dipole fluctuations, thus breaking the potential symmetry. In other words, the solvent "helps" the molecule to decide which nuclei are primed to pair up to give the diatomic product. The appearance of the fundamental antisymmetric frequency (which is symmetry forbidden) in protonated solvents (alcohols and water) suggest that these solvents prefer an asymmetric configuration of the ion. Such help from the solvent was shown to be as valuable to the creation of coherent modulations as the impulsive nature of the pulse.

After its emergence, the photoproduct is subjected to various forces which influence the observed spectral modulations. There are energy transfer and dephasing processes originating from interaction with the bath, and there is the anharmonic nature of the I_2^- potential well. The latter makes different components of the wave packet travel at different phase velocities, thus loosing its compact shape, causing a damping of the modulations. Considering only the anharmonic effect, the wave packet is still fully coherent, and if no dissipation processes were taking place as well, a full revival [66] of the compact shape would be expected at a later time. Since dephasing processes are present, destroying the coherence between different populations, such recurrence is impossible. This makes the anharmonic effect practically (experimentally) indistinguishable from the damping caused by the dephasing process, and both contribute to the total decay of the oscillating signal. The TRISRS technique is the key for separating the two components: the anharmonic contribution decreases as the population cools, bringing the measured total decay rate to an asymptotic value equal to the pure dephasing rate.

The role of the energy relaxation in this process is somewhat surprising, as it enhances, rather than decreases, the observed modulations. This is because the relaxation narrows the energy band in which the product population exists, and does so in a coherent fashion, preserving the existing phase dependence and only diminishing the anharmonic effect. The stronger the coupling between the molecular system and the solvent bath, the more efficient this process. It might be that this mechanism is responsible for the more persistent modulations observed experimentally in the highly polar water, in contrast with the rapidly decaying modulations measured in the less polar isobutanol.

The present analysis of the TRISRS signals contains for the first time a complete representation of all dissipative mechanisms influencing the observables. The results confirm the conclusion of earlier analysis and demonstrate that this spectroscopy unveils the evolving vibrational density. As pointed out there, this method is especially well adapted for probing

highly excited vibrational ensembles, complementing information obtained from the time-dependence of fragment absorption spectra. It is important to point out, however, that due to the strong bias any single probe frequency has toward detecting a specific region of the vibration ladder, it is highly recommended that this spectroscopy be implemented with multipole frequencies both of "push" and of probe pulses [4].

3. *Imagery*

Following events in time naturally submits itself to the use of visual tools. The phase space snapshots are chosen as the primary display. Without losing the full quantum picture one is able to directly compare classical and semiclassical calculations. The extension of the phase space image to action-angle representation supplies a new viewpoint at these complex dissipative processes. In particular it allows one to follow the role of phase and phase relaxation directly. This imagery further underlines the limited information content of any single spectroscopic probing method in capturing the full dynamic picture. It is often the case that the phase space picture shows dynamic richness and complexity, yet a given spectroscopic probe shows only a marginal evolution. Unraveling this richness is an immense experimental challenge and requires a multitude of probing techniques.

4. *Theoretical Alternatives*

The fully quantum approach applied to the I_3^- photoreaction is in no way exclusive. The exponential scaling of quantum calculations has served as the primary motivation for the development of a multitude of approximate methods. The most common of which is classical molecular dynamics [11]. Quantum effects are then introduced by employing semiclassical methods or a series of approximate mixed quantum-classical methods [12, 13, 14, 15, 16, 17]. These methods can be related on a mean field approach, usually formulated within the TDSCF approximation [67, 68, 69]. Although these methods are usually applied under uncontrollable approximations conditions, they are able to incorporate many degrees of freedom. Bearing in mind that the purpose of the calculation is to gain insight on the system under study, these methods can become extremely useful. The present approach limits the scope of the calculation in order to obtain a controllable model. Under these circumstances specific effects and their influence on the observables can be studied.

5. *Dissipative Model*

The dissipative quantum dynamics in this study attempts to reach beyond the well-studied two-level system coupled to a bath [32, 70, 71, 72]. The experimental conditions are such that a vast amount of energy has to be dissipated from the highly excited vibrational manifold, thus multilevel excitation is

observed. Under these conditions phase coherence is maintained between many levels simultaneously.

The present approach to vibrational relaxation proves to be conceptually more straightforward than alternative treatments based on an eigenvalue decomposition of the density operator and its interactions [73]. In particular, conservation of coherence despite ongoing energy relaxation arises naturally from following the change in observables in time. This is a particular example of the advantages of an explicit time-dependent approach in studying transient phenomena.

The current dissipative model is based on a phenomenological approach that classifies and parameterizes a small class of dissipative mechanisms. The drawback of this approach is that the solvent properties are only implicitly addressed. It is possible by using the connection between the semigroup approach and the weak coupling limit [21, 30, 73, 74] to relate the semigroup parameters with Fourier transforms of bath correlation functions. This approach has been used by Pugliano et al. [9] to obtain Master equation parameters for the relaxation of IHgI in solution.

A key point in applying a reduced dynamical approach is where to position the partition between the system and bath. This partition determines which degrees of freedom are treated explicitly and which implicitly. The choice in this study, based primarily on computational considerations, was to follow the molecular identities, therefore the primary degrees of freedom are the ones associated with iodine. The large mass mismatch and the similarities of many spectroscopic observables in different solvents partly justify this choice. There is growing tendency to include in the primary zone at least one collective solvation mode. This approach is used in the Brownian oscillator model [75] to couple the electronic and nuclear dissipative dynamics. A collective solvent mode has also been used in the description of the recombination dynamics of I_2^- [64, 76, 77]. The addition of a cage or solvent degree of freedom to the present calculation seems a natural extension. Its inclusion would also correct for inhomogeneous effects not considered presently.

6. *Potentials*

Another drawback of current computation model is the inability to calculate good *ab initio* potentials for this electronic complex system. The hypothesis underlying all the computations in this work, namely that the photodissociation reaction only involves two electronic surfaces, is naive. Preliminary calculations show that the large number of electrons and the strong spin–orbit coupling create a multitude of intercrossing surfaces and recombination paths, which should be incorporated in the simulation. The addition of more electronic surfaces is easily achieved within the developed framework, and is not very costly: the computation scales as the square of the

number of surfaces, and not exponentially with it (as is the case with additional degrees of freedom). The effect of the solvent on the potential energy surfaces also has to be addressed. The charge distribution in the ions is the key quantity. Progress in this direction is on its way.

B. Conclusions

The causal approach of following events in time is the key in gaining insight into a complex dynamical encounter of the photodissociation of I_3^- in solution. Therefore the combination of ultrafast spectroscopic methods and time-dependent quantum mechanical methods naturally fit together to study a process that is characterized by a series of timescale separations.

Acknowledgments

We thank David Tannor and S. Rice for stimulating discussions. This research was supported by Moked, Israel Science Foundation. The Frarkas and the Fritz Haber Research Centers are supported by the Minerva Gesellschaft für die Forschung, GmbH München, FRG.

APPENDIX A: NUMERICAL METHODS

1. Approximating Functions of Operators

Iterative propagation schemes have become the methods of choice in quantum dynamical modeling and simulations. The reason is their superior efficiency when the size of the problem increases. These schemes are based on the ability to perform numerically the elementary step of mapping a state vector by an operator (e.g., $|\phi\rangle = \hat{\mathbf{H}}|\psi\rangle$), or a density matrix by a super-operator (e.g., $\hat{\sigma} = \hat{\mathcal{L}}\hat{\rho}$).[7] The propagators are defined by their recursive application of the elementary mapping step [34]. This amounts to approximating a function of the Hamiltonian as a polynomial.

The original propagation scheme [78], was developed to solve the time-dependent Schrödinger equation. The evolution operator $\hat{\mathbf{U}}(t) = e^{-i\hat{\mathbf{H}}t/\hbar}$ was approximated as a polynomial. A spectral expansion based on the Chebychev orthogonal polynomial was used leading to

$$\psi(t) = e^{-i/\hbar\hat{\mathbf{H}}t}\psi(0)$$

$$\approx e^{-i/\hbar(\Delta E/2 + E_{min})t} \sum_{n=0}^{N_{ch}-1} a_n \left(\frac{\Delta E t}{2\hbar}\right) T_n(\hat{\mathbf{H}}_{\mathbf{norm}})\psi(0) \qquad \text{(A.1)}$$

[7]Since the algebra of vectors and operators is isomorphic to the algebra of matrixes and superoperators, a general notation will be used from here on. ξ will represent a generalized state, and O a generalized operator, so $|\xi\rangle$ and $\hat{\mathbf{O}}$ might as well be read as $\hat{\xi}$ and $\hat{O}$.

where the expansion coefficients become $a_n(\alpha) = i^n(2 - \delta_{n0})J_n(\alpha)$ and $T_n(x)$ are the Chebychev polynomials: $T_n(\cos\theta) = \cos(n\theta)$ [34]. For stability in Eq. (A.1) the Hamiltonian is normalized: $\hat{\mathbf{H}}_{\mathbf{norm}} = 2(\hat{\mathbf{H}} - \overline{H})/\Delta E$ where $\overline{H} = (E_{max} + E_{min})/2$ is the center of the eigenvalue spectrum and $\Delta E = (E_{max} - E_{min})$ is the eigenvalue range of $\hat{\mathbf{H}}$. The normalized Hamiltonian has its eigenvalues distributed on the real axis between -1 and 1.

Examining Eq. (A.1) it can be noticed that the time variable only appears in the expansion coefficients a_n. The computationally intensive part, which is the evaluation of the mapping induced by the Chebychev polynomial: $\phi_n = T_n(\hat{\mathbf{H}}_{norm})\psi(0)$ is time-independent. This observation has led to the development of propagation schemes for other functions of the Hamiltonian. Examples include the Green function, allowing the calculation of Raman spectra [35], or reactive scattering cross sections [79, 80]; the delta function, allowing the calculation of absorption spectra [81] and density of states [82, 83]; propagation in imaginary time [84] and filter diagonalization [85, 86, 87], allowing the calculation of eigenstates. The method can be classified as a spectral expansion of a function of the Hamiltonian operator.

For approximating an analytic function $f(z)$ the spectral expansion possess exponential convergence [78]. Comparison of the Chebychev propagator with other propagation schemes has shown that the Chebychev expansion is usually superior in both accuracy and efficiency to other methods [88].

These findings have led to a prolification of the use of the algorithm and to the exploration of its range of validity. It was found that the original Chebychev algorithm can become unstable when the Hamiltonian operator $\hat{\mathbf{H}}$ is not Hermitian. A complex non-Hermitian Hamiltonian arises naturally when absorbing boundary conditions are introduced [65, 89, 90, 91, 92, 93, 94]. The reason for the instability is that support for the Chebychev polynomials is on the real axis. Although the Chebychev method can tolerate some complex character [90], large complex eigenvalues of the Hamiltonian cause severe instability. Complex eigenvalues are also obtained for the Liouville super-operator in a dissipative environment [20, 21]. Solving the Liouville von Neumann equation for dissipative open systems was the motivation for developing an alternative propagation scheme that could tolerate complex eigenvalues [95].

The new propagator was based on the Newtonian interpolation polynomial. The support points or interpolation points were located on a polygon in the complex plane, and therefore tolerated complex eigenvalues of the Liouville super-operator that are contained within the polygon. Using the theory of interpolation in the complex plane it can be shown that a uniform converging interpolation in a domain D is obtained when the interpolation points are located on the circumference of the domain.

The choice and ordering of the points is crucial to the stability of the algorithm. Evenly distributed points on the exterior of the polygon were obtained by a conformal mapping of the polygon onto a circle, where evenly distributed points are easily obtained by symmetry considerations. An inverse transform distributed the points back onto the polygon. Ordering the points was found to be crucial to the stability of the algorithm and to directly influence the calculation of the divided difference coefficients. It was found that to obtain stability a complete staggering of points was required [95]. The scheme was applied to the evolution operator in simulating photoinduced processes in solution [45, 2] and photoinduced desorption from metal surfaces [96]. Another application has been the calculating of the S matrix in reactive scattering using absorbing boundaries [97, 98].

In practical applications the Newtonian-based propagator was found to be hard to use. The difficulty could be traced to the Schwartz–Christoffel conformal mapping algorithm [99], which is required to obtain the uniformly distributed points on the circumference of the interpolation domain. The mapping algorithm severely limited the order of the Newtonian interpolation polynomial in the complex plane. This is in contrast to Newtonian interpolation on the real axis, where no limit to the order of the polynomial was found [34, 100]. In this work a new approach to defining the interpolation points (termed Leja points [101]) is used. This method is able to overcome the difficulty in locating the interpolation points.

In parallel with these developments, the original Chebychev expansion was generalized, first by shifting the support from the real axis to a line shifted into the complex plane [83]. This shift greatly enhances the stability of the method. The domain of stability becomes an ellipse in the complex plane. Another alternative is to modify the recursion relation of the Chebychev polynomial by adding a damping term [102]. A more rigorous fix to the problem is to define a spectral expansion in the complex plane. The Faber polynomials that are a generalization of the Chebychev polynomials constitute such a set. With the use of the Faber polynomial it has recently been shown that a stable uniform approximation in the complex plane is possible [103].

Before continuing, a brief comparison of the two methods is appropriate. If for the Newtonian propagator the zeros of the Chebychev polynomial are chosen as sampling points, the two methods are numerically equivalent [34]. Formally, if the expansion coefficients in the Chebychev series are calculated by a Gaussian–Chebychev quadrature rule, then the expansion becomes an interpolation formula mathematically equivalent to the Newtonian interpolation formula [34]. For the practitioner it will be shown that the Newtonian method is more flexible when different functions of the Hamiltonian are required simultaneously.

2. Newton's Interpolation Method

The propagation method is based on the Newtonian interpolation formula in which an analytic function $f(z)$ is approximated as a polynomial

$$f(z) \approx \mathcal{P}_{N-1}(z) \equiv \sum_{n=0}^{N-1} a_n \prod_{j=0}^{n-1} (z - x_j) \tag{A.2}$$

By definition, at the sampling points x_j, $f(x_j) \equiv \mathcal{P}(x_j)$. The coefficient a_n is the nth divided difference coefficient [104] defined as

$$a_0 = f[x_0] = f(x_0)$$

$$a_1 = f[x_0, x_1] = \frac{f(x_1) - f(x_0)}{x_1 - x_0} \tag{A.3}$$

$$a_k = f[x_0, x_1, \ldots, x_k] = \frac{f(x_k) - \mathcal{P}_{k-1}(x_k)}{\prod_{j=0}^{k-1} (x_k - x_j)} \tag{A.4}$$

The advantage of this method is the complete freedom in choosing the function $f(z)$. The only demand is the ability to calculate its value at the sampling points so it is even possible to interpolate an integral of a function that can be only integrated numerically, e.g., Eq. (2.89), which is not solvable in the Chebychev method.

When interpolating the function of an operator, rather than of a scalar, the same divided difference coefficients are used in the expansion

$$f(\hat{\mathbf{O}}) \approx \mathcal{P}_{N-1}(\hat{\mathbf{O}}) = \sum_{n=0}^{N-1} a_n \prod_{j=0}^{n-1} (\hat{\mathbf{O}} - x_j \hat{\mathbf{I}}) \tag{A.5}$$

The choice and order of the interpolation points, x_j is the crucial step in the algorithm.

3. Leja's Interpolation Points

The first step is to establish the domain D of eigenvalues of $\hat{\mathbf{O}}$,[8] and shift it on the real axis so it is symmetric with respect to the imaginary axis. Once

[8]For the Hamiltonian operator $\hat{\mathbf{H}}$, the extent of D on the real axis is from $\hat{\mathbf{H}}_{\min} = \hat{\mathbf{V}}_{\min}$ to $\hat{\mathbf{H}}_{\max} = \hat{\mathbf{V}}_{\max} + \hat{\mathbf{P}}^2_{\max}/2m$. The extent on the imaginary axis is from 0 to $-\hat{\mathbf{V}}^{\max}_{\text{absorbing}}$. For the Liouville superoperator $\hat{\mathcal{L}}$, the real extent is from $\hat{\mathcal{L}}_H^{\min} = \hat{\mathbf{H}}_{\min} - \hat{\mathbf{H}}_{\max}$ to $\hat{\mathcal{L}}_H^{\max} = -\hat{\mathcal{L}}_H^{\min}$, and the imaginary from 0 to $\hat{\mathcal{L}}_D^{\max}$, which is negative.

the domain is defined the algorithm used to generate the interpolation points can begin:

1. A line encircling the domain D in the complex plain is defined. For practical purposes it will be chosen as a polygon. The domain is scaled in size, without changing its shape, to make the interpolation process stable. While its exact size will be fixed in step 4, initial coordinates should be of the order of 1.
2. Trial points $\{y_i\}$ are calculated to be equally distributed on the circumference contour of the domain D. The number of trial points is 1.5 to 3 times the number of requested interpolation points.
3. The interpolation points $\{x_i\}_{i=0}^{N-1}$ are chosen from $\{y_i\}$. The first interpolation point can be chosen arbitrarily

$$x_0 = y_0 \tag{A.6}$$

Other interpolation points are chosen so they maximize the denominator of Eq. (A.4). After choosing n such points, the product

$$\mathcal{J}(y_i) = \prod_{j=0}^{n-1} (y_i - x_j) \tag{A.7}$$

is calculated for each trial point y_i. The trial point for which $\mathcal{J}$, Eq. (A.7), is maximal becomes x_n. If Eq. (A.7) goes to zero or infinity for large n's, the size of D should be adjusted to correct that [e.g., scaled down if Eq. (A.7) overflows].

4. The optimal interpolation points are calculated by normalizing the size of D. A point z in the center of the domain is chosen arbitrarily, and a normalizing factor is calculated by

$$\rho = \prod_{j=0}^{N-1} (z - x_j)^{1/N} \tag{A.8}$$

Each of the x_j's is then divided by ρ, to yield $\tilde{z}_j$. The result is N sampling points on the contour of a scaled domain $\tilde{D}$. The normalization is essential to keep Eq. (A.2) stable. If $\tilde{D}$ is too small this will result in divergence of the divided differences (the a_k's), while if it is too large it will diverge the product term in Eq. (A.2).

4. Application to Operators

After choosing the interpolation points, the operator is shifted and scaled so all of its eigenvalues reside inside the domain $\tilde{D}$

$$\tilde{\mathbf{O}} = (\hat{\mathbf{O}} - \overline{O}) \cdot \frac{1}{\sigma} \tag{A.9}$$

Here, $\overline{O}$ is the shift,[9] and σ is a scaling factor. To compensate for the change from $\hat{\mathbf{O}}$ to $\tilde{\mathbf{O}}$, the interpolation polynomial is used to approximate a scaled function $\tilde{f}(z) = f(z\sigma + \overline{O})$

$$\begin{aligned} f(\hat{\mathbf{O}})|\xi\rangle &\equiv \tilde{f}(\tilde{\mathbf{O}})|\xi\rangle \approx \tilde{\mathcal{P}}_{N-1}(\tilde{\mathbf{O}})|\xi\rangle \\ &\equiv a_0|\xi\rangle + a_1(\tilde{\mathbf{O}} - \tilde{z}_0)|\xi\rangle + a_2(\tilde{\mathbf{O}} - \tilde{z}_1)(\tilde{\mathbf{O}} - \tilde{z}_0)|\xi\rangle \end{aligned} \tag{A.10}$$

with the $\tilde{z}_k$'s residing on the contour of $\tilde{D}$, and the a_k's calculated by

$$a_0 = \tilde{f}(\tilde{z}_0) \tag{A.11}$$

$$a_k = \frac{\tilde{f}(\tilde{z}_k) - a_0 - \sum_{l=1}^{k-1} a_l\,(\tilde{z}_k - \tilde{z}_0)\cdots(\tilde{z}_k - \tilde{z}_{l-1})}{(\tilde{z}_k - \tilde{z}_0)\cdots(\tilde{z}_k - \tilde{z}_{k-1})} \tag{A.12}$$

To calculate the product terms in Eq. (A.10) a recursive relation is used

$$\begin{aligned} |\phi_0\rangle &= |\xi\rangle \\ |\phi_1\rangle &= (\tilde{\mathbf{O}} - \tilde{z}_0\hat{\mathbf{I}})|\phi_0\rangle \\ |\phi_{n+1}\rangle &= (\tilde{\mathbf{O}} - \tilde{z}_n\hat{\mathbf{I}})|\phi_n\rangle \end{aligned} \tag{A.13}$$

The final result is obtained by accumulating the sum

$$|\phi\rangle = \sum_{n=0}^{N-1} a_n|\phi_n\rangle \tag{A.14}$$

The sum is truncated when the residuum $a_n||\,|\phi\rangle_n||$ is smaller than a prespecified tolerance. Since the quality of the approximation of the function $f(\hat{\mathbf{O}})$ is equivalent to a scalar function in the domain D, before performing the actual calculation the accuracy can be checked on the scalar function. Figure 37 shows contour maps of the accuracy of the interpolation for some test cases. A few guidelines for choosing the interpolation points can be deduced from experience and from these figures:

1. It becomes obvious that when using interpolation points residing only on the real axis (as in the original Chebychev algorithm) the domain

[9]The real extent of the eigenvalues of $\hat{\mathcal{L}}$ is symmetric with respect to the imaginary axis, so $\overline{O}$ is identically zero in this case.

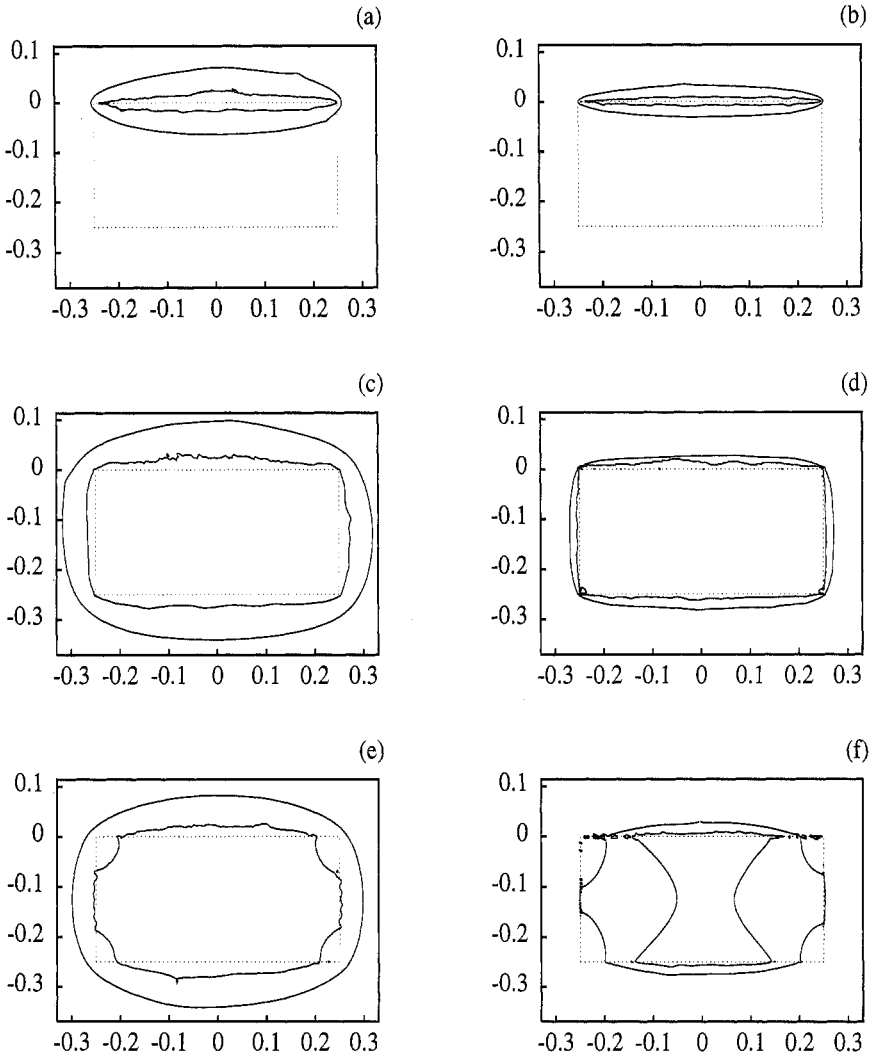

Figure 37. Contour maps for the accuracy of the Newtonian interpolation. The approximated function is an evolution operator as in [Eq. (2.41)], with a time step of 100 a.u. and a Hamiltonian with $\Delta E = \hat{\mathbf{H}}_{max} - \hat{\mathbf{H}}_{min} = 0.5$ a.u. The inner line is the boundary of the domain in which the relative error of the interpolation is less than 10^{-5}, the outer line is for relative error larger than 1 (stability boundary). (*a*) and (*b*) were calculated with the Chebychev algorithm, with interpolation points on the real axis; (*c*)–(*f*) were calculated with Newtonian interpolation, with interpolation points on the dotted rectangle. The number of points used in each map is: (*a*) 64; (*b*) 128; (*c*) 64 chosen from 96; (*d*) 200 chosen from 300; (*e*) 64 chosen from 67; (*f*) 200 chosen from 210.

of stability is a small region around the real axis. Choosing the same number of points on the circumference of a rectangular domain leads to a much better coverage in the complex plain. If the domain contains all of the eigenvalues of the interpolated operator, stability is assured for very long time steps. Figure 37(*a*) and Fig. 37(*b*) show the domain of convergence of the Chebychev scheme.

2. The number of trial points has to exceed the number of actual interpolation points. If too few trial points are used, the interpolation becomes inaccurate, especially in the vicinity of the sharp corners of the domain. Higher order interpolation polynomials require more trial points, since the density of the points increases, making the divided difference terms more sensitive to the choice of the interpolation points. The actual number of trial points needed for a low order ($N < 100$ terms) polynomial is 1.5 times the number of interpolation points, while for higher order polynomials the ratio will be bigger (for an 800-term polynomial a ratio of 1 : 3 was needed). Too many trial points will slow the calculation, but this calculation is performed only once before the propagation cycle. Comparison of Fig. 37(*c*) with Fig. 37(*e*) and of Fig. 37(*d*) with Fig. 37(*f*) shows the effect of not choosing enough trial points on the convergence domain.
3. Employing more interpolation points than is required for obtaining the desired accuracy inside the domain hampers the calculation. As a result the stability area shrinks and if some eigenvalues reside outside, but close to, the domain the accuracy is degraded. This is the reason why the Chebychev algorithm is stable only for short time steps when an absorbing potential is employed, but diverges when using larger time steps that require higher order polynomials. For comparison, the results in Section III.B.2 were calculated using 2000 a.u. (atomic units) time steps (700 terms in the polynomial). The same calculations carried out with the Chebychev algorithm diverged for time steps larger than 100 a.u. (64 terms). This effect can be seen by comparing Fig. 37(*a*) with Fig. 37(*b*), or Fig. 37(*c*) with Fig. 37(*d*).

APPENDIX B: SYSTEM PARAMETERS

TABLE B.I
Potential Surfaces Parameters in Atomic Units

Ground Potential Surface for I_3^- [11]

$$V_g(r_{ab}, r_{bc}) = \tfrac{1}{2}k(r_{ab} - r^{eq})^2 + \tfrac{1}{2}k(r_{bc} - r^{eq})^2 + \chi(r_{ab} - r^{eq})(r_{bc} - r^{eq})$$

$$k = 0.04598 \qquad \chi = 0.01323 \qquad r^{eq} = 5.480$$

Excited Potential Surface for I_3^- [11]

$$V_e(r_{ab}, r_{bc}, r_{ac}) = \Delta E_0 + Q_1 + Q_2 + Q_3 - (J_1^2 + J_2^2 + J_3^2 - J_1J_2 - J_2J_3 - J_3J_1)^{1/2}$$

$$Q_i = \tfrac{1}{2}[{}^1E(r_i) + {}^3E(r_i)] \qquad {}^1E(r_i) = {}^1D[1 - e^{-{}^1\beta(r_i - {}^1r^{eq})}]^2 - {}^1D$$

$$J_i = \tfrac{1}{2}[{}^1E(r_i) - {}^3E(r_i)] \qquad {}^3E(r_i) = {}^3D[1 + e^{-3\beta(r_i - {}^3r^{eq})}]^2 - {}^3D$$

$${}^1r^{eq} = 6.104 \quad {}^1\beta = 0.6138 \quad {}^1D = 0.0404$$

$${}^3r^{eq} = 5.637 \quad {}^3\beta = 0.5292 \quad {}^3D = 0.0371 \quad \Delta E_0 = 0.1361$$

Ground Potential for I_2^- [4]

$$V_g r(r) = D[1 - e^{-\beta(r_i - r^{eq})}]^2$$

$$r^{eq} = 6.104 \quad \beta = 0.6138 \quad D = 4.04 \cdot 10^{-2}$$

Excited Potential for I_2^- [4]

$$V_e x(r) = D + Ve^{-\beta(r - r^{eq})}$$

$$r^{eq} = 6.104 \quad \beta = 1.852 \quad D = 4.04 \cdot 10^{-2} \quad V = 2.168 \cdot 10^{-3}$$

Absorbing Potential [65]

$$V(\bar{y}) = -i \cdot A \cdot N \cdot e^{-2/\bar{y}} \qquad \bar{y} = (y - y_i)/(y_f - y_i)$$

$$A = 0.018 \qquad N = 13.22 \quad y_i = 8.94 \qquad y_f = 9.69$$

$$V(\bar{v}) = -i \cdot A \cdot \bar{y}^2 \qquad \bar{v} = (v - v_i)/(v_f - v_i)$$

$$A = 0.05 \qquad v_i = 100 \quad v_f = 120$$

TABLE B.II
Electromagnetic Field Parameters in Atomic Units

$$\epsilon(t) = \bar{\epsilon}(t)e^{i\omega t} \qquad \bar{\epsilon}(t) = Ae^{\frac{-2\ln 2}{\tau^2}(t - t_0)^2}$$

Pump Pulse [1]

$\omega = 0.1479$ $\quad A = 2.5 \cdot 10^{-4}$ $\quad \tau = 2400$ $\quad t_0 = 4800$

Dipole function $\quad \hat{\mu} = a \cdot \hat{\mathbf{I}}$ $\quad a = 3.7$

Push Pulse [4]

$\omega = 7.396 \cdot 10^{-2}$ $A = 5.9 \cdot 10^{-4}$ $\tau = 2400$ $t_0 = 4800$
Dipole function $\hat{\mu} = a \cdot \hat{\mathbf{I}}$ $a = 2.24$

TABLE B.III
Typical Parameters of Propagation in Atomic Units

Mass Scaled Grid

$\Delta x = 1.2\ 10^{-2}$ $N_x = 1024$ $x_{\min} = 6.24$
$\Delta y = 1.2\ 10^{-2}$ $N_y = 512$ $y_{\min} = 3.42$
Mass $2.315 \cdot 10^5$

Propagation

With pulse $\Delta t = 200$ Order = 70
Without pulse $\Delta t = 1000$ Order = 200

REFERENCES

1. U. Banin, R. Kosloff, and S. Ruhman, *Israel. J. Chem.*, **33,** 141 (1993).
2. U. Banin, A. Bartana, S. Ruhman, and R. Kosloff, *J. Chem. Phys.* **101,** 8461 (1994).
3. A. E. Johnson and A. B. Myers, *J. Chem. Phys.*, **102,** 2519 (1995).
4. U. Banin, R. Kosloff, and S. Ruhman, *Chem. Phys.*, **183,** 289–307 (1994).
5. T. Kühne and P. Vöhringer, *Ultrafast Phenomena*, 1996.
6. S. Ruhman, E. Gordon and E. Gershgoren, *Ultrafast Phenomena*, 1996.
7. M. Gruebele, M. Dantus, R. M. Bowman, and A. H. Zewail, *J. Chem. Phys.*, **91,** 7437 (1989).
8. L. R. Khundkar and A. H. Zewail, *Annu. Rev. Phys. Chem.*, **41,** 15 (1990).
9. N. Pugliano, D. K. Palit, A. Z. Szarka, and R. M. Hochstarsser, *J. Chem. Phys.*, **99,** 7273 (1993).
10. N. Pugliano, A. Z. Szarka, S. Gnanakaran, M. Triechel, and R. M. Hochstarsser, *J. Chem. Phys.*, **103,** 6498 (1995).
11. I. Benjamin, U. Banin, and S. Ruhman, *J. Chem. Phys.*, **98,** 8337 (1993).
12. T. J. Martinez, M. Ben-Nun, and G. Ashkenazi, *J. Chem. Phys.*, **104,** 1996.
13. G. D. Billing, in *Numerical Grid Methods and Their Applications to Schrödinger's Equation*, C. Cerjan, Ed., Kluwer Academic Publishers, The Netherlands, 1993, p. 121.
14. R. Kosloff and A. D. Hammerich, *Faraday Discuss. Chem. Soc.*, **91,** 239–247 (1991).
15. F. Webster, E. Tang, P. Rossky, and R. Friesner, *J. Chem. Phys.*, **100,** 4835 (1994).
16. E. R. Bittner and P. Rossky, *J. Chem. Phys.*, **103,** (1995).
17. Z. L. Zadoyan, V. Apkarian, and C. C. Martens, *J. Phys. Chem.*, **99,** 7453 (1995).

18. G. Ashkenazi, R. Kosloff, S. Ruhman, and H. Tal-Ezer, *J. Chem. Phys.*, **103,** 10005 (1995).
19. A. Bartana, U. Banin, S. Ruhman, and R. Kosloff, *Chem. Phys. Lett.*, **229,** 211 (1994).
20. G. Lindblad, *Commun. Math. Phys.*, **48,** 119 (1976).
21. R. Alicka and K. Landi, *Quantum Dynamical Semigroups and Applications*, Springer-Verlag, 1987.
22. L. Liu and H. Guo, *J. Chem. Phys.*, **103,** 8541, 1996.
23. R. Kosloff, in *Numerical Grid Methods and Their Applications to Schrödinger's Equation.* C. Cerjan, Ed., Kluwer Academic Publishers, The Netherlands, 1993.
24. E. Moyal, *J. Phys. Chem.*, **45,** 99 (1949).
25. V. Gorini, A. Kossokowski, and E. C. G. Sudarshan, *J. Math. Phys.*, **17,** 821 (1976).
26. R. Kosloff, *Physica*, **110A,** 346 (1982).
27. A. Frigerio and V. Gorini, *J. Math. Phys.*, **17,** 2123 (1976).
28. D. Kohen and D. J. Tannor, *J. Chem. Phys.*, (1996).
29. A. G. Redfield, *IBM Jr.*, **1,** 19 (1957).
30. E. B. Davies, *Commun. Math. Phys.*, **39,** 91 (1974).
31. J. L. Skinner, *Annu. Rev. Phys. Chem.*, **39,** 463 (1988).
32. J. L. Skinner, B. B. Laird, and L. Root, *J. Lumin.*, **45,** 6 (1990).
33. H. Tal Ezer, R. Kosloff, and C. Cerjan, *J. Comp. Phys.*, **100,** 179 (1992).
34. R. Kosloff, *Annu. Rev. Phys. Chem.*, **45,** 145 (1994).
35. R. Kosloff, *J. Phys. Chem.*, **92,** 2087 (1988).
36. W. Magnus, *Comm. Pure and Appl. Math.*, **7,** 659 (1954).
37. M. D. Feit, J. A. Fleck, Jr., and A. Steiger, *J. Comm. Phys.*, **47,** 412 (1982).
38. M. D. Feit and J. A. Fleck, Jr., *J. Chem. Phys.*, **78,** 301 (1983).
39. L. Allen and J. H. Eberly, *Optical Resonance and Two-Level Atoms*, Dover, 1987.
40. B. M. Garraway, K.-A. Suominen, and S. Stenholm, *Phys. Rev. A*, **45,** 3060 (1992).
41. C. Cohen-Tanoundji and J. Allen, *Quantum Mechanics*, Wiley, New York, 1977.
42. T. J. Smith, L. W. Ungar, and J. A. Cina, *J. Lumin.*, **58,** 66 (1994).
43. Y. X. Yan, L. T. Cheng, K. A. Nelson, in *Advances in Nonlinear Spectroscopy*, R. G. H. Clarke, and R. E. Hester, Eds., Wiley, New York, 1987.
44. R. Kosloff, A. Dell Hammerich, and D. Tannor, *Phys. Rev. Lett.*, **69,** 2172 (1992).
45. A. Bartana, R. Kosloff, and D. Tannor, *J. Chem. Phys.*, **99,** 196 (1993).
46. W. T. Pollard and R. A. Mathies, *Annu. Rev. Phys. Chem.*, **43,** 497 (1992).
47. W. T. Pollard, S. L. Dexheimer, Q. Wang, L. A. Peteanu, C. V. Shank, and R. A. Mathies, *J. Phys. Chem.*, **96,** 6147 (1992).
48. J. D. Jackson, *Classical Electrodynamics*, Wiley, 1975.
49. Y. J. Yan and S. Mukamel, *Phys. Rev. A*, **41,** 6485 (1990).
50. N. F. Scherer, R. J. Carlson, A. Matro, M. Du, A. J. Ruggiero, V. Romero-Rochin, J. A. China, G. R. Fleming, and S. A. Rice, *J. Chem. Phys.*, **95,** 1487 (1991).
51. N. F. Scherer, L. D. Ziegler, and G. R. Fleming, *J. Chem. Phys.*, **96,** 5544 (1992).
52. N. F. Scherer, D. M. Jonas, and G. R. Fleming, *J. Chem. Phys.*, **99,** 153 (1993).
53. S. Rice, H. Tang, and R. Kosloff, *J. Chem. Phys.*, **104,** 5457 (1996).
54. M. Cho, N. F. Scherer, G. R. Fleming, and S. Mukamel, *J. Chem. Phys.*, **77,** 202 (1982).

55. W. P. de Boeiji, M. S. Pshenichnikov, and D. A. Weirsma, *Chem. Phys. Lett.*, **238,** 1 (1995).
56. G. Stock, L. Seidner, and W. Domcke, *J. Chem. Phys.*, **103,** 3998 (1995).
57. R. Baer and R. Kosloff, *Chem. Phys. Lett.*, **200,** 183 (1992).
58. D. J. Tannor and E. J. Heller, *J. Chem. Phys.*, **77,** 202 (1982).
59. D. Danovich, J. Hrusak, and S. Shaik, *Chem. Phys. Lett.*, **233,** 249 (1995).
60. G. Asahkenazi, K. Yamashita, R. Kosloff, and S. Ruhman, in preparation (1996).
61. E. C. M. Chen and W. E. Wentworth, *J. Phys. Chem.*, **89,** 4099 (1985).
62. P. E. Maslen, J. M. Papanikolas, J. Faeder, R. Parson, and S. V. ONeil, *J. Chem. Phys.*, **101,** 5731 (1994).
63. P. K. Walhout, J. C. Alfano, K. A. M. Thakur, and P. Barbara, *J. Phys. Chem.*, **99,** 7568 (1995).
64. I. Benjamin, P. Barbara, B. J. Gertner, and J. T. Hynes, *J. Phys. Chem.*, **99,** 7557 (1995).
65. A. Vibok and G. G. Balint-Kurti, *J. Phys. Chem.*, **96,** 7615 (1992).
66. I. Sh. Averbuck and N. F. Perelman, *Phys. Lett.*, **139A,** 449 (1989).
67. R. B. Gerber, A. Garcia-Vela, *J. Chem. Phys.*, **98,** 427 (1993).
68. P. Jungwirth and R. B. Gerber, *J. Chem. Phys.*, **102,** 6046 (1995).
69. H. Stock, *J. Chem. Phys.*, **103,** 2888 (1995).
70. F. Bloch, *Phys. Rev.*, **102,** 104 (1956).
71. M. Toplar and N. Mackri, *J. Chem. Phys.*, **101,** 7500 (1994).
72. P. Hänggi, P. Talkner, and M. Borkovec, *Rev. Mod. Phys.*, **62,** 251 (1990).
73. W. T. Pollard and R. A. Freisner, *J. Chem. Phys.*, **100,** 5054 (1994); *Adv. Chem. Phys.*, **93,** 77 (1996).
74. E. B. Davies, *Quantum Theory of Open Systems*, Academic Press, 1976.
75. S. Mukamel, *Annu. Rev. Phys. Chem.*, **41,** 647 (1990).
76. R. Bianco and J. T. Hynes, *J. Chem. Phys.*, **102,** 7885 (1995).
77. R. Bianco and J. T. Hynes, *J. Chem. Phys.*, **102,** 7864 (1995).
78. H. Tal-Ezer and R. Kosloff, *J. Chem. Phys.*, **96,** 5618 (1992).
79. D. J. Kouri, M. Arnold and D. J. Hoffman, *Chem. Phys. Lett.*, **203,** 96 (1993).
80. W. Zhu, Y. Huang, D. J. Kouri, C. Chandler and D. J. Hoffman, *Chem. Phys. Lett.*, **217,** 73 (1994).
81. B. Hartke, R. Kosloff, and S. Ruhman, *Chem. Phys. Lett.*, **158,** 238 (1989).
82. Y. Huang, W. Zhu, D. J. Kouri, and D. J. Hoffman, *Chem. Phys. Lett.*, **214,** 451 (1993).
83. D. J. Kouri, W. Zhu, Y. Hoang, and D. J. Hoffman, *Chem. Phys. Lett.*, **220,** 312 (1994).
84. R. Kosloff and H. Tal-Ezer, *Chem. Phys. Lett.*, **127,** 223 (1986).
85. D. Neuhauser, *J. Chem. Phys.*, **93,** 2611 (1990).
86. D. Neuhauser, *J. Chem. Phys.*, **100,** 5076 (1994).
87. M. R. Wall and D. Neuhauser, *J. Chem. Phys.*, **102,** 8011 (1995).
88. C. Leforestier, R. Bisseling, C. Cerjan, M. Feit, R. Freisner, A. Guldberg, A. D. Hammerich, G. Julicard, W. Karrlein, H. Dieter Meyer, N. Lipkin, O. Roncero, and R. Kosloff, *J. Comp. Phys.*, **94,** 59 (1991).
89. C. Leforestier and R. E. Wyatt, *Chem. Phys. Lett.*, **78,** 2334 (1983).
90. R. Kosloff and D. Kosloff, *J. Comp. Phys.*, **63,** 363 (1986).

91. D. Neuhauser and M. Baer, *J. Chem. Phys.*, **90,** 4351 (1989).
92. M. S. Child, *Mol. Phys.*, **72,** 89 (1991).
93. G. G. Balint-Kurti and A. Vibok A, in *Numerical Grid Methods and Their Application to Schrödinger's Equation*, C. Cerjan, Ed., Kluwer Academic Publishers, The Netherlands, 1993, p. 412.
94. C. W. MacCurdy, and C. K. Stround, *Comp. Phys. Comm.*, **63,** 323 (1991).
95. M. Berman, R. Kosloff, and H. Tal-Ezer, *J. Phys. A*, **25,** 1283 (1992).
96. P. Saalfrank, R. Baer, and R. Kosloff, *Chem. Phys. Lett.*, **230,** 463 (1994).
97. S. Aurbach and C. Leforestier, *Comp. Phys. Comm.*, **78,** 55 (1994).
98. S. M. Auerbach and W. H. Miller, *J. Chem. Phys.*, **100,** 1103 (1994).
99. L. M. Trefethen, *J. Sci. Stat. Comput.*, **1,** 82 (1980).
100. U. Peskin, R. Kosloff, and N. Moiseyev, *J. Chem. Phys.*, **100,** 8849 (1994).
101. Lotharreichel, *Bite*, **30,** 332 (1990).
102. V. A. Mandelshtam and H. S. Taylor, *J. Chem. Phys.*, **102** (1995).
103. Y. Hoang, D. J. Kouri, and D. J. Hoffman, *J. Chem. Phys.*, **101,** 10493 (1994).
104. M. Abramowitz and I. A. Stegun, *Handbook of Mathematical Functions*, Dover, 1972.